SCUOLA DI DOTTORATO
UNIVERSITÀ DEGLI STUDI DI MILANO-BICOCCA

Department of Earth and Environmental Sciences (DISAT)

Ph.D. program in Chemical, Geological and Environmental Sciences

Cycle XXIX

Geological Sciences curriculum

THE MAGMA PLUMBING SYSTEM OF THE "RIFT VOLCANISM" ACTIVITY IN EL HIERRO, CANARY ISLANDS: FLUID INCLUSION AND PETROLOGICAL STUDIES

OGLIALORO EDUARDO

Registration number: 760344

Tutor: Prof.ssa Frezzotti Maria Luce

Co-tutor: Dott. Groppelli Gianluca - Dott.ssa Principe Claudia

Coordinatore: Prof.ssa Frezzotti Maria Luce

ACADEMIC YEAR 2016/2017

ABSTRACT

The present thesis integrates fluid inclusion, petrographic, and geochemical studies to model the internal structure and magma dynamics of El Hierro volcano, the western and smallest island of Canary Archipelago (Spain). The reconstruction of the magma plumbing system of this volcano improves the knowledge about the presence of a lithospheric magma reservoir beneath the oceanic volcanic island. Moreover, the data obtained can be useful for monitoring strategies implementation and hazard evaluation of the island, where the latest submarine eruption took place in 2011-2012.

For this study, xenolith samples have been collected in a locality in the El Julan valley (SSW of the island) from a basaltic lava flow (40 ka; Volcanism cycle).

The modal compositions have been performed on 16 among the best preserved samples. Peridotites have been classified in dunites, harzburgites and lherzolites (type I olivine-orthopyroxene-spinel series). Most harzburgites and lherzolites with texture from protogranular to porphyroclastic show a variable recrystallization degree (from 10 to 50 %). Two generations of olivine and orthopyroxene are observed in the most recrystallized samples. Olivine shows large and elongated strained grains (porphyroclasts) and smaller polygonal strain-free ones (neoblasts). Orthopyroxene shows large euhedral exsolved strained grains (porphyroclasts) and smaller polygonal, clear, or mildly strained ones (neoblasts). Finally, clinopyroxene and spinel are present as small irregular interstitial grains.

In addition, eight peridotites have been analysed for mineral phase composition by electron microprobe analyses (WDS). Olivine Mg# (Mg# = Mg/Mg+Fe) range from 89.3 to 91 wt%, with the highest values in harzburgites. Orthopyroxene and clinopyroxene contain Mg# between 0.90 to 0.91 wt%, with an increase in Al_2O_3 (opx: 2.1- 3.7; cpx: 1.6-4.5 wt.%) and a decrease in Cr_2O_3 (opx: 0.2-0.7; cpx: 0.4-1.1 wt.%) from dunites to lherzolites.

Based on the mineral chemistry and the geobarometry of spinel bearing peridotites, the pressure of re-equilibration at lithospheric depths has been calculated and it ranges between 1.5 and 2.0 GPa. The temperature equilibria conditions have been found different in 2 types of xenoliths: LT-type T= 800-950 °C and HT-type T= 900-1100 °C, suggesting an isobaric heating at various depths.

Two types of trapped fluids in LT and HT peridotites (8 samples) have been analysed by Raman microspectroscopy and microthermometry:

Type I, CO_2-N_2 fluid inclusions, containing dominantly carbonate/sulfate/phosphate/spinel daughter phases (LT peridotites); *Type II*, pure CO_2 fluid inclusions (both LT and HT peridotites). In CO_2-N_2 fluid, X_{N2} varies from 0.01 to 0.18. *P-T* conditions in the lithosphere at 1.8 GPa and 950 °C (~ 60 km depth) have been indicated by the highest density *Type I* CO_2-N_2 (X_{N2} = 0.18; d=1.19 g/cm^3). In CO_2 fluid, 2 main intervals of the homogenization temperatures (T_h) have been identified, with density intervals corresponding to 0.99 - 1.11 g/cm^3, and to 0.65 - 0.75 g/cm^3.

These values define two pressure intervals ranging to 0.67 - 1 GPa and to 0.26 - 0.34 GPa respectively, suggesting a multistage ascent behavior of magmas.

The halogen concentration has been investigated in *Type I* fluid inclusions trapped in 2 LT peridotites applying the noble gas method. I/Cl and Br/Cl ratios exhibit values of $6.2*10^{-4}$ - $6.5*10^{-4}$ and of 2.02 $*10^{-3}$ - 1.96 $*10^{-3}$, respectively. These ratios result higher than typical MORB/OIB mantle (from 1.1 $*10^{-5}$ a 1.01 $*10^{-4}$), supporting a metasomatic origin for *Type I* fluid at lithospheric depths of about 60 km.

In order to describe magma ascent dynamics based on fluid inclusion studies in peridotite xenoliths of El Julan, once the *P-T* conditions of *Type I* and *Type II* fluids have been defined, the corresponding depths have been estimated following the relation: $H= P/(g*d)$ [where H is the depth of the trapped fluid, P the lithostatic pressure, g gravity acceleration (9.81 m/sec^2) and d is the density of the column-rocks]. A simplified stratigraphic reconstruction has been used to consider the difference in density between the rocks of the crust and the mantle lithosphere (d= from 2.5 g/cm^3 to 3 g/cm^3) with Moho beneath El Hierro Island at about 12.5-15 km.

According to *Type I* fluid inclusion and mineral geothermobarometry, the minimum depth of origin of the peridotites has been identified at about 60±10 km in the lithosphere. The multistage ascent behavior of magmas have been characterized by two shallower trapping events of CO_2 (*Type II*) degassed from basaltic magmas, which identify two episodes of magma rest during the ascent to the surface: the first one, from 36 to 22 km, in the lithospheric mantle, and the latter, from 10 to 12 km, in the lower oceanic crust. The deepest region of magma accumulation has been interpreted as a "vertically staked reservoir", where the storage of magma is characterized by a vertical network of small magma pockets, which extends for 14 km. In the lower crust the presence of an ephemeral level of magma stagnation prior to eruption is also suggested.

The results obtained have been also compared with the dynamics of magma ascent of the last eruption in 2011-2012 for the island suggesting the same magma plumbing system beneath El Hierro, for the last 40 ka. Moreover, this model could be useful for investigating the magma ascent dynamics in other oceanic volcanic islands. Further insights into the magma ascent dynamics of El Hierro could be obtained from the reconstruction of the magma plumbing system during the whole sub aerial activity of the volcano starting from 1.12 Ma. In addition, mantle metasomatic fluids which have affected the lithosphere beneath the Canary Islands could be investigated by further petrological and geochemical studies of peridotites and fluid trapped, improving models of the petrogenesis of basaltic magmas.

RIASSUNTO

La presente tesi intende integrare lo studio petrografico, geochimico e di inclusioni fluide per modellizzare la struttura interna e le dinamiche di risalita del vulcano di El Hierro, l'isola più piccola e ad ovest dell'Arcipelago delle Canarie (Spagna). La ricostruzione del sistema di alimentazione di questo vulcano migliora le conoscenze riguardo la presenza di un reservoir litosferico di magma per le isole vulcaniche oceaniche durante la loro fase matura. Inoltre, i dati ottenuti possono essere utili all'implementazione delle strategie di monitoraggio e valutazione del rischio per l'isola, dove l'ultima eruzione risale al 2011-2012.

Per questo studio, xenoliti ultramafici sono state campionati nella località di El Julan valley (S SW dell'isola) da una colata di lava basaltica (40ka); la colata è relativa al ciclo del Rift Volcanism.

Su 16 dei campioni meglio preservati è stata definita la composizione modale. Le peridotiti sono state classificate in duniti, harzburgiti e lherzoliti (serie type I olivine-orthopyroxene-spinel). La maggior parte delle lherzolite ed harzburgite con tessitura da protogranulare a porfiroclastica mostrano un grado variabile di ricristallizzazione (da 10 a 50%). Due generazioni di olivina e ortopirosseno sono osservate nei campioni maggiormente ricristallizzati. Le olivine si presentano in grandi grani elongati e striati (porfiroclasti) e più piccoli grani poligonali privi di striature (neoblasti). L'ortopirosseno si presenta in grani euedrali e con striature-essoluzioni (porfiroclasti) e più piccoli grani poligonali, chiari o moderatamente striati (neoblasti). Clinopirosseno e spinello sono presenti in piccoli grani interstiziali irregolari.

Per 8 di queste peridotiti la composizione chimica delle fasi minerali è stata analizzata tramite microsonda elettronica (WDS). L'olivina ha un Mg# (Mg# = Mg/Mg+Fe) tra 89.3 e 91 wt%, con i più alti valori nelle harzburgiti. Ortopirosseno e clinopirosseno hanno un Mg# tra 0.90 e 0.91 wt%, con un arricchimento in Al_2O_3 (opx: 2.1- 3.7; cpx: 1.6-4.5 wt%) ed un impoverimento in Cr_2O_3 (opx: 0.2-0.7; cpx: 0.4-1.1 wt%) da duniti a lherzoliti.

Sulla base delle composizioni minerali e la geobarometria delle peridotiti a spinello, le condizioni di equilibrio a profondità della litosfera sono state calcolate tra 1.5 e 2.0 GPa. Le temperature di equilibrio sono state definite differentemente per 2 gruppi di xenoliti: per LT-type *T*= 800-950 °C e per HT-type *T*= 900-1100 °C, suggerendo un riscaldamento isobarico avvenuto a differenti profondità.

Due tipi di fluido intrappolato in LT e HT peridotiti (8 campioni) sono stati analizzati con microspectroscopia Raman e microtermobarometria: *Type I*, CO_2-N_2 inclusioni fluide, contenenti fasi minerali di carbonato/solfato/fosfato/spinello (LT peridotiti); *Type II,* pura CO_2 inclusioni fluide (in entrambe LT e HT peridotiti). Nel fluido CO_2-N_2, X_{N2} varia da 0.01 a 0.18. Le condizioni P-T sono state definite dall'inclusione *Type I* CO_2-N_2 più densa analizzata (X_{N2} = 0.18; d=1.19

g/cm^3) a 1.8 GPa e 950 °C (~ 60km in profondità). Per le inclusioni *Type II* sono stati definiti 2 principali intervalli di temperature di omogeneizzazione (T_h), con intervalli di densità corrispondenti tra 0.99 e 1.11 g/cm^3, e tra 0.65 e 0.75 g/cm^3. Questi valori identificano 2 intervalli di pressione tra 0.67 e 1 GPa, e tra 0.26 e 0.34 GPa rispettivamente, suggerendo una risalita del magma a stadi multipli.

La concentrazione degli alogeni è stata investigate nelle inclusioni *Type I* in 2 peridotiti LT applicando il metodo dei gas nobili. I rapporti I/Cl e Br/Cl mostrano valori di $6.2*10^{-4}$ - $6.5*10^{-4}$ e di $2.02*10^{-3}$ - $1.96*10^{-3}$ rispettivamente nei 2 campioni. Questi rapporti risultano più alti di quelli tipici del mantello MORB/OIB (da $1.1*10^{-5}$ a $1.01*10^{-4}$), supportando l'origine metasomatica del fluido *Type I* a condizioni litosferiche di 60 km di profondità.

Per definire le dinamiche di risalita del magma sulla base dello studio delle inclusioni fluide intrappolate negli xenoliti di El Julan, una volta definite le condizioni *P-T* dei 2 tipi di fluido, le corrispondenti profondità sono state stimate seguendo la relazione: $H= P/(g*d)$ [dove H è la profondità di intrappolamento del fluido, P la pressione litostatica, g l'accelerazione di gravità (9.81 m/sec^2) e d la densità della colonna di roccia. Una ricostruzione stratigrafica semplifica è stata usata considerando le differenze di densità tra le rocce di crosta e del mantello litosferico (d= da 2.5 g/cm^3 a 3 g/cm^3) con la Moho al di sotto dell'Isola di El Hierro a circa 12.5-15 km.

In accordo con le inclusioni fluide *Type I* e la geotermobarometria dei minerali, la minima profondità di origine degli xenoliti è identificata a 60±10 km nella litosfera. La risalita multistadio del magma è stata caratterizzata da 2 eventi di intrappolamento di CO_2 (*Type II)* degassata dal magma basaltico, identificando due episodi di stazionamento del magma durante la risalita: il primo tra 36 e 22 km nel mantello litosferico, e il secondo tra 10 e 12 km nella bassa crosta oceanica. La più profonda zona di accumulazione del magma è stata interpretata come un "vertically staked magma reservoir", dove lo stazionamento del magma è caratterizzato da una rete verticale di piccole tasche di magma impilate per 14 km. Nella bassa crosta è suggerito un livello effimero di stazionamento del magma, prima dell'eruzione. I risultati ottenuti sono stati comparati con l'ultima eruzione del 2011-2012, per capire se il sistema fosse cambiato negli ultimi 40 ka, durante la sua fase matura. Il modello proposto può essere d'aiuto nell'investigare le dinamiche di risalita del magma anche per altre isole oceaniche vulcaniche. Ulteriori informazioni riguardo al sistema di alimentazione del vulcano di El Hierro potranno essere ottenute con lo studio delle unità affioranti più vecchie (a partire da 1.12 Ma), caratterizzando la fase immatura dell'isola. Inoltre maggiori investigazioni sulla natura geochimica del fluido metasomatico agente sulle rocce litosferiche delle Isole Canarie, potranno implementare i modelli petrogenetici riguardanti l'origine del magma.

THESIS LAYOUT

The present thesis consists of two manuscripts which have been submitted to peer-reviewed journals (manuscripts 1 and 2). The manuscripts discuss in detail the lines of research developed during the Ph.D. to investigate the magma plumbing system of El Hierro Island during the "Rift Volcanism" cycle, and the geochemical nature of its ultramafic rocks and trapped fluids. Before the manuscripts, an introductive chapter provides a brief overview of the current state of knowledge on present magma ascent dynamics beneath various volcanic islands, and on the application of fluid inclusion studies to volcanological research, and outlines the aims of the two research lines. This section is followed by a synthesis of the geological setting of El Hierro Island and a chapter on the analytical approach. Following the manuscripts, a brief discussion on the main results of this thesis is given, with insights on future studies.

1. INTRODUCTION

Understanding the mechanisms of magma ascent preceding eruptions, and in particular the systems that store and transport magma from the lithospheric mantle to the surface, is of paramount importance for the evaluation of hazard and risk monitoring strategies (Shaw 1980; Ryan 1988; Scandone et al. 2007).

The ascent of magma is largely controlled by buoyancy mechanisms. As suggested by Scandone et al. (2007), magma ascends by injection of discrete batches into a preformed crack network; an eruption indicates that magma batches are rising along connected fracture networks. Eruptive activity is also governed by local or regional structural weakness patterns (Nakamura 1977; Shaw 1980). Volcanic and tectonic stress fields along the ascending pathway of magma have a large influence on the spatial evolution of volcanoes, and on magma transport and eruption (e.g., Gudmundsson 2006; Hildner et al. 2011).

A magma plumbing system is defined as a series of storage regions and feeder conduits through which magma rise from its source at depth to the Earth's surface (Caricchi and Blundy 2015). In oceanic intraplate volcanoes, a mainly vertical magma ascent from a deep reservoir characterizes the early stages of growth (Gudmundsson 2006; Klügel et al. 2015). The presence of a vertical conduit allows the ascent of large amounts of magma that contribute to a rapid growth of the volcanic edifice. The following stages of volcanic activity can be affected by a complex evolution of the magma-feeding system in the lithosphere, with the formation of different magma accumulation levels of variable thickness and located at different depths in the crust and/or mantle (Clague and Dixon 2000; Klügel et al. 2015). This evolution can take place due to a change of chemical and physical properties of the magmas (i.e., chemical differentiation) and/or to different regional or local stress fields that change in time. The combination of lateral spreading and overburden pressure, and gravitational collapses can affect the paths of magma in its ascent to the

Earth's surface, during all the different stages of growth of a volcano (Gudmundsson 2006; Becerril et al. 2013a).

During the last thirty years, many authors have proposed different models focusing on the magma plumbing system of ancient and/or active volcanoes with the goal of defining magma paths and pressure conditions of storage levels, chiefly in the crust, using different methods of investigation, such as geophysics, petrology, geochemistry and experimental petrology (e.g. Bertagnini et al. 2002; Klügel et al. 2000; 2005; Schwarz et al. 2004; Morgan et al. 2007; Stroncik et al. 2009). The pathways and time scale of magma ascent can also be assessed by fluid inclusion studies combined with petrological investigations (e.g., Frezzotti et al. 1992; Belkin and De Vivo 1993; Hansteen et al. 1998; Andersen and Neumann 2001; Frezzotti and Peccerillo 2004; Hansteen and Klügel 2008). Fluid inclusion geothermobarometry has been successfully applied in mantle and crustal xenoliths contained in lavas and pyroclastic successions to reconstruct the magma plumbing systems of different volcanoes, in both continental and oceanic settings.

In oceanic volcanic islands, fluid inclusion studies in mantle xenoliths and in olivine phenocrysts in basaltic magmas have been applied to characterize the evolution and magma conditions of Hawaii Islands (e.g., Roedder 1983; De Vivo et al. 1988; Frezzotti et al. 1991), Cape Verde archipelago (e.g., Holm et al. 2008; Hildner et al. 2011), Azores archipelago (e.g., Zanon and Frezzotti 2013; Zanon 2015) and Canary Islands (e.g., Hansteen et al. 1991; Frezzotti et al. 1994; Andersen et al. 1995; Neumann et al. 1995; Hansteen et al. 1998; Frezzotti et al. 2002a, b; Klügel et al. 2005). Fluid inclusion studies allowed to identify the presence of magma ponding levels in the lower oceanic crust and/or close to the Moho at a regional scale for most oceanic-island volcanic settings (De Vivo et al. 1988; Hansteen et al. 1998; Zanon 2015). For some oceanic volcanic islands (e.g., Pico and Faial, Azores archipelago) an additional level has been recognized in the lithospheric mantle (e.g., Zanon and Frezzotti 2013).

1.1 Fluid inclusion studies in volcanic systems

Fluid inclusions represent trapped fluids in rocks at different stages of their evolution, and can provide information on the pressure or temperature conditions of fluid entrapment (Roedder 1984; Touret 2001; Bodnar 2003). Fluid inclusions are closed volumes, in which pressure and temperature are interdependent variables. Pressure and temperature are related by the equation of state of the enclosed fluid, defined as a linear relation (isochore) in the P-T space (Roedder 1984) (Fig.1). Thus, if temperature is estimated by an independent method (e.g., homogenization temperature of coeval melt inclusions or by geothermometry of mantle xenoliths), then the pressure of fluid entrapment is obtained.

Not all fluid inclusions, however, preserve P-T trapping conditions. Some inclusions may undergo decrepitation and/or stretching, due to fluid overpressure (i.e., re-equilibration) (Roedder 1984; Vityk and Bodnar 1998; Bodnar 2003). Fluid inclusion re-equilibration occurs when external lithostatic P conditions are significantly lower than fluid internal isochoric conditions, which induces partial to complete fluid loss and/or an increase of inclusion volume, resulting in a decrease of fluid inclusion density (Roedder 1984). Decrepitation of inclusions is a complex process that depends on a number of variables, i.e., nature and density of the fluid, the mechanical strength of the host minerals, the size and distribution of inclusions (Bodnar 2003; Campione et al. 2015).

In volcanic systems, decrepitation of fluid inclusions is expected since the magma ascent is not isochoric (Fig.1; Frezzotti and Peccerillo 2004). In relatively fast rising magmas, inclusions are mostly decrepited (II in Fig.1c). Fluid density in inclusions undergoes a random re-equilibration, identifiable in a skewed distribution, where histograms show a broad "re-equilibration tail" (II in Fig.1a). In this case, which generally does not reflect a delay in decompression, representative fluid density data are confined to a minority of inclusions, generally of small size (< 3-5 μm, Fig.1b; Bodnar et al. 1989). Only if inclusion densities reset to a newly defined lower value (II in Fig.1d), and/or novel episodes of fluid trapping occur, a slowing down in the ascent rate of magmas may be

proposed, which corresponds to magma resting episodes (Zanon et al. 2003). Therefore, the occurrence of fluid inclusions with multiple well–defined Gaussian density distributions indicate the occurrence of several levels of magma ponding within a volcanic system (Frezzotti and Peccerillo 2004; Andersen and Neumann 2001; Klügel and Hansteen 2005; Frezzotti and Touret 2014).

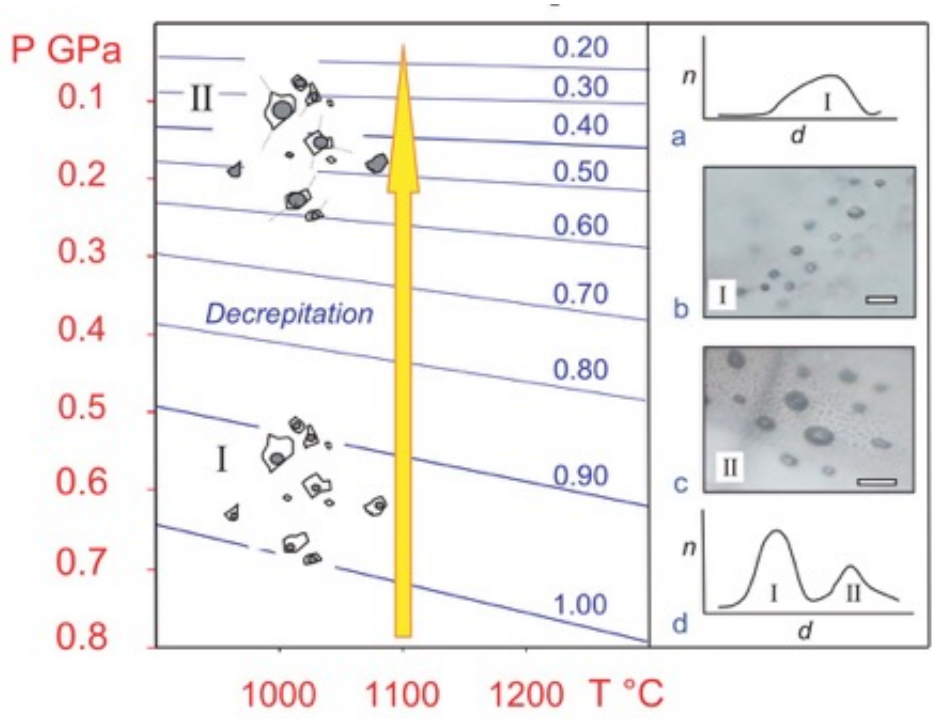

Fig.1 *P-T isochoric diagram with preserved (**b-I**) and re-equilibrated (**c-II**) fluid inclusions at different pressure conditions, to characterize the magma plumbing system of a volcano, and example of Gaussian distributions appreciable in the histogram representation (**a** and **d**) (modified from Frezzotti and Peccerillo 2004).*

In recent times, much progress in reconstructing the dynamics of magma ascent and rest in volcanic systems has been made, by combining fluid inclusion geothermobarometric studies with petrological and geochemical investigations. As an example, fluid inclusion studies in crustal xenoliths in lavas from Aeolian Island volcanoes (i.e., Lipari, Vulcano, Alicudi, Filicudi, Salina, and Stromboli) suggest two main magma accumulation levels in the continental crust at the regional scale, migrating in the crust according to magma differentiation (Belkin and De Vivo 1993; Vaggelli et al. 2003; Frezzotti et al. 2004b; Zanon et al. 2003; Bonelli et al. 2004; Zanon and Nikogosian 2004; Peccerillo et al. 2006; Di Martino et al. 2010).

2. AIMS OF THE THESIS

In this thesis a reconstruction of the magma plumbing system for the active volcano of El Hierro Island is proposed based on the geothermobarometry of fluid inclusions and petrological studies of mantle xenolith rocks. The main goal of this research is to improve the understanding and knowledge about the magma ascent dynamics in oceanic volcanic islands.

Various magma ascent and rest patterns have been reconstructed for different volcanic oceanic archipelagos based on geophysics, petrology, geochemistry, experimental petrology, and fluid inclusions. For Hawaii islands volcanoes, the presence of two main magma reservoirs has been identified beneath Kilauea; in this case initial deep stagnation of magma has been suggested in the upper mantle, followed by a second one in the crust (Ryan et al. 1988; Michon et al. 2015). At Canary, Madeira and Capo Verde islands, the models proposed indicate a residence of magma in levels located at lower crustal depths close to the Moho (Hansteen et al.1998; Schwarz et al. 2004; Gallip et al. 2006; Klügel and Klein 2006; Hildner et al. 2011, 2012; Longpré et al. 2014). The deeper mantle reservoir has not been clearly recognized.

El Hierro volcano (Canary Island), with the latest eruption in 2011-2012 (in the area of La Restinga, SE rift of the island), become one of the most important volcano of the recent times to study for better understanding of magma ascent dynamics in the oceanic volcanic islands. Many authors proposed different models where the presence of magma accumulation levels have been recognised at various depth in the crust or close to the Moho (Meletlidis et al. 2012; Becerril et al. 2013; González et al. 2013; Martí et al. 2013; Longpré et al. 2014; Meletlidis et al. 2015; Troll et al. 2015). Only Klügel et al. (2015), suggest for the first time the presence of a deep magma reservoir in the upper mantle. From this evidence the author proposed a reconstruction of the magma plumbing system, which can change during the evolution of the island. During the immature stage, the magma vertically ascends from deep reservoirs consisting of a system of individual magma pockets in the mantle and is directly erupted at the surface. In the mature stage, these deep mantle reservoirs tend to migrate upward and develop an oblate magma reservoir at the Moho. In the lower

crust, the formation of such an oblate reservoir may induce sub-horizontal movements of the magma in the crust (Clauge and Dixon 2000; Gudmunsonn 2006; Menand 2011; Gudmunsonn 2012). As a consequence, the magma is not confined into a well-defined accumulation zone for a long time, but can migrate with sub-horizontal paths, and eventually continue its rapid ascent toward the surface (Klügel et al. 2015). To confirm the entire evolutionary magma paths and consequently the growth of El Hierro oceanic volcanic island it is necessary an implementation of the information about the magma plumbing system of this island during its mature stage since data in literature are related only to the last 2011-2012 submarine eruption. Therefore, it is necessary an implementation of data and models characterizing different events of the Rift Volcanism cycle, as well as of the ancient volcanic activity phases. Accordingly, the aim of this thesis is to reconstruct the magma plumbing system by characterizing mantle rocks sampled in a lava flow in El Julan valley (40ka; Carracedo et al. 2001), recognized as part of the Rift Volcanism cycle. In addition, the data proposed can be used to implement monitoring strategies and the hazard evaluation of the island, which has ~11.000 inhabitants.

The model has been defined through the petrological characterization of mantle xenoliths and geothermobarometry of fluid inclusions trapped in these rocks. Peridotites studies included major elements composition, mineral phases geobarometer. To characterize the geochemical nature and geothermobarometric conditions of trapped fluids in the ultramafic xenoliths Raman microspectroscopy, microthermometry and mass-spectroscopy have been used.

The first part of the research concentrates on the petrology and geochemistry of peridotites, indispensable prerequisite to obtain a proper geochemical characterization of the lithospheric mantle. The second part of the research concentrates on the reconstruction of magma plumbing system of El Hierro Island based on fluid inclusion geothermobarometry.

The rationale of these two main lines of research (manuscripts 1 and 2) is briefly outlined below and the reader is referred to the attached manuscripts for a full description of methods, results and implications.

2.1 Petrological and geochemical heterogeneity of the lithosphere beneath El Hierro Island (*Manuscript 1*)

The geochemical nature of the lithospheric mantle can be revealed by petrological and geochemical investigations of peridotite xenoliths brought to the surface by basaltic magmas. In the case of the Canary Archipelago, the mantle lithosphere is dominated by spinel harzburgites and dunites, with subordinate lherzolites (Frezzotti et al. 1994, 2002a, 2002b; Neumann et al. 1995, 2000, 2002, 2004). Rare wehrlites and pyroxenites are also present (Hansteen et al. 1991; Neumann 1991; Neumann et al. 2004).

In the lithosphere beneath the Canary Islands, a first depletion process is suggested by the low Al_2O_3 and the high Cr_2O_3 content in pyroxenes and in spinel of peridotites (Neumann et al. 2004). According to these authors, the lithospheric mantle beneath the Canary Islands underwent a 25-30% depletion by melting processes related to the opening of the Atlantic Ocean (Neumann et al. 2004). At later stage, during the Canarian intraplate event, metasomatism affected the lithospheric mantle (Neumann et al. 2004). In harzburgites and lherzolites, modal, cryptic and Ca-metasomatism have been suggested based on the presence of minor phlogopite, on the enrichment of incompatible trace elements (e.g., LREE and MREE) in clinopyroxene, and on the presence of $CaO/Al_2O_3 > 1$ in rocks (Frezzotti et al. 2002a; Neumann et al. 2004). The highest degrees of metasomatic enrichments have been observed in the wehrlite rocks.

Metasomatism in the lithospheric mantle beneath the Canary Islands has been caused by carbonatitic or carbonaceous melts highly enriched in light rare earth elements (LREE), by high-Si melts and by a CO_2-rich basaltic melts (Neumann et al. 2004). This evidence has been supported also by fluid inclusion studies revealing the presence of volatile-rich, siliceous, alkaline carbonatite melts in peridotites. (e.g., Tenerife and La Gomera Island, Frezzotti et al. (2002a, b).

In this work, the characterization of the fluids trapped in peridotites of El Hierro Island has been proposed with the main aim to improve the knowledge on the chemical nature of the

matasomatic agents in the mantle lithosphere beneath the Canary Islands. Fluid inclusions have been investigated in dunites, lherzolites and harzburgites. They contain dominantly carbonate/sulfate/phosphate/spinel aggregates, with exsolved $CO_2 \pm N_2$, and are associated with carbonate + silicate glass inclusions and intragranular microveins.

Raman microspectroscopy analyses allow us to identify the different mineral phases of dolomite, Mg-calcite, anhydrite, sulfohalite (± other anhydrous and hydrous alkali-sulfates), apatite, and Cr-spinel in the inclusions, and to define the chemical composition and geothermobarometry conditions of the gas phases entrapped. The noble gas method (mass-spectroscopy) has been applied to highlights the presence of halogens in this type of fluid. Halogens, which are a still poorly explored marker of the lithosphere geochemical heterogeneity, can help to shed light on the processes giving rise to the metasomatic fluids in the lithospheric mantle.

2.2 The magma plumbing system beneath El Hierro Island (*Manuscript 2*)

The present research focuses on the mechanisms of magma ascent beneath El Hierro Island, one of the active volcanoes of the Canary Archipelago. Following the 2011-12 eruption an important multidisciplinary effort provided different magma dynamics models associated with this event (Meletlidis et al. 2012; Becerril et al. 2013; González et al. 2013; Martí et al. 2013; Longpré et al. 2014; Meletlidis et al. 2015). The resulting magma plumbing system is characterized by a complex ascent behaviour defined by levels of magma ponding in the oceanic crust and in the lithospheric mantle. The proposed magma ponding levels, determined using several independent techniques (e.g., fluid inclusions, mineral/melt chemistry, geophysics, analysis of feeder dykes and InSAR analyses) are summarized in Fig.2. In particular, Martí et al. (2013a, b) suggested, based on mineral/melt equilibria in basanites and on the seismic sequence record, the presence, in the mantle, of a deep-seated magma reservoir between 25 and 20 km, and a shallower level of magma accumulation in the crust, confined between 15 and 12 km (Fig.2e), the latest associated with a

lateral movement of magma of about 15–20 km by sill propagation. According to Klügel et al. (2015), sub-horizontal magma migration within the lower crust at the considered depths might explain the rapid endogenous island growth. Longpré et al. (2014) suggested a similar magma ascent dynamic beneath the island characterized by a main reservoir in the lithospheric mantle at 25-20 km and a shallower one in the oceanic crust at 10-5 km (Fig.2d), based on mineral/melt equilibria and fluid inclusion thermobarometry. Moreover, Becerril et al. (2013) estimated the source of erupting magmas in the oceanic crust from 14 to 7 km (Fig.2c) through a study based on the length-thickness ratios of feeder dykes. In addition, Gonzalés et al. (2013) identified two magma chambers in the crust between 9.5 and 4 km and between 4.5 and 2 km (Fig.2b) through the analysis of InSAR images and relative geodetic data, while Meletlidis et al. (2012) proposed the provenance of erupting magmas from 4 km (Fig.2a) using a chemistry-thermodynamic model on basanite and xenopumice samples.

Fewer models have been proposed for the volcanic activity before the 2011-2012 eruption. Neumann (1990) and Hansteen et al. (1991) suggested magma resting at similar depths in the crust (12 to 6 km, Fig.2g, h), based on geothermobarometry fluid inclusion studies on mantle xenoliths of Valverde cinder cones (NE of the island). More recently, Stroncik et al. (2009) proposed a multitude of small non interconnected magma chambers distributed over a depth interval of 35 to 10 km (Fig.2f), using the cpx-melt equilibrium of several basanites collected from the ocean floor of El Hierro Island.

Many questions on the dynamics of magma ascent of El Hierro Island are still unanswered. In particular, a careful analysis of data in Fig.2 shows well recognized magma ponding levels in the oceanic crust, while much less is known about the deeper lithospheric magma ascent. Moreover, many recent studies concentrate on the 2011-2012 eruption, neglecting to further characterize earlier eruptive activity, which could hold important information for a better understanding of the island evolution.

In this work, the petrological and geothermobarometric characterization of the mantle

xenoliths from the El Julan Valley (40ka; Carracedo et al. 2001) and the geothermobarometry studies of fluid inclusions trapped in these rocks allowed to define the magma ascent dynamics genesis from a depth of ~ 60 km till the surface, further identifying in the lithospheric mantle beneath El Hierro Island the presence of 1) a main magma reservoir and 2) a temporary magma accumulation at lower crustal levels.

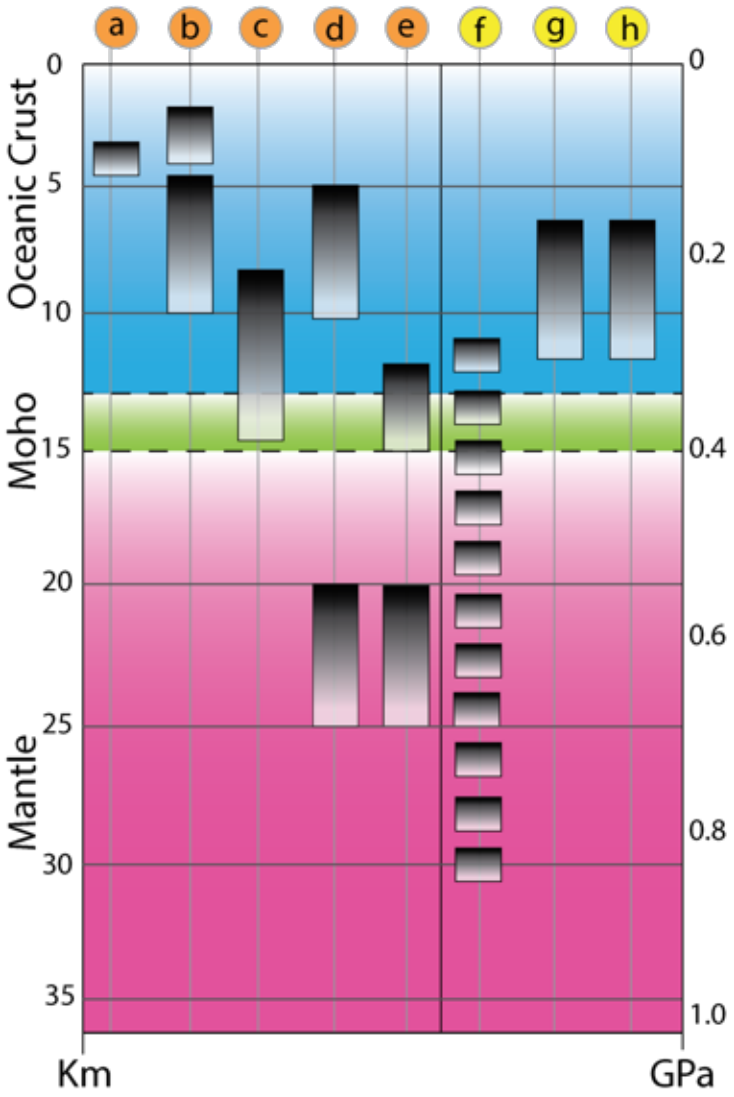

Fig.2 *Schematic representation for models of magma ponding levels in the lithosphere beneath El Hierro island from the literature. Black squares: depths of magma pounding in the crust and/or in the mantle; orange circles: 2011-2012 eruption; yellow circles: previous eruptions;* ***a*** *Meletlidis et al. 2012, based on geochemistry composition of xeno-pumices;* ***b*** *Gonzales et al. 2013, based on multifrequency and multisatellite interferometric data combined;* ***c*** *Becerril et al. 2013, based on length-thickness ratios of feeder dykes;* ***d*** *Longprè et al. 2014, based on experimental petrology and fluid inclusion thermodynamics;* ***e*** *Marti et el. 2013a, b, based on mineral/melt equilibria in basanites;* ***f*** *Stroncik et al. 2008, based on mineral-melt thermobarometry in glass and clinopyroxene;* ***g*** *Neumann 1990, based on geothermobarometry of fluid inclusions;* ***h*** *Hansteen et al. 1991, based on geothermobarometry of fluid inclusions.*

3. GEODYNAMIC AND GEOLOGICAL SETTING

The Canary Archipelago (Spain) is located on the continental rise off Cape Juby, west of northern Africa, in front of southern Moroccan coasts, and extends in a chain for roughly 500 km across the eastern Atlantic, between latitudes 27°N and 30°N, with its eastern edge only 100 km from NW African coast. The Canary Islands developed in a geodynamic setting characterized by Jurassic oceanic lithosphere formed during the first stage of opening of the Atlantic Ocean at 180-150 Ma and laying close to a passive continental margin on a very slow-moving African tectonic plate (Van den Bogaard 2013). The islands may be aligned along the contact between the continental crust on the east and the oceanic crust on the west (Heinrich 1988): Fuerteventura and Lanzarote at the eastern end of the archipelago are 100 km from the African coast, and El Hierro and La Palma at its western end are 500 km from the coast. Lanzarote and Fuerteventura are along the crest of the northeast trending Canary Ridge, on the upper continental rise at a water depth of about 2000 m. The rest of the archipelago, Gran Canaria, Tenerife, La Gomera, La Palma and El Hierro, at water depths of 3000 to 4000 m, are on oceanic crust of Jurassic age (Acosta et al. 2003). Gran Canaria, Tenerife and La Gomera islands have an East-West trend parallel to the oceanic fracture zone in this region, with Tenerife's long axis oblique to this trend. La Palma and El Hierro,

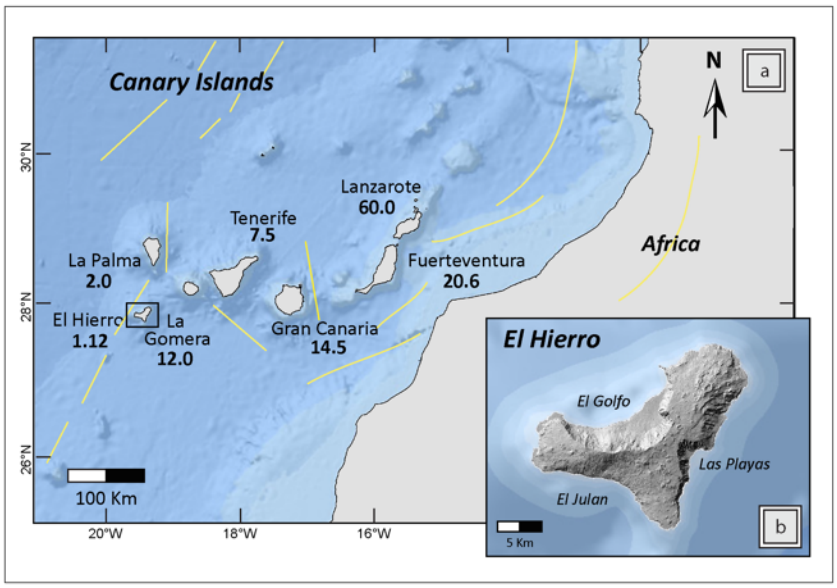

Fig. 3 *Geographical setting of Canary Islands showing location and age of the volcanic products, yellow lines define the main structures of Atlantic and African tectonic units, modified from Marinoni and Pasquarè (1994).*

at the western end of the island chain, are offset to the north and south of this trend (Fig.3).

The tectonic lineaments related to the Canary Islands can be divided into "African" (continental) trends (strikes: N20°E, N45°E, N75°E) and "Atlantic" (oceanic) trends (N160-N180°E, N120-N135°E) (Marinoni and Pasquarè 1994) (Fig.3). The most recent available seismic data in literature describes a change of crustal thickness and Moho depth beneath the different Canary Islands. Indeed, the Moho discontinuity deepens towards the east, varying in depth from 11.5 to 12.5 km beneath El Hierro and La Palma, to 20-30 km beneath Lanzarote and Fuerteventura (Martinez-Arevalo et al. 2013; Fig.4).

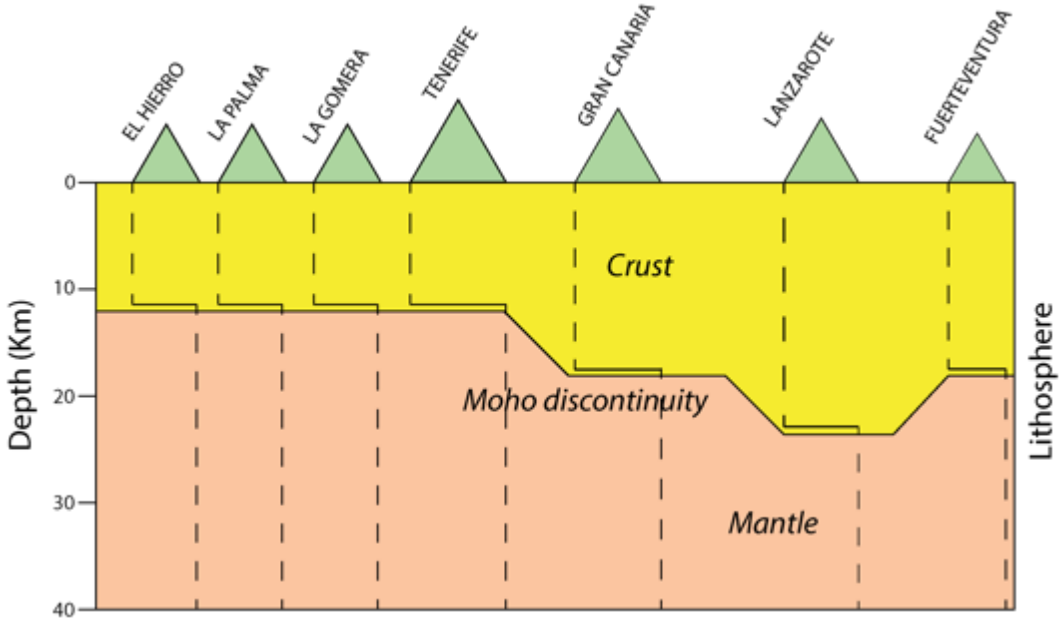

Fig. 4 *Geophysical characterization of the Lithosphere beneath Canary Islands, modified from Martinez-Arevalo et al. (2013).*

The magmatism of Canary Islands started in the Cretaceous (Seamount Canary Province from 133.3 ± 0.2 Ma, on a Jurassic basaltic crust of 160-155 Ma) while the sub-aerial volcanism of the main seven islands that forming the archipelago started at around 60 Ma ago, from Lanzarote, the oldest island of the archipelago. On El Hierro, the youngest island, the sub-aerial activity started 1.12 Ma ago (Robertson and Stillman 1979; Marinoni and Pasquarè 1994; Marinoni and Gudmundsson, 2000). The origin of the magmatism in the Canary Islands and its complicated space and time relationships have been a subject of debate still at current times. Many contradictory models, that including the presence of a hot spot, the propagation of a fracture from the Atlas

Mountains and the mantle decompression melting related to the uplift of the tectonic blocks, have been proposed to explain the origin of Canary Archipelago (Anguita and Hernán 1975; Schmincke 1982; Araña and Ortiz 1991; Hoernle and Schmincke 1992; Carracedo et al. 1998; Carracedo et al. 2001; Anguita and Hernán 2000; King and Ritsema 2000). Most recently van de Bogaard et al. (2013) proposed a shallow plate-bound mantle convection off the rifted NW African continental margin that explain the alignment, age distribution, plate tectonic setting, geochemical mantle components, and long history of individual centres of the Canary Islands seamount province.

The reconstruction of the geological history of the Canary Islands has been proposed from radio isotopic ages available starting from the 80's years (Carracedo 1979; Cantagrel et al. 1984; Ancochea et al. 1990; 1994; 2006; Guillou et al. 1996; 1998; 2004 Van den Bogaard and Schmincke 1998; Carracedo et al. 2001) and compared to other oceanic volcanic islands, such Hawaiian Islands (Carracedo et al. 1998; 1999) and Cape Verde (Carracedo et al. 2015). The stages of the island formation result to be similar in terms of structural features, including large rift structures and associated volcanism and giant landslide, and for their common origin from the probably mantle hot spots (Fig.5). Based on these features, Carracedo and Troll (2016) proposed that the single islands alignment initially considered due to the age progression of islands (Lanzarote from 60, Fuerteventura from 20 Ma, Gran Canaria from 14.5 Ma, La Gomera from 12 Ma, Tenerife from 7.5 Ma, La Palma from 2 Ma and El Hierro from 1.12 Ma is actually characterized by a "dual line" alignment due to a new trend of simultaneous islands formation of La Palma and El Hierro.

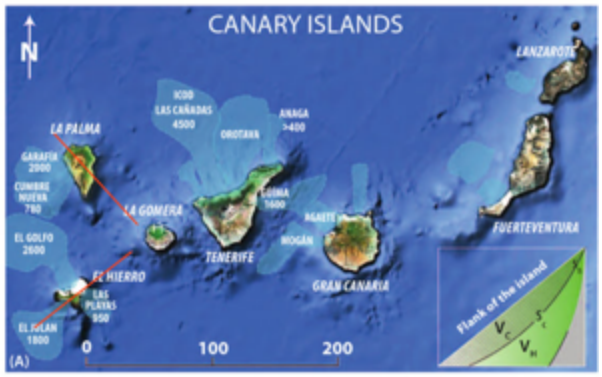

Fig. 5 *Probably hot spot progressions in Canary Island with the main giant landslides from bathymetric data. Red line in defines the "dual line" alignment of La Palma and El Hierro islands, modified from Carracedo and Troll (2016).*

El Hierro is the smallest and westernmost island of the Canary Archipelago. With an area of about 269 km^2, this volcanic island in its shield stage of growth raised from a depth of 3700-4000 m reaching a height of 1500 m a.s.l. (Carracedo 2001). The E-W alignment, the apparent progression of the Canaries, and the geochronological data appoint El Hierro as the youngest island of the archipelago. Sub-aerial volcanic products in El Hierro date back to 1.12 Ma (Guillou et al. 1996). Latest $^{40}Ar/^{39}Ar$ data for submarine trachyte breccias with an age of 133.3 ± 0.2 Ma in the southern El Hierro Ridge oceanic floor and in the northern flank indicate submarine volcanic activity starting from the Early Cretaceous (Van den Bogaard 2013; Fig.6).

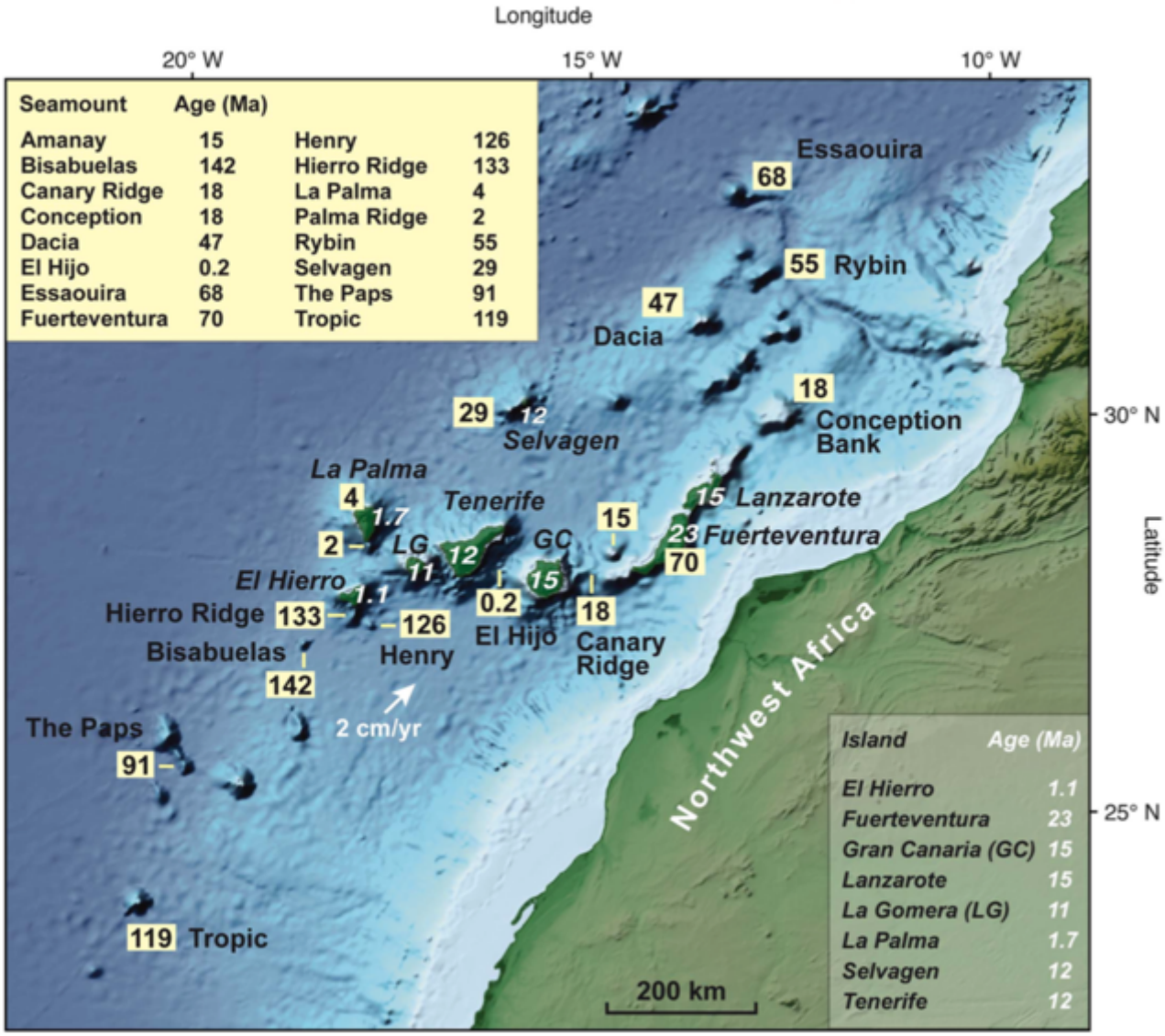

Fig. 6 *Topographic map of the NW African continental margin and age distribution in the Canary Island Seamount Province, with El Hierro Ridge underlined in red; Van de Bogaard (2013).*

The current morphology of the island describes the presence of three main rifts arranged at 120° from each other (Gee et al. 2001) (Fig. 7). The presence and the relative evolution of a three armed rift, recognized in several islands of Canary Archipelago (e.g., Tenerife and La Palma island) and as well as in Hawaii Islands (e.g., Mauna Loa, Kilauea, and Kohala islands) has been also proposed for El Hierro Island. Three main theories have been suggested: the first one identifies a rift development as a result of local stresses generated by the pushing action of up-doming magmas (Carracedo et al. 1994); the second suggests a gravitational spreading control on rift zones and flank instability, (Münn et al. 2006); the third one proposes a strong control by regional tectonic structures (strikes: N20°, N160-180°E, N120-N135°E; Geyer and Martí 2010).

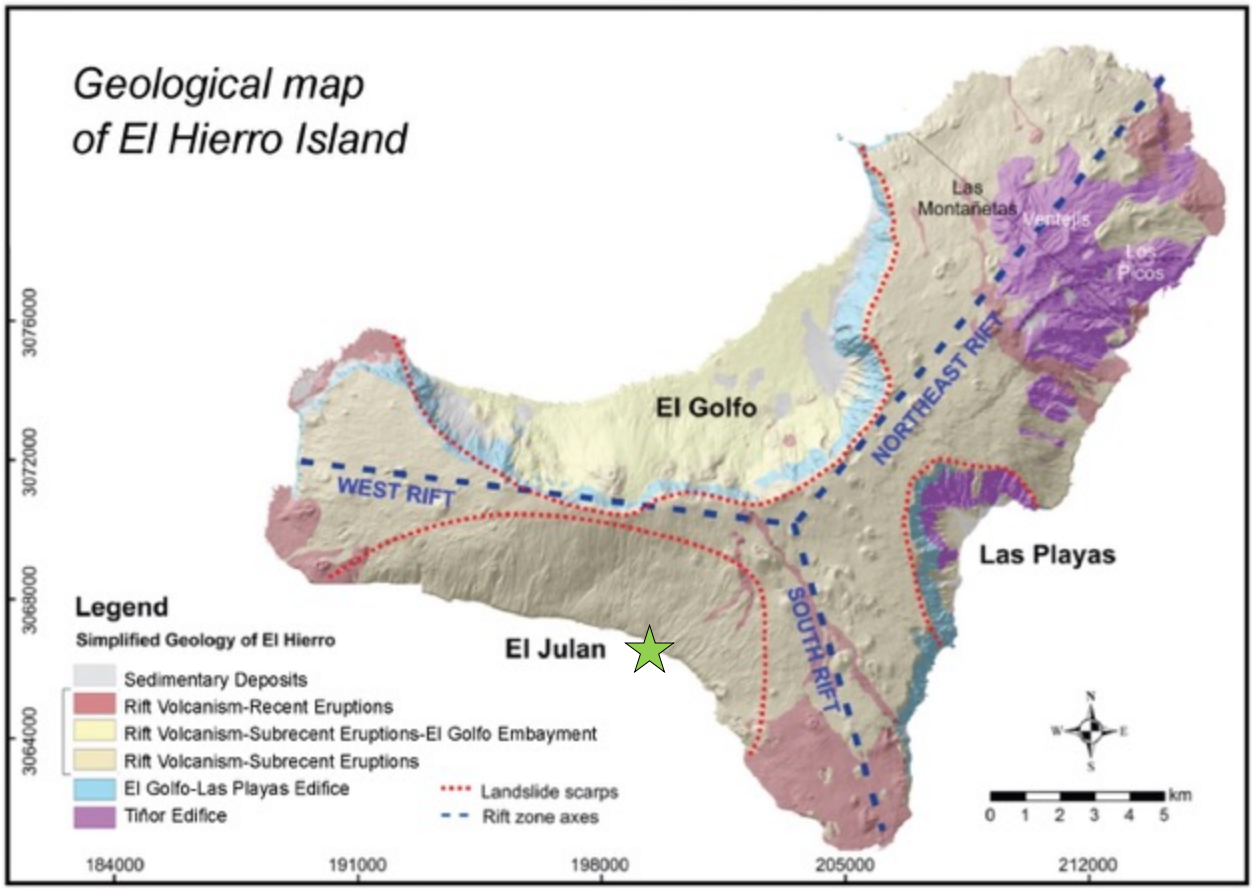

Fig. 7 *Geological map of El Hierro Island. Different volcanic cycles are present in legend. The three armed rifts are in bleu lines and main giant landslides in red, modified from Becerril et al. (2015); the green star indicates the outcrops of lava flow rich of mantle xenoliths in El Julan Valley.*

Recently, Becerril et al. (2015) proposed a characterization of the structural evolution of El Hierro Island, where the radial structures defined by a uniform stress fields during the constructive episodes result conditioned by the combination of gravitational spreading, overburden pressure, stresses induced by magma ascent in each of the volcanic edifices, confirming the presence of the three armed rift on the island (Fig.7). Conversely, in the shallower parts of the edifice the structures with strikes NE–SW, N–S and WNW–ESE reflect local stress fields related to the formation of giant landslides and able to mask the general and regional stress field.

The most widely accepted interpretation of El Hierro geology is based on three main volcanic cycles, namely Tiñor Edifice (1.12 - 0.88 Ma), El Golfo-Las Playas Edifice (0.545 - 0.176 Ma), and Rift Volcanism (0.158 Ma - Present) (Carracedo et al. 2001; Becerril et al. 2013b) (Fig.6). The cycles are separated by periods of quiescence, structural deformation and sector collapses. Four main collapses have been identified as Las Playas I and II (~545 - 0.176 Ma and 0.176 - 0.145 Ma respectively), El Julan (< 0.158 Ma) and El Golfo (~87 - 39 ka) (Masson 1996; Masson et al. 2002; Masson et al. 2006; Gee et al. 2001; Longpré et al. 2011). Two additional smaller landslides have been proposed occurring between Tiñor Edifice and El Golfo-Las Playas Edifice, at around 0.8 and 0.5 Ma, in the northern side of El Tiñor Edifice [Carracedo et al. 2001; IGME (Instituto Geológico y Minero de España) 2010a, b, c, d)].

The Tiñor Edifice forms the first stage of sub-aerial growth of El Hierro Island. Its outcrops are confined to the NE flank of the island and inside Las Playas collapse. The E flank of this apparatus is affected by faults forming a graben system (IGME 2010a; Becerril et al. 2015). The activity of this edifice is characterized by a consistent compositional variation that may reflect the morphological evolution of the developing edifice: a basal unit of relative thin, steeply dipping flows, probably corresponding to the initial stage of growth of the volcano, characterized by steep flanks; an intermediate unit of massive lavas, with a progressively trend to sub-horizontal flows in the centre of the edifice, that has been interpreted as the lower slopes of this mature stage of growth, and than sometimes fill the canyons on the flanks; the final unit is characterized by thin lava flows

from emission vents on the top of the edifice, and its last stages of activity identified as the incipient development of the three armed rift (Carracedo 1998, 2001; IGME 2010a; Becerril et al. 2015).

The El Golfo-Las Playas Edifice was imposed after the collapse of Las Playas. This edifice take place filling the NW-facing collapse embayment and finally spilling lavas towards the E cost overlaying the El Tiñor Edifice. Two sub-units can be identified in this volcano from morphological differences and local development unconformities: the basal unit is composed of strombolian and pyroclastic cinder cones with subordinate lava flows; the upper unit is predominantly composed of thin lava flows. The duration of growth of El Golfo- Las Playas Edifice have been estimated to be about 360-380 ka as indicates by the lower age (545 ka) and most recent (176 ka) trachytic lavas of this cycle proposed by Guillou et al. 1996 in the collapse scarp of Las Playas. In addition, the geochronological data available in the NE sector of the island are able to propose an important break of the volcanic activity between the Tiñor Edifice and El Golfo-Las Playas Edifice from 880 and 545 ka (Carracedo 2001; Carracedo and Troll 2016).

The Rift Volcanism cycle is identified as the last growing stage of El Hierro Island. This period of volcanic activity is characterised by eruptions occurring equally along the three rifts (Carracedo et al. 2001; IGME 2010). The emergent parts of these rifts are characterised by steep narrow ridges formed by clusters of cinder cones and which internal structure is characterised by dyke swarms (Carracedo et al. 2001; Galindo et al. 2012; Becerril et al. 2015). As a results of a wide distribution of vents, a sequence of thin basic lavas has covered much of the topographical surface of the island (Fig.7). These lava flows have largely filled the El Julan collapse and partially also the embayment of El Golfo. For the Rift Volcanism cycle the period of activity is constrained from 158 ka to 2500 years AD; the eruptive rates are relatively moderate and continuous. The eruptions of the Rift Volcanism cycle can be divided in two different stages: eruption older than the Holocene (158 ka- 2500 years AD) have been defined as “sub-recent eruption”, while those occurring later (11,700 AD-Present time) have been indicated as “recent eruptions”. The recent sub-aerial volcanism of El Hierro Island is characterize by monogenetic cones with effusive magmatic

eruption of basic composition, as well as Hawaiian-Strombolian episodes fed by sub-vertical dykes (Becerril et al. 2013; 2015), that may be combined with hydromagmatic eruptions (Becerril 2009). The island eruptions have been mainly mafic in nature as well as the intrusion of sub-volcanic bodies ranging in composition from foidite to basanite (Pellicer 1977; Aparicio et al. 2003; Stroncik et al. 2009), which have generally erupted along the rift zones.

In addition to the sub-aerial volcanism, bathymetric studies proposed by Gee et al. (2001) revealed a significant number of well preserved volcanic cones sited on the submarine flanks of the island, suggesting that a significant submarine volcanic activity also occurred in recent times. This observation has been confirmed by the latest eruption taking place on the submarine south rift of the island, 2 km off the coast of El Hierro in "Las Calmas sea", close to "La Restinga village", and lasting from the 10th of October 2011 to the end of February 2012, albeit the official declaration of the eruption's end was the 5th of March 2012 (Martí et al. 2013a). This eruption has been the first fully and systematically well-monitored volcanic eruption in the Canary Islands by the National Geographic Institute (IGN) (López et al. 2012). No clear evidence of events over the last 600 years (historical period) has been found on the island, except this last submarine volcanic event and a questionable eruption in 1793 at the northwest of the island called "Lomo Negro volcano" (Hernández Pacheco, 1982) that most probably was an offshore eruption which produced an intense seismicity phase felt by the population (Romero and Guillén 2012).

A compilation of all geochronological information (e.g. Abdel-Monet et al. 1972; Guillou et al. 1996; Széméta et al. 1999; Carracedo et al. 2001; Longprè et al. 2011; Lopez et al. 2012; Rodriguez-Gonzàlet et al. 2011) of the El Hierro Island has been provided by Becerril et al. (2016) (Fig.8), which proposed also new $^{40}Ar/^{39}Ar$ and ^{14}C ages for the product of El Tiñor Edifice and the Rift Volcanism cycle, providing an estimation of the eruption recurrence for the last 33ka.

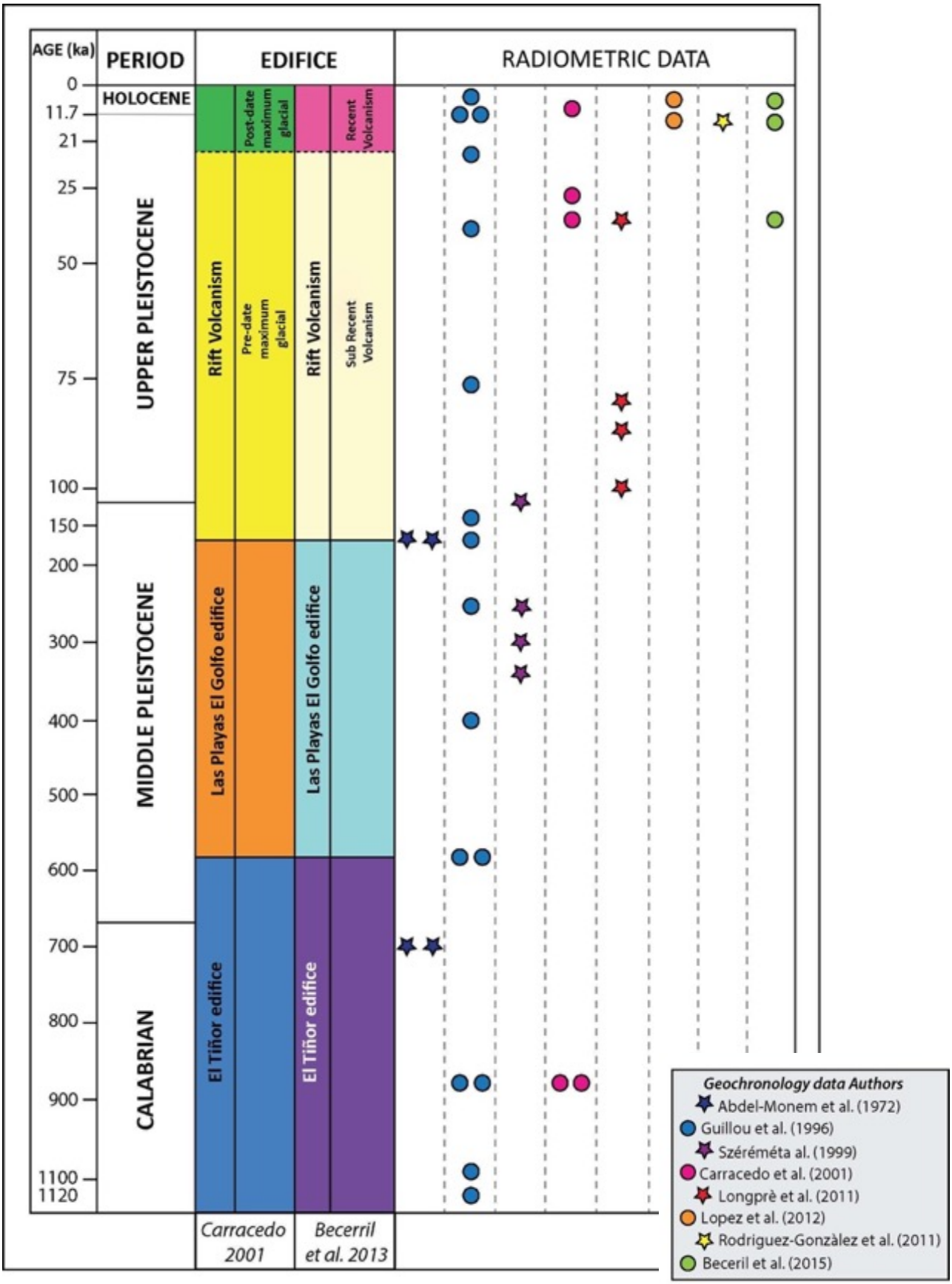

Fig. 8 *Chronostratigraphic chart for the volcanism on El Hierro Island, (modified from Becerril et al. 2016). In legend are reported all geochronological data proposed by the different authors, correlated at the three main cycle-edifices proposed by Carracedo (2001) and Becerril et al. (2013). Different colours of the geology sequence edifice are reported according on the maps proposed by the authors.*

Xenoliths rich lava flow in El Julan valley

The xenolith rocks collected in a lava flow in the area of El Julan valley (SSW) have been object of study in this thesis (green star in Fig.7). El Julan valley located between the south and the west rift of the island is affected by one of the three main sector collapses that affect the morphology of El Hierro Island.

Few structural evidence on the surface are presents, but the affection of landslide in this area has been confirmed by bathymetric data proposed by Masson et al. (2002). Indeed, El Julan valley is characterized by the presence of overlapped lava flows succession of the Rift Volcanism cycle that have largely filled the depression imposed from the collapse, hiding the the scarp of the sector collapse (Fig.9).

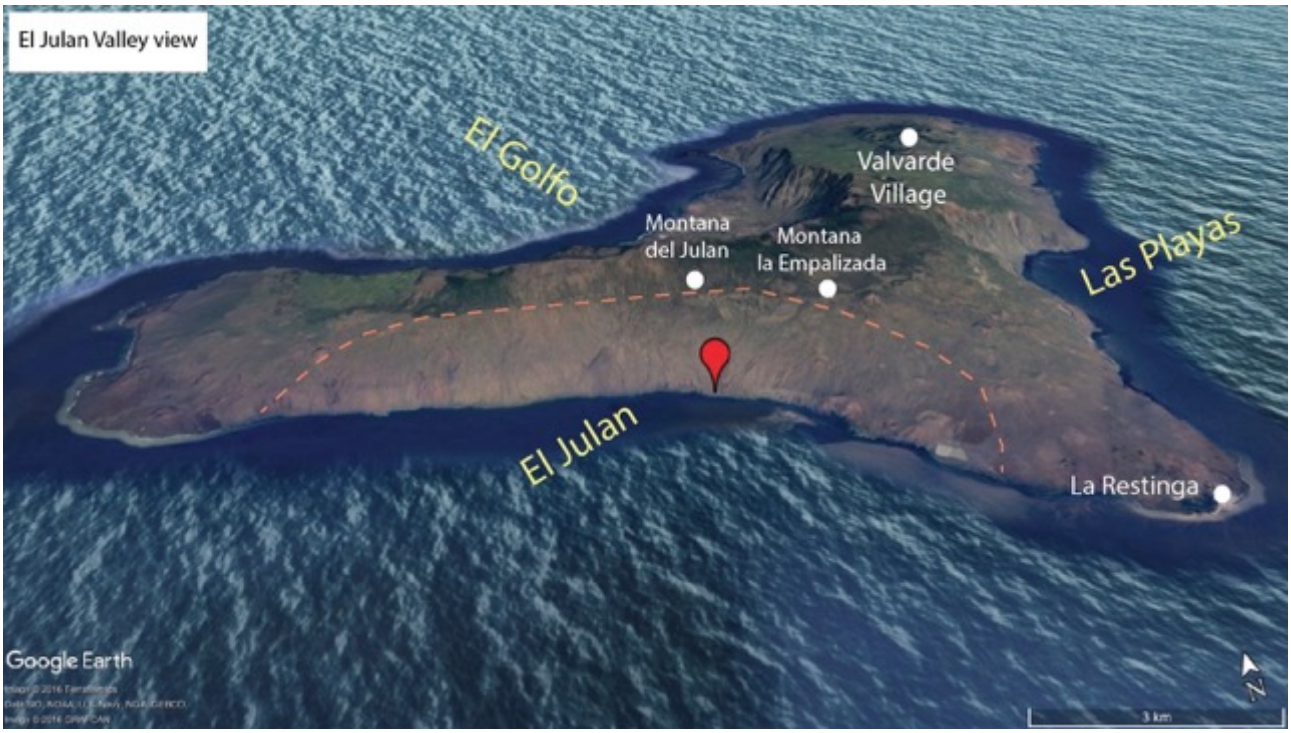

Fig. 9 *El Julan Valley view. The red place-card localized the outcrop studied in the area of El Julan collapse. Trace of the scarp- collapse is identified in orange dashed line.*

The outcrops where the xenolith rocks have been collected are located along an abandoned road (at about 200m a.s.l) used to investigated the presence of groundwater. Three tunnel for water investigation called “Los Jables”, “El Julan” and “Las Alcusas” are present at a distance of ~1 km

each other (Fig.10). The outcrop with the xenoliths rich lava flow is located close to the "El Julan" tunnel at ~ 20m a.s.l, along to the coast line (27°41'27"N - 18°02'49"W). This basaltic lava flow (dipping about 20° to SW) reaches 3m in thickness and locally pyroclastic deposits of scoria cone are presents (Fig.11a, b). The lava flow is extended along the street for ~ 500 m.

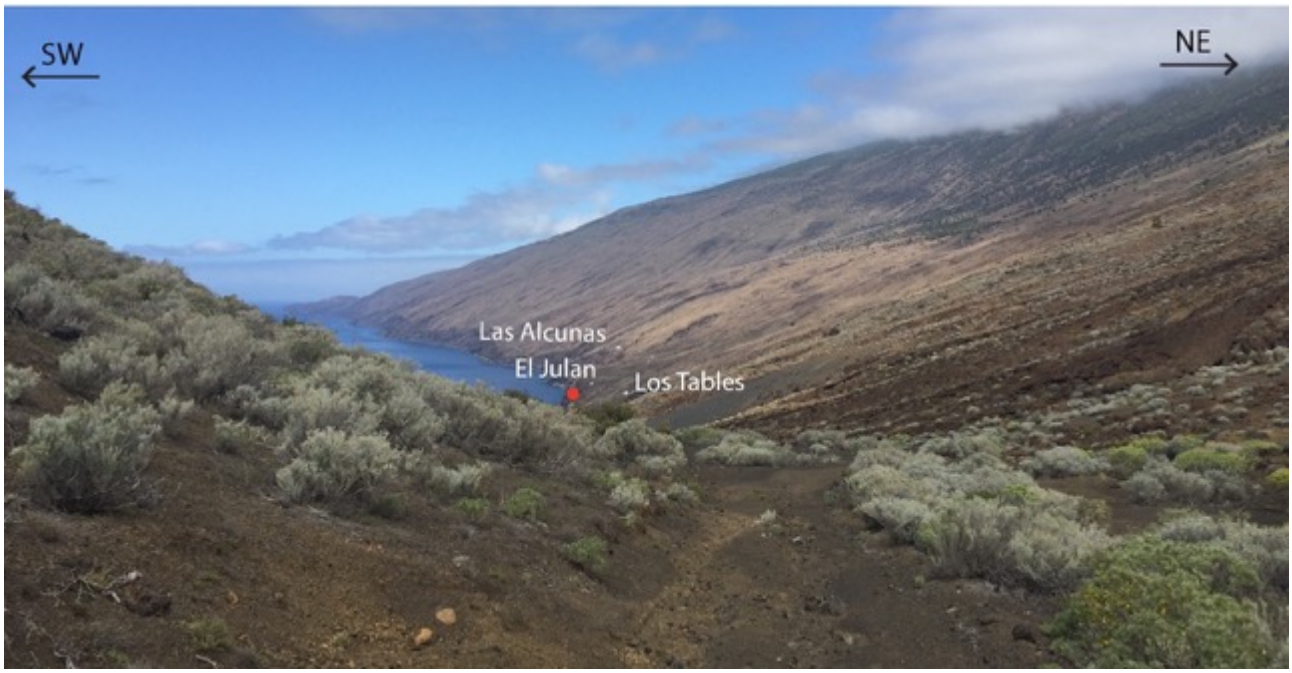

Fig. 10 *Panoramic picture of El Julan Valley The red place-card localized the outcrop close to the water tunnel for water investigation called "Los Jables", "El Julan" and "Las Alcusas.*

The basalt is porphyritic with dark grey groundmass and olivine phenocrysts of mm-sized. Ultramafic xenoliths in the lava host are from sub-angular to angular in shape and about 10 cm in size on average. They have a pale green colour, characteristic for fresh peridotites (Fig.11c). This lava flow has been related to the Rift Volcanism cycle based on geological maps, altitude of the flow and available radiometric data. About 1 km south-western of the sampled xenolith rich lava flow Carracedo et al. (2001) present 2 K-Ar radiometric ages (SJ 01 41±2 ka and SJ 02 31±2 ka) related to two lava flows that form a continuous lava flow succession without any important unconformity inside. Therefore, the investigated xenoliths rich lava flow belongs to this succession and presents an are of age of 40 ka. The eruptive fissure related with this lava flow can be suggested to be on the top of morphological hillside in the area between "Montana del Julan" and "Montana la Empalizada". The studies about the location of this eruptive fissure are still in progress.

Fig. 11 *Outcrop of El Julan valley;(a) xenoliths rich lava flow; (b) base of the lava flow with a paleo soil; (c) detail of the ultramafic xenoliths in the host lava.*

4. ANALYTICAL APPROACH

The research presented in this thesis has been carried out using a range of classical and cutting-edge petrological and geochemical analytical techniques. These include chemical analysis of minerals, and subsequent thermobarometric modelling. Fluid inclusion analyses by microthermometry and Raman microspectroscopy have a central role in this thesis. A short description of the main methodologies applied is summarized in the following paragraphs.

4.1 Mineral chemistry and geothermobarometry of peridotites

Major elements composition of mineral phase in mantle xenoliths have been performed using a wavelength Dispersive System (WDS) microprobe, a JEOL JXA 8200 Superprobe, equipped with five wavelength-dispersive spectrometers, Energy Dispersive X-ray Spectroscopy (EDS), and cathode luminescence detectors at University of Milan. The operating conditions consist of an acceleration voltage of 15 kV, at a beam current of 15 nA at 30s counting time for element, with a spot size of 1μm. The typical detection limit for each element was 0.01%. Natural and synthetic minerals have been used as standard during the calibration phase of the instruments. Structural formulae of minerals have been processed through the software NORM (Ulmer 1986). Analysis have been made considering rim and core of the single mineral phase in spinel lherzolites and harzburgite rocks.

Different thermometers proposed in literature are based on thermodynamics model and experimental data calibrated at high- T and P conditions with systems that approximate the typical composition of the minerals of mantle xenoliths. The geothermometers by Wells (1977), (considering the partitioning of Fe^{2+}, Mg and Ca between orthopyroxene and clinopyroxene), by Brey and Koehler (1990), (with the solubility of Ca and Al in orthopyroxene in equilibrium with olivine) and by Witt-Eickschen and Seck (1991), (based on the equilibrium between clinopyroxene and spinel) have been chosen to characterized the mantle xenoliths. Pressures conditions of mantle

rocks have been attributed through the Koehler and Brey (1990) geobarometer, which considers the diffusion of Ca in olivine in spinel peridotites.

4.2 Fluid inclusions studies

The study of fluid inclusions has been performed following the analytical procedure proposed by Touret and Frezzotti (2003). The characterization of the different generations of fluid inclusions has been obtained on the basis of textural features: two main fluid inclusion assemblages have been observed:

- *Type I:* early multiphase-CO_2±N_2 fluid inclusions, occur either in small and spatially isolated clusters or as intragranular trails;
- *Type II:* late CO_2 fluid inclusions, occur both as intragranular and intergranular trails of variable length.

Fluid chemical composition and density have been obtained by observation of the temperature at which phase changes occur in a fluid inclusion upon heating. Fluid inclusion study has been performed by microthermometry measurements carried out with a Linkam THMS600 heating/freezing stage at the University of Milan Bicocca.

Recorded temperatures include:

a) Temperature of melting T_m (i.e., triple point temperature) for pure CO_2.
b) First melting T_e (eutectic) or T_i (initial) for binary or higher fluid systems.
c) Temperature of final melting T_f (final) for binary or higher fluid systems.
d) Temperature of homogenization into the liquid Th_L (L+V → L)
e) Temperature of homogenization into vapour Th_V (L+V → V)
f) Partial homogenization in presence of solid CO_2 Th_S (S+L+V→S+L)
g) Temperature of sublimation T_S (S+L→L)

The density of the CO_2 fluid was calculated on the basis of the equations of Duschek et al. (1990) with BULK software. Isochores for a pure CO_2 fluid were calculated through the application of the equation of state of CO_2 of Holloway (1981) with ISOCHORE software.

Fluid inclusions have been further characterized with a Horiba Labram HR800 Raman microspectrometer, at the University of Turin. A polarized Nd green laser operating at 532 nm wavelength and 80mW incident power was used as the excitation source, with a spot size resolution of 1x1x3 μm. The slit width was 100 μm, and the corresponding spectral resolution was ±1.5 cm^{-1}. CO_2 Raman spectra have been collected with a 100× objective and 30s acquisition times (3 accumulations per spectrum). The calibration of the instrument has been daily checked, using the 521 cm^{-1} silicon band. This analytical technique has been used to obtain the chemical composition and the relative amounts (in molar fractions) of fluids, and to identify daughter minerals in fluid inclusions. This non-destructive technique allows to analyse liquid, gaseous and solid phases, and solute species in inclusions as small as 1 μm in diameter, that is a resolution not possible by conventional petrography and microthermometry (Burke and Lustenhouwer 1987; Dhamelincourt et al. 1979; Dubessy et al. 1982; 1989; Pasteris et al. 1986; 1988; Rosasco et al. 1975; Seitz et al. 1987; Burke 2001; Frezzotti et al. 2012).

The fundaments of Raman spectroscopy were demonstrated by Raman (1928) based on the inelastic scattering of light resulting from the interaction of photons and molecules. If the scattered light has frequency υ_1, Rayleigh or elastic scattering occurs when no energy is lost; on the other hand, if there is a change in the lower (υ_1-υ_m) and higher (υ_1+ υ_m) frequencies – known as anti-Stokes and Stokes lines respectively – inelastic scattering or Raman effect takes place. The latter ones give more intense Raman scatter, and are generally measured by Raman spectroscopy and translated into a spectrum of anelastically scattered light intensity (in arbitrary units or counts) versus the shift of frequency of scattered light (in $1/\lambda$ in $cm^{-1)}$ (Frezzotti et al. 2012, and references therein). The vibrational energies of the molecules (i.e., the nature of the bonding) translate to bands

in a Raman spectrum.

In mixed CO_2-N_2 fluid inclusions Raman band recorded at 2330-2228 cm^{-1} for N_2 and at 1280 cm^{-1} for CO_2. The relative molar fractions of the two end-members have been calculated following Burke (2001). The molar fractions (X) of end-member components in a gas mixture can be obtained using the following equation:

$$X_a = \frac{\frac{A_a}{\sigma_a \zeta_a}}{\sum \frac{A_i}{\sigma_i \zeta_i}}$$

where X_a is the molar fraction, A_a the band area, σ_a the Raman cross-section and ζ_a the instrumental efficiency for gas, while $\Sigma A_i \sigma_i$, and ζ_i represent the sum of values for all gas species in the fluid inclusion. Molar volumes of CO_2-N_2 have been derived by plotting fluid composition and measured sequences of phase transitions in the CO_2-N_2 T-X diagram (van den Kerkhof 1989; Klemd et al. 1992).

Raman microspectroscopy characterization has been carried out on the daughter minerals identified into the fluid inclusions. The presence of carbonates, sulphates, phosphates and spinel has been characterized by the single acquisition of spectra and through the distribution and (qualitative) relative abundances proposed by Raman mapping. Characterization of the different mineral phases has been obtained following Frezzotti et al. 2012. Single Raman map (40x40µm square region with a spot stepped of 2 µm; objective x100 µm) has been first acquired for each mineral phase, based on a colour intensity scale (from blue, minor intensity, to yellow, major intensity; Fig. 12A), which reflects the increase in thickness of the phase. Raman maps of single phases have been then combined inside each inclusion, based on Raman results and optical observations (Fig. 12B, C).

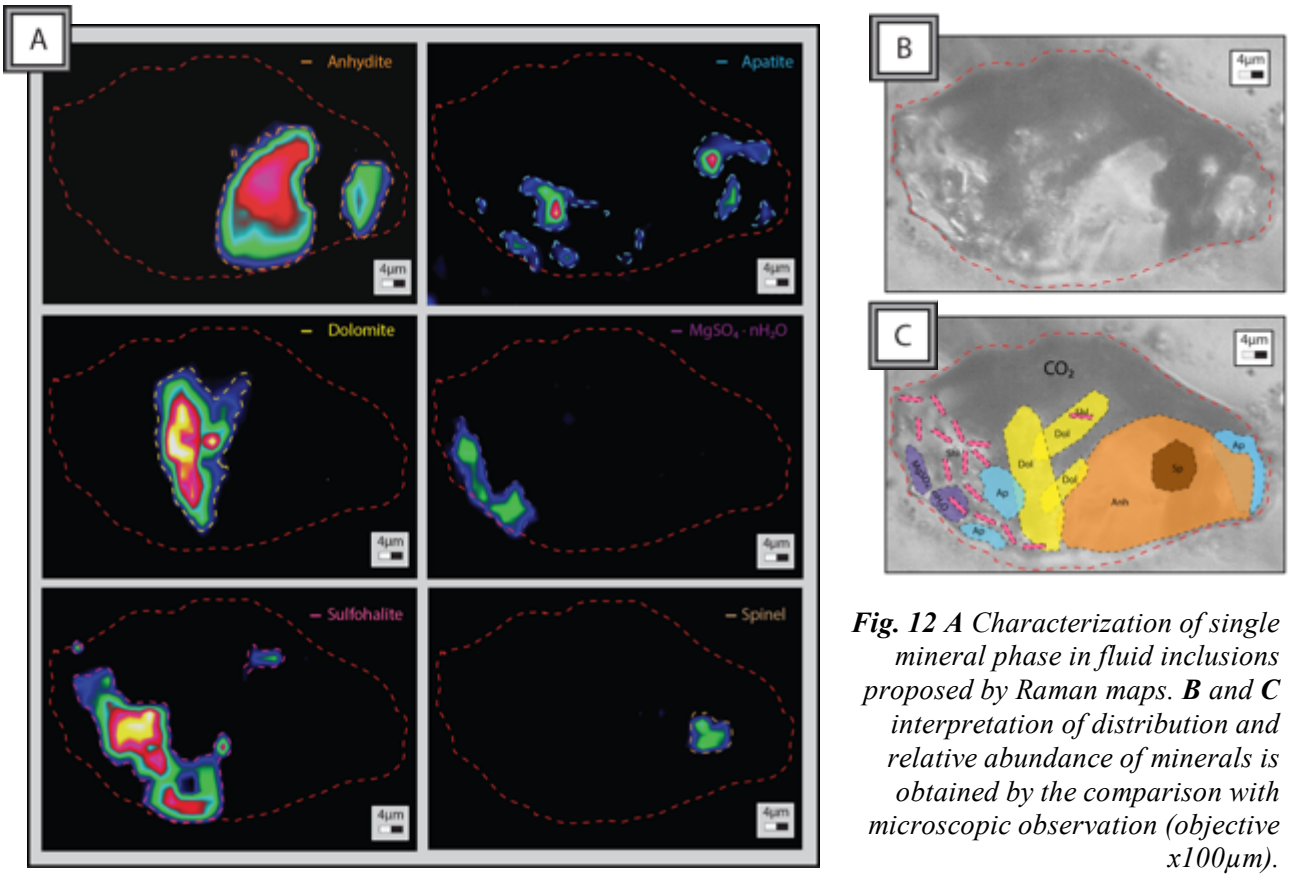

Fig. 12 A *Characterization of single mineral phase in fluid inclusions proposed by Raman maps.* ***B*** *and* ***C*** *interpretation of distribution and relative abundance of minerals is obtained by the comparison with microscopic observation (objective x100µm).*

4.3 Evaluation of CO_2 density by Raman Microspectroscopy (Raman densimeter)

Density of pure CO_2 fluid inclusions with sizes < 3µm has been calculated by Raman spectroscopy based on the distance between the two main CO_2 bands (Δ in cm^{-1}) (Rosso and Bodnar 1995, and references therein). The CO_2 Raman spectrum, described in Fig.13, shows two sharp bands at about 1285 (v1) and 1388 cm^{-1} (v2), depending on fluid density, and two symmetrical weak bands below the 1285 and above the 1388 cm^{-1} band, defined as hot bands (Colthup et al. 1975; Dhamelincourt et al. 1979; Dubessy et al. 1999; Rosasco et al. 1975; van den Kerkhof and Olsen 1990). A small peak at 1370 cm^{-1} is the $^{13}CO_2$. The presence of two main bands in the CO_2 spectrum was defined by Fermi (1931) as a resonance effect. The distance between the two main CO_2 bands, i.e., Fermi doublet, (Δ in cm^{-1}; Fig.13) is proportional to the CO_2 density: at the

increment of the Δ split corresponds an increase of density (Bertránd 1983; Garrabos et al. 1980; van den Kerkhof 1988b; Wang and Wright 1973; Yamamoto et al. 2006). The presence of other gas components in the fluid inclusions in addition to CO_2 (e.g., CH_4 or N_2) affects the Δ value, which does not show linear relation with density.

Several equations have been proposed, i.e., "Raman densimeter", such as Rosso and Bodnar 1995; Kawakami et al. 2003; Yamamoto and Kagi 2006; Song et al. 2009; Fall et al. 2011; Wang et al. 2011. CO_2 density can be determined in the range from 0.1 to 1.24 g/cm^3 with an accuracy better than 5% (Wang et al. 2011). A very good agreement has been observed between density data derived from Raman spectroscopy and from microthermometry, also for CO_2 fluids containing minor amounts of other gaseous species (i.e., 5 mol% CH_4 or N_2; Frezzotti and Peccerillo 2007).

Before applying the Raman densimeter, 34 fluid inclusion densities were double checked by microthermometry and Raman analyses in the interval from 1.00 to to 0.84 g/cm^3. By comparing microthermometric and Raman densities the most appropriate densimeter resulted to be the one proposed by Kawakami et al. 2003, which has an operating range of densities up to 1.24 g/cm^3 with relative accuracy in the density values definition of 0.01 g/cm^3. Although the precision of microthermometric measurements is higher, the Raman densimeter permits to analyse very small fluid inclusions (< 3-5 μm in diameter).

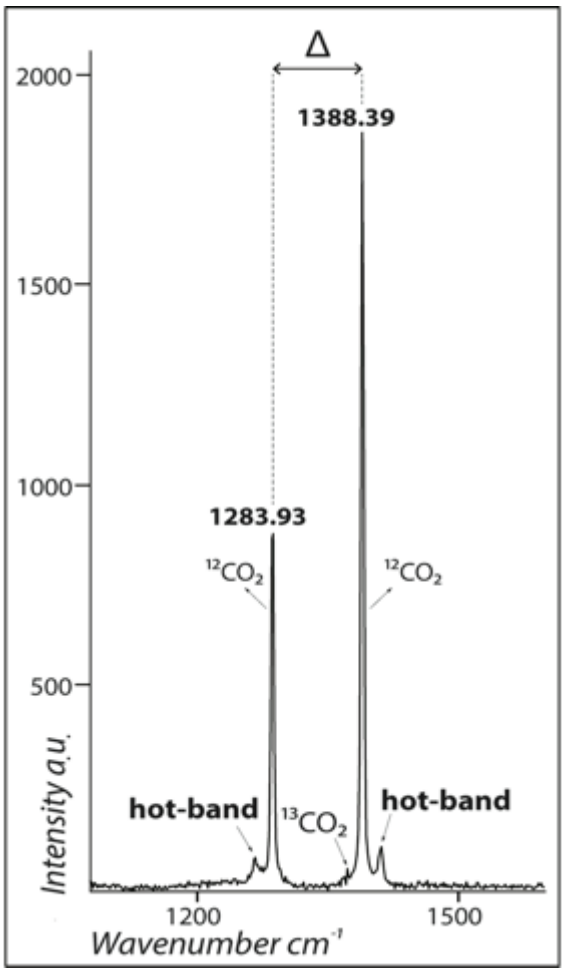

Fig. 13 *Spectra of CO_2 fluid inclusion.*

4.4 Halogens mass spectroscopy

The investigation about the halogens in fluid inclusions has been proposed in this thesis through the technique of *mass spectroscopy (noble gas method).* The measurement of halogens (Cl, Br, I and Ba), has been carried out by irradiating samples with neutrons and measuring artificial noble gas isotope, respectively, ^{38}Ar, ^{80}Kr,^{128}Xe and ^{131}Xe, through a noble gas mass spectrometer (Jeffery and Reynolds 1961; Kendrick 2012 and references therein) (Fig.14). Analysis have been performed through a Noblesse™ mass-spectometer by NuInstruments™, equipped with one Faraday cup and one MasCom™ ion counter (at University of Milan Bicocca).

As regards the mass-spectroscopy analyses, a standard with independently known target element concentrations have been used to translate acquired raw noble gas data – yielded by the acquisition software in counts per second [CPS] – into element concentrations (in the present case Cl, Br, Ba, I and U) in each sample. Scapolite (SY) have been used as standard (Kendrick et al. 2012; 2013). Five steps of heating have been performed to achieve a temperature of 1500 °C, to reach the decrepitation of fluid inclusions as predicted by Roedder (1965). Indeed, in steps 4 and 5 (1200 and 1400 °C), a spike following a decreasing trend in noble gases indicates that the fluid inclusions are decrepitating, releasing radiogenic Ar, Kr and Xe concentrations in the fluids. It is possible to calculate halogen concentrations in the samples and their ratios by referring to a standard with known concentrations of halogens and previously irradiated.

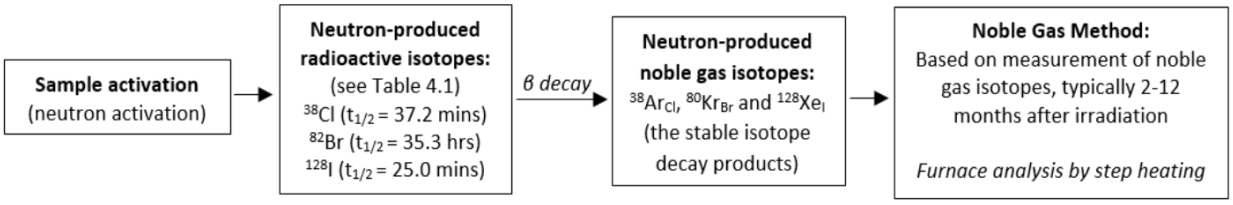

Fig.14 *Steps followed for the noble gas method. Modified from Kendrick et al. (2012).*

REFERENCES

Abdel-Monem A, Watkins ND, Gast PW (1971) Potassium-argon ages, volcanic stratigraphy, and geomagnetic polarity history of the Canary Islands: Tenerife, La Palma, and Hierro. Amer J Sci 272:805–825. http://doi.org/10.2475/ajs.272.9.805

Acosta J, Uchupi E, Muñoz A, Herranz P, Palomo C, Ballesteros M, Working ZE (2005) Geologic evolution of the Canarian Islands of Lanzarote, Fuerteventura, Gran Canaria and La Gomera and comparison of landslides at these islands with those at Tenerife, La Palma and El Hierro. Mar Geophys Res 24:1–40. http://doi.org/10.1007/s11001-004-1513-3

Ancochea E, Hernán F, Cendrero A, Cantagrel JM, Fúster JM, Ibarrola E, Coello J, (1994) Constructive and destructive episodes in the building of young Oceanic Island, La Palma, Canary Islands and genesis of the Caldera de Taburiente. J of Volcanol and Geothe Res, 60, 243-262

Ancochea, E, Brändle JL, Cubas CR, Hernán F, Huertas MJ (1996) Volcanic complexes in the eastern ridge of the Canary Islands: the Miocene activity of the island of Fuerteventura. J of Volcanol and Geothe Res, 70, 183-204

Ancochea E, Brändle JL, Huertas MJ, Cubas CR, Hernán F (2003) The felsic dikes of La Gomera (Canary Islands): Identification of cone sheet and radial dike swarms. J of Volcanol and Geothe Res, 120, 197-206

Ancochea E, Brändle JL, Huertas MJ, Hernán F, Herrera R (2008) Dike-swarms, key to the reconstruction of major volcanic edifices: The basic dikes of La Gomera (Canary Islands). J of Volcanol and Geothe Res, 173, 207-216

Andersen T, Burke EJ, Neumann ER (1995) Nitrogen-rich fluid in the upper mantle: fluid inclusions in spinel dunite from Lanzarote, Canary Islands. Contrib Mineral Petr 120:20–28. http://doi.org/10.1007/BF00311005

Andersen T, Neumann ER (2001) Fluid inclusions in mantle xenoliths. Lithos 55:301–320. http://doi.org/10.1016/S0024-4937(00)00049-9

Anguita F, Hernan F (1975) A propagating fracture model versus a hot spot origin for the Canary Islands. Earth Planet Sci Lett 27:11–19. http://doi.org/10.1016/0012- 821X(75)90155-7

Anguita F, Hernán F (2000) The Canary Islands origin: a unifying model. J Volcanol and Geother Res 103:1–26. http://doi/10.1016/S0377- 0273(00)00195- 5

Aparicio A, Henán F, Cubas CR, Araña V, (2003) Fuentes mantélicas y evolución del volcanismo canario. Estudios Geológicos, 59, 5-13

Araña V, Ortiz R (1991) The Canary Islands: tectonics, magmatism and geodynamic framework. In: Kampunzu AB, Lubala RT J Volcanol and Geother Res 209–249. http://doi/10.1007/978-3-642-73966-8

Becerril L, (2009) Approach to volcanic hazard and its effects in coastal areas of the Canary Islands. Master's thesis, Universidad de Las Palmas de Gran Canaria, Spain.

Becerril L, Cappello A, Galindo I, Neri M, Del Negro C (2013a) Spatial probability distribution of future volcanic eruptions at El Hierro Island (Canary Islands, Spain). J Volcanol and Geother Res 257:21–30. http://doi.org/10.1016/j.jvolgeores.2013.03.005

Becerril L, Galindo I, Gudmundsson A, Morales JM (2013b) Depth of origin of magma in eruptions. Sci Rep 3:1–6. http://doi.org/10.1038/srep02762

Becerril L, Galindo I, Martí J, Gudmundsson A (2015) Three-armed rifts or masked radial pattern of eruptive fissures? The intriguing case of El Hierro volcano (Canary Islands). Tectonophysics 647:33–47. http://doi.org/10.1016/j.tecto.2015.02.006

Belkin HE, De Vivo B (1993) Fluid inclusion studies of ejected nodules from plinian eruptions of Mt. Somma-Vesuvius. J Volcanol and Geother Res 58:89–100. http://doi.org/10.1016/0377-0273(93)90103-X

Bertagnini A, Métrich NN, Francalanci L, Landi P, Tommasini SC (2002) Volcanology and magma geochemistry of the present-day activity: constraints on the feeding system. In: Calvari S, Inguaggiato S, Puglisi G, Ripepe M. (Eds.), Learming from Stromboli: Amer Geophys Union

Bodnar RJ, Binns PR, Hall DL, (1989) Synthetic fluid inclusions-VI. Quantitative evaluation of the decrepitation behaviour of fluid inclusions in quartz at one atmosphere confining pressure. J Metam Geol, 7(2), 229-242

Bodnar RJ (2003) Introduction to aqueous-electrolyte fluid inclusions. Fluid Inclusions: Analysis and Interpretation. Mineral Canada, short course 32:81-100

Bonelli R, Frezzotti ML, Zanon V, Peccerillo A (2004) Evolution of the volcanic plumbing system of Alicudi (Aeolian Islands): Evidence from fluid inclusions in quartz xenoliths. Annals of Geophysic 47:1409–1422

Brey GP, Köhler T (1990) Geothermobarometry in four-phase lherzolites II. New thermobarometers, and practical assessment of existing thermobarometers. J Petrology 31:1353–1378

Burke EAJ, (2001) Raman microspectrometry of fluid inclusions. Lithos 55:139–158.

Burke EAJ, Lustenhouwer WJ, (1987) The application of a multichannel laser Raman microprobe (Microdril-28) to the analysis of fluid inclusions. Chem Geol 61:11–17

Cantagrel JM, Cendrero A, Fuster JM, Ibarrola E, Jamond C (1984) K-Ar chronology of the volcanic eruptions in the Canarian archipelago: island of La Gomera. Bull Volcanol, 47(3), 597-609

Caricchi L, Blundy J (2015) The temporal evolution of chemical and physical properties of magmatic systems. Geol Soc, Lond Special Public 422:1-15

Carracedo JC (1994) The Canary Islands: an example of structural control on the growth of large ocean-island volcanoes. J Volcanol and Geother Res 60:225–241. http://doi.org/10.1016/0377-0273(94)90053-1

Carracedo JC (1999) Growth, structure, instability and collapse of Canarian volcanoes and comparisons with Hawaiian volcanoes. J Volcanol and Geother Res 94:1–19. http://doi.org/10.1016/S0377-0273(99)00095-5

Carracedo JC, Badiola ER, Guillou H, de La Nuez J, Pérez Torrado FJ (2001) Geology and volcanology of La Palma and El Hierro (Canary Islands). Estudios Geol 57:175–273

Carracedo JC, Perez-Torrado FJ, Rodriguez-Gonzalez A, Fernandez-Turiel JL, Klügel A, Troll, VR, Wiesmaier S (2012) The ongoing volcanic eruption of El Hierro, Canary Islands. Eos 93: 89-90. http://doi.org/10.1029/2012EO090002

Carracedo JC, Troll VR (2016) The Geology of the Canary Islands. Elsevier.

Clague DA, Dixon JE (2000) Extrinsic controls on the evolution of Hawaiian ocean island volcanoes. Geochem, Geophys, Geosyst, 1

Collier JS, Henstock TJ, Peirce C, Watts AB, (1998) A detailed geophysical study in the Canary Basin (eastern Atlantic): implications for the internal structure of 130 Ma oceanic crust. Geophys J Int 135:943–963

Colthup NB, Daly LH, (1975) SE Wiberley Infrared and Raman Spectroscopy.

Dasgupta R, Hirschmann MM, Smith ND (2007) Partial melting experiments of peridotite + CO_2 at 3 GPa and genesis of alkalic ocean island basalts. J Petrology 48:2093–2124

De Vivo B, Frezzotti ML, Lima A, Trigila R (1988) Spinel lherzolite nodules from Oahu Island (Hawaii): a fluid inclusion study. Bull Min 111:307–319

Dhamelincourt JM, Beny C, Dubessy J, Poty B, (1979) Analyse d'inclusions fluides à le microsonde MOLE à effet Raman. Bullet de Minéral 102:600–610

Dubessy J, Audeoud D, Wilkins R, Kosztolanyi C (1982) The use of the Raman Micro-probe Mole in the determination of the electrolytes dissolved in the aqueous phase of fluid inclusions. Chem Geol 37:137–150

Dubessy, J., Poty, B., Ramboz, C., 1989. Advances in C–O–H–N–S fluid geochemistry based on micro-Raman spectrometric analysis of fluid inclusions. Europ J Mineral 1:517–534

Ellis DJ, Green DH (1979) An experimental study of the effect of Ca upon garnet-clinopyroxene Fe-Mg exchange equilibria. Contrib Mineral Petrol 71:13-22

Fall A, Tattitch B, Bodnar RJ (2011) Combined microthermometric and Raman spectroscopic technique to determine the salinity of H_2O-CO_2-NaCl fluid inclusions based on clathrate melting. Geochim Cosmochim Ac 75: 951–964. http://doi.org/10.1016/j.gca.2010.11.021

Frezzotti ML, Burke EJ, De vivo B, Stefanini B, Villa IM (1992) Mantle Fluids in Pyroxenite Nodules from Salt Lake Crater (Oahu, Hawaii). Euro J Mineral, *4*;1137–1153

Frezzotti ML, Touret JL, Lustenhouwer WJ, Neumann ER (1994) Melt and fluid inclusions in dunite xenoliths from La Gomera, Canary Islands: tracking the mantle metasomatic fluids. Eur J Mineral, 805-818

Frezzotti ML, Andersen T, Neumann ER, Simonsen SL (2002a) Carbonatite melt–CO_2 fluid inclusions in mantle xenoliths from Tenerife, Canary Islands: a story of trapping, immiscibility and fluid–rock interaction in the upper mantle. Lithos 64:77–96. http://doi.org/10.1016/S0024-4937(02)00178-0

Frezzotti ML, Touret JL, Neumann ER (2002b) Ephemeral carbonate melts in the upper mantle. Europ J Mineral 14:891–904

Frezzotti ML, Peccerillo A (2004a) Fluid inclusion and petrological studies elucidate reconstruction of magma conduits. Eos 85:157–160 http://doi.org/10.1029/2004EO160001

Frezzotti ML, Peccerillo A, Zanon V, Nikogosian I (2004b) Silica-rich melts in quartz xenoliths from Vulcano Island and their bearing on processes of crustal anatexis and crust–magma interaction beneath the Aeolian Arc, Southern Italy. J Petrology 45:3–26

Frezzotti ML, Tecce F, Casagli A (2012) Raman spectroscopy for fluid inclusion analysis. J of Geochem Explor, 112:1–20. http://doi.org/10.1016/j.gexplo.2011.09.009

Frezzotti ML, Touret JL (2014) CO_2, carbonate-rich melts, and brines in the mantle. Geosci Front, 5:697-710

Füster J, Paez A, Sagredo J (1969) Significance of Basic and Ultramafic Rock Inclusions in the Basalts of Canary Islands. Bull Vulcanol 33:665–693

Galindo I, Gudmundsson A (2012) Basaltic feeder dykes in rift zones: geometry, emplacement, and effusion rates. Nat Hazards and Earth Sys Sci, 12(12), 3683

Garrabos Y, Tufeu R, Le Neindre B, Zalczer G, Beysens D (1980) Rayleigh and Raman scattering near the critical point of carbon dioxide. J Chem Physics 72:4637–4651

Gee MJR, Masson DG, Watts AB, Mitchell NC (2001) Offshore continuation of volcanic rift zones, El Hierro, Canary Islands. J Volcanol and Geother Res 105:107–119. http://doi.org/10.1016/S0377- 0273(00)00241-9

Geyer A, Martí J (2010) Tectonophysics The distribution of basaltic volcanism on Tenerife, Canary Islands: Implications on the origin and dynamics of the rift systems. Tectonophysics 483: 310–326. http://doi.org/10.1016/j.tecto.2009.11.002

González PJ, Samsonov SV, Pepe S, Tiampo KF, Tizzani P, Casu F, Sansosti E (2013) Magma storage and migration associated with the 2011 – 2012 El Hierro eruption: Implications for crustal magmatic systems at oceanic island volcanoes, J Geoph Res Solid Earth 118:4361–4377. doi:10.1002/jgrb.50289

Gudmundsson A (2006) How local stresses control magma-chamber ruptures, dyke injections, and eruptions in composite volcanoes. Earth Sci Rev 79:1–31

Guillou H, Carracedo JC, Torrado FP, Badiola ER (1996) K-Ar ages and magnetic stratigraphy of a hotspot-induced, fast grown oceanic island: El Hierro, Canary Islands. J Volcanol and Geother Res 73:141–155. http://doi.org/10.1016/0377-0273(96)00021-2

Gurenko A, Sobolev V, Hoernle KA, Hauff F, Schmincke HU (2009) Enriched, HIMU-type peridotite and depleted recycled pyroxenite in the Canary plume: a mixed- up mantle. Earth Planet Sc Lett 277:514–524

Hansteen TH, Andersen T, Neumann ER, Jelsma H (1991) Fluid and silicate glass inclusions in ultramafic and mafic xenoliths from Hierro, Canary Islands: implications for mantle metasomatism. Contrib Mineral Petrol 107:242–254
Hansteen TH, Klügel A, Schmincke HU (1998) Multi-stage magma ascent beneath the Canary Islands: evidence from fluid inclusions. Contrib Mineral Petrol 132:48–64. http://doi.org/10.1007/s004100050404
Hansteen TH, Klügel A (2008) Fluid inclusion thermobarometry as a tracer for magmatic processes. In: Putirka KD, Tepley FJ Reviews in Mineralogy Min Soc Amer 149:143–177
Heinrich H (1988) Origin and consequences of cyclic ice rafting in the northeast Atlantic Ocean during the past 130,000 years. Quaternary res 29:142-152
Hildner E, Klügel A, Hauff F, (2011) Magma storage and ascent during the 1995 eruption of Fogo, Cape Verde Archipelago. Contrib Mineral Petrol 162:751–772
Hoernle K, Schmincke HU (1992) The Role of Partial Melting in the 15-Ma Geochemical Evolution of Gran Canada: A Blob Model for the Canary Hotspot, *J Petrology 34*, 599–626
Holm PM, Grandvuinet T, Friis J, Wilson JR, Barker AK, Plesner S (2008) An 40Ar-39Ar study of the Cape Verde hot spot: Temporal evolution in a semi-stationary plate environment. Journal of Geophysical Research: Solid Earth 113 http://doi.org/10.1029/2007JB005339
IGME (2010a) Mapa Geológico de España, Escala 1:25.000. Isla de El Hierro. Hoja 1105- II, Valverde, 96 pp.
IGME (2010b) Mapa Geológico de España, Escala 1:25.000. Isla de El Hierro. Hoja 1105- III, Sabinosa, 71 pp.
IGME (2010c) Mapa Geológico de España, Escala 1:25.000. Isla de El Hierro. Hoja 1105- IV, Frontera, 84 pp.
IGME (2010d) Mapa Geológico de España, Escala 1:25.000. Isla de El Hierro. Hoja 1108- I/II, La Restinga, 55 pp.
Kawakami Y, Yamamoto J, Kagi H (2003) Micro-Raman Densimeter for CO_2 Inclusions in Mantle-Derived Minerals. Applied Spectrosc 57:1333–1339
Kendrick MA (2012) High precision Cl, Br and I determinations in mineral standards using the noble gas method. Chemical Geology, 29:116–126
Kendrick MA, Honda M, Pettke T, Scambelluri M, Phillips D, Giuliani A (2013) Subduction zone fluxes of halogens and noble gases in seafloor and forearc serpentinites. Earth and Planet Sci Lett, 365, 86–96
Kendrick MA, Arculus RJ, Danyushevsky LV, Kamenetsky VS, Woodhead JD, Honda M (2014) Subduction-related halogens (Cl, Br and I) and H2O in magmatic glasses from Southwest Pacific Backarc Basins. Earth and Planet Sci Lett, 400:165–176
Klemd R, Van den Kerkhof AM, Horn EE (1992) High-density CO_2-N_2 inclusions in eclogite-facies metasediments of the Münchberg gneiss complex, SE Germany. Contrib Mineral Petrol 111: 409-419
Klügel A, Hoernle, K. A., Schmincke, H. U., & White, J. D. (2000). The chemically zoned 1949 eruption on La Palma (Canary Islands): Petrologic evolution and magma supply dynamics of a rift zone eruption. J Geophys Res: Solid Earth 105:5997-6016
Klügel A, Hansteen TH, Galipp K (2005) Magma storage and underplating beneath Cumbre ieja volcano, La Palma (Canary Islands). Earth Planet Sci Lett 236:211–226 http://doi.org/10.1016/j.epsl.2005.04.006
Klügel A, Longpré MA, García-Cañada L, Stix J, (2015) Deep intrusions, lateral magma transport and related uplift at ocean island volcanoes. Earth Planet Sci Lett 43:140–149 http://doi.org/10.1016/j.epsl.2015.09.031
Longpré MA, Klügel A, Diehl A, Stix J (2014) Mixing in mantle magma reservoirs prior to and during the 2011 – 2012 eruption at El Hierro, Canary Islands. Geology, 42:315–318 http://doi.org/10.1130/G35165.1
López, C., Blanco, M. J., Abella, R., Brenes, B., Cabrera Rodríguez, V. M., Casas, B., & García, O.

(2012). Monitoring the volcanic unrest of El Hierro (Canary Islands) before the onset of the 2011–2012 submarine eruption. Geophys Res Lett, 39
Marinoni LB, Gudmundsson A (2000) Dykes, faults and palaeostresses in the Teno and Anaga massifs of Tenerife (Canary Islands). J Volcanol and Geother Res 103:83–103 http://doi.org/10.1016/S0377- 0273(00)00217-1
Martí J, Pinel V, Lõpez C, Geyer A, Abella R, Tárraga M, Rodríguez C (2013a) Causes and mechanisms of the 2011-2012 El Hierro (Canary Islands) submarine eruption. J Geophy Res Solid Earth, 118:823–839. http://doi.org/10.1002/jgrb.50087
Martí J, Castro A, Rodríguez C, Costa F, Carrasquilla S, Pedreira R, Bolos X (2013b) Correlation of magma evolution and geophysical monitoring during the 2011-2012 El Hierro (Canary Islands) submarine eruption. J Petrology, 54:1349–1373 http://doi.org/10.1093/petrology/egt014
Martinez-Arevalo C, de Lis Mancilla F, Helffrich G, Garcia A (2013). Seismic evidence of a regional sublithospheric low velocity layer beneath the Canary Islands. Tectonophysics, 608, 586-599
Martinez-Arevalo C, Mancilla FD, Helffrich G, Garcia A (2013) Seismic evidence of a regional sublithospheric low velocity layer beneath the Canary Islands. Tectonophysics 608:586–599. http://doi.org/10.1016/j.tecto.2013.08.021
Masson DG (1996) Catastrophic collapse of the volcanic island of Hierro 15 ka ago and the history of landslides in the Canary Islands. Geology, 24:3, 231-234
Masson DG, Watts B, Gee MJR, Urgeles R, Mitchell NC, Le Bas TP, Canals M. (2002) Slope failures on the flanks of the western Canary Islands. Earth Sci Rev 57:1–35
Masson DG, Harbitz CB, Wynn RB, Pedersen G, Løvholt F (2006) Submarine landslides: processes, triggers and hazard prediction. Philosophical Transactions. Series A, Math, Physical Eng Sci 364:2009–2039
Morgan, D. J., Jerram, D. a., Chertkoff, D. G., Davidson, J. P., Pearson, D. G., Kronz, a., & Nowell, G. M. (2007). Combining CSD and isotopic microanalysis: Magma supply and mixing processes at Stromboli Volcano, Aeolian Islands, Italy. Earth Planet Sc Lett 260:419–431 http://doi.org/10.1016/j.epsl.2007.05.037
Münn, S., Walter, T. R., & Klügel, A. (2006). Gravitational spreading controls rift zones and flank instability on El Hierro, Canary Islands. Geol Mag 143: 257-268
Nakamura K, (1977) Volcanoes as possible indicators of tectonic stress orientation—principle and proposal. J Volcanol and Geoth Res 2:1-16
Neumann E (1991) Ultramafic and mafic xenoliths from Hierro, Canary Islands: evidence for melt infiltration in the upper mantle. J Chem 53:1689–1699 http://doi.org/10.1017/CBO9781107415324.004
Neumann ER, Wulff-Pedersen E, Johnsen K, Andersen T, Krogh E (1995) Petrogenesis of spinel harzburgite and dunite suite xenoliths from Lanzarote, eastern Canary Islands: Implications for the upper mantle. Lithos 35:83–107. http://doi.org/10.1016/0024-4937(95)91153-Z
Neumann ER, Wulff-Pedersen E, Pearson NJ, Spencer EA (2002) Mantle Xenoliths from Tenerife (Canary Islands): Evidence for Reactions between Mantle Peridotites and Silicic Carbonatite Melts inducing Ca Metasomatism. J Petrology 43:825–857 http://doi.org/10.1093/petrology/43.5.825
Neumann ER, Griffin WL, Pearson NJ, O'Reilly SY (2004) The evolution of the upper mantle beneath the Canary Islands: Information from trace elements and Sr isotope ratios in minerals in mantle xenoliths. J Petrology 45: 2573–2612. http://doi.org/10.1093/petrology/egh063
Pasteris JD, Kuehn CA, Bodnar RJ, 1986 Applications of the laser Raman microprobe RAMANOR U-1000 to hydrothermal ore deposits: Carlin as an example. Econ Geol 81: 915–930
Pasteris JD, Wopenka B, Seitz JC, 1988. Practical aspects of quantitative laser Raman microprobe spectroscopy for the study of fluid inclusions. Geochim Cosmochim Ac 52: 979–988

Peccerillo A, Frezzotti ML, De Astis G, Ventura G (2006) Modeling the magma plumbing system of Vulcano (Aeolian Islands, Italy) by integrated fluid-inclusion geobarometry, petrology, and geophysics. Geology 34:17. http://doi.org/10.0030/G22117.1

Raman CV (1928) A new radiation. Indian J Physics 387

Roedder E (1965) Liquid CO_2 inclusions in olivine-bearing nodules and phenocrysts from basalts. Am Miner 50:20–40

Roedder E (1983) Geobarometry of ultramafic xenoliths from Loihi Seamount, Hawaii, on the basis of CO_2 inclusions in olivine. Earth and Planet Sci Lett, 66, 369-379

Roedder E (1984) Geothermobarometry of ultramafic xenoliths from Loihi seamount, Hawaii, on the basis of CO_2 inclusions in olivine. Earth Planet Sci Lett 66:369-379

Rosasco, G.J., Roedder, E., Simmons, J.H., 1975. Laser-excited Raman spectroscopy for nondestructive partial analysis of individual phases in fluid inclusions in minerals.

Ryan MP (1988) Structure of Active Magmatic Systems' Kilauea Volcano, Hawaii. Journal of Geophysical Research, 93: 4213–4248. http://doi.org/10.1029/JB093iB05p04213

Scandone R, Cashman KV, Malone SD (2007) Magma supply, magma ascent and the style of volcanic eruptions. Earth Planet Sci Lett 253:513–529 http://doi.org/10.1016/j.epsl.2006.11.016

Schmincke HU (1982) Volcanic and chemical evolution of the Canary Islands. Geol African cont marg pp. 273–306

Schwarz S, Klügel A, Wohlgemuth-Ueberwasser C (2004) Melt extraction pathways and stagnation depths beneath the Madeira and Desertas rift zones (NE Atlantic) inferred from barometric studies. Contrib Mineral Petrol 147:228–240. http://doi.org/10.1007/s00410-004-0556-4

Seitz, J.C., Pasteris, J.D., Wopenka, B., 1987. Characterization of CO_2-CH_4-H_2O fluid inclusions by microthermometry and laser Raman microprobe spectroscopy: inferences for clathrate and fluid equilibria. Geochim Cosmochim Ac 51:1651–1664

Shaw HR (1980) The fracture mechanisms of magma transport from the mantle to the surface. Physics of magmatic processes 64:201-264

Stroncik NA, Klügel A, Hansteen TH (2009) The magmatic plumbing system beneath El Hierro (Canary Islands): constraints from phenocrysts and naturally quenched basaltic glasses in submarine rocks. Contrib Mineral Petrol 157: 593–607. http://doi.org/10.1007/s00410-008-0354-5

Touret JL (2001) Fluids in metamorphic rocks. Lithos 55:1-25

Troll VR, Klügel A, Longpré MA, Burchardt S, Deegan FM, Carracedo JC, Hansteen TH (2012) Floating stones off El Hierro, Canary Islands: xenoliths of pre-island sedimentary origin in the early products of the October 2011 eruption. Solid Earth, 3(1), 97

Uchupi, E., Emery, K. O., Bowin, C. O., & Phillips, J. D (1976). Continental margin off western Africa: Senegal to Portugal. AAPG Bulletin, 60(5), 809-878

Vaggelli G, Francalanci L, Ruggieri G, Testi S (2003) Persistent polybaric rests of calcalkaline magmas at Stromboli volcano, Italy: pressure data from fluid inclusions in restitic quartzite nodules. Bull Volcanol 65:385–404. doi:10.1007/s00445-002-0264-8

van den Bogaard, P (2013). The origin of the Canary Island Seamount Province-New ages of old seamounts. Sci rep 3

Van den Kerkhof AM (1988a) The system CO_2 –CH_4 –N_2 in fluid inclusions: theoretical modelling and geological applications. PhD Dissertation, Amsterdam Free University, 206 pp

van den Kerkhof AM (1988b) The system CO_2–CH_4–N_2 in fluid inclusions: theoretical modeling and geological applications. Ph.D. Thesis, Vrije Universiteit Amsterdam, The Netherlands. 206

van den Kerkhof AM, Olsen SN, (1990) A natural example of superdense CO_2 inclusions: microthermometry and Raman analysis. Geochim Cosmochim Ac 55: 2533–2544

Vityk MO, Bodnar R J (1998) Statistical microthermometry of synthetic fluid inclusions in quartz during decompression reequilibration. Contrib Mineral Petrol 132:149-162

Wang X, Chou IM, Hu W, Burruss RC, Sun Q, Song Y (2011) Raman spectroscopic measurements of CO_2 density: Experimental calibration with high-pressure optical cell (HPOC) and fused silica capillary capsule (FSCC) with application to fluid inclusion observations. Geochim Cosmochim Ac 75:4080–4093. http://doi.org/10.1016/j.gca.2011.04.028

Wells PR (1977) Pyroxene thermometry in simple and complex systems. Contrib Mineral Petrol 62:129-139

Widom E, Hoernle K, Shirey SB, Schmincke HU (1999) Os Isotope Systematics in the Canary Islands and Madeira: Lithospheric Contamination and Mantle Plume Signatures. J Petrology, 40(2), 279–296

Witt-Eickschen G, Seck HA (1991) Solubility of Ca and Al in orthopyroxene from spinel peridotite: an improved version of an empirical geothermometer. Contrib Mineral Petrol 106:431-439

Yamamoto J, Kagi H (2006) Extended Micro-Raman Densimeter for CO_2 Applicable to Mantle-originated Fluid Inclusions. Chemistry Lett 35:610–611. http://doi.org/10.1246/cl.2006.610

Zanon V (2003). Magmatic feeding system and crustal magma accumulation beneath Vulcano Island (Italy): Evidence from CO_2 fluid inclusions in quartz xenoliths. J Geophy Res 108:2298. http://doi.org/10.1029/2002JB002140

Zanon V, Nikogosian I (2004) Evidence of crustal melting events below the island of Salina (Aeolian arc, southern Italy). Geol Mag 141:525–540 http://doi.org/10.1017/S0016756804009124

Zanon V, Frezzotti ML (2013) Magma storage and ascent conditions beneath Pico and Faial islands (Azores archipelago): A study on fluid inclusions. Geochem, Geophys, Geosyst 14:3494–3514. http://doi.org/10.1002/ggge.20221

Zanon V (2015) Conditions for mafic magma storage beneath fissure zones at oceanic islands. The case of São Miguel island (Azores archipelago). Geol Soc, Lond Special Public 422: 85–104

5. MANUSCRIPT 1: *submitted to Chemical Geology on 8th December 2016*

Halogens in the lithospheric mantle beneath El Hierro (Canary Islands)

I.M. Villa[1,2], V. Peverelli[1], E. Oglialoro[1], M.L. Frezzotti[1]

1 - Dipartimento di Scienze dell'Ambiente e della Terra, Università di Milano Bicocca, 20126 Milano, Italy
2 - Institut für Geologie, Universität Bern, 3012 Bern, Switzerland

Corresponding author: igor.villa@geo.unibe.ch

Abstract

Halogens are an underexplored geochemical marker. We derive absolute halogen amounts from rare gas amounts in irradiated samples. Kr-Xe systematics also yield Ba and U concentrations. We combined irradiation with stepheating on carbonate-sulfate-rich fluid inclusions (FI)-bearing xenoliths from El Hierro, Canary Island: spinel harzburgite XML-7 and spinel dunite XML-1. Daughter minerals in multiphase FI identified by Raman microspectroscopy include dolomite, sulfohalite and anhydrite.

Three components are recognised in the rare gas release. (1) Atmospheric surface contamination decreases up to 1000 °C. (2) U-derived ^{134,136}Xe and ^{85,86}Kr are released in a spike at 1000 °C, decoupled from FI. This requires a different carrier than FI, e.g. Ti oxides. U concentrations are 0.3- 0.4 μg/g. (3) FI decrepitation by laboratory heating occurs above 1200 °C, corresponding to the release of ^{80,82}Kr and ^{128}Xe in the 1200 and 1400 °C steps. Br whole-rock concentrations are 5-8 ng/g; the molar Br/Cl and I/Cl ratios in the harzburgite FI, 4×10^{-4} resp. 3×10^{-4}, are similar to those in the dunite FI, 1×10^{-4} resp. 2×10^{-4}. Halogen-derived rare gases are released together with artificial ^{131}Xe from Ba; Ba has a high affinity for CO_2-rich fluids. The calculated Ba concentrations are 4-6 μg/g, with Ba/Br ≈ 750. The Br/Cl and I/Cl ratios are well distinct from MORB and "typical mantle": Br/Cl is lower by one order of magnitude, I/Cl is > 30 times higher. Serpentinisation would (i) be visible petrographically, (ii) give positively correlated Br/Cl vs I/Cl. The process leading to the observed halogen pattern instead requires at least two stages separated in time and in *P-T* and probably involves remnants of older continental crust incorporated in the lithospheric mantle.

1. Introduction

Halogens are highly incompatible volatile elements with very large ionic radius. Because of the variability in incompatibility among them and their contrasting behaviour, they serve as key tracers of volatile fluxes in the mantle (e.g., Wyllie, 1989; Webster, 1990; 1992; Bureau and Keppler, 1999). Chlorine is notably considered to trace water thanks to its high H_2O-silicate melt partition coefficient, while Br/Cl and I/Cl ratios provide variable halogen signatures for different geological settings (e.g., Böhlke and Irwin, 1992; Kendrick *et al.,* 2013).

In lithospheric mantle, halogens have been extensively studied in subduction zones, where peridotites contain brine fluid inclusions (salinity up to 50 wt. % in NaCl eq.; e.g., Scambelluri *et al.,* 1997; McInnes *et al.,* 2001; Kawamoto *et al.,* 2013). Most Cl is considered to be recycled via arc magmatism after being released into the mantle wedge, and only a very small portion is subducted into the deep mantle (Straub and Layne, 2003).

Halogen concentrations in mantle fluids from intraplate and extensional settings have been reported less often. For several decades CO_2 was considered the exclusive fluid phase (e.g., Roedder, 1965; Andersen and Neumann, 2001). Direct evidence of brines in mantle xenoliths from extensional lithospheric settings came from the Ethiopian plateau where CO_2-brine fluid inclusions are preserved in spinel lherzolites (Frezzotti *et al.,* 2010). These authors calculated $X_{H_2O} = 0.33$, $X_{NaCl} = 0.02$, a minimum NaCl-equivalent salinity (NCES) of 14-10 wt. % (Cl = 4-5 mol. %), and a trapping pressure of 1.4 -1.5 GPa at 950°C.

Earlier work had inferred high halogen concentrations in several extensional and intraplate locations (Hawaii, Australia, Canary Islands) on the basis of indirect evidence (e.g., presence of Cl-rich amphibole and/or phlogopite: Andersen *et al.,*1984; De Vivo *et al.,* 1988; Frezzotti and Peccerillo, 2007; Frezzotti *et al.,* 2002). Halogens are also important components of diamond forming fluids in the deep subcontinental lithospheric mantle. A study of nanometric to micrometric fluid inclusions in diamonds (e.g., Klein-Ben David *et al.,* 2007; and references therein) suggests that the trapped fluids can be explained by mixing of three end-members: hydrous-silicic fluids rich

in Si, Al and K; carbonatitic fluids rich in carbonates, Ca, Fe and Mg, with variable contents of Na and K; and aqueous brines with high concentrations of Cl (up to 30-40 wt. %), K and Na.

The first evidence of aqueous-chloride-carbonate fluids in diamonds came from South African diamonds (Izraeli *et al.,* 2001) and it has been reported worldwide since (Klein-BenDavid *et al.,* 2007; Smith *et al.,* 2012); as a consequence, it was proposed that there may exist halogen reservoirs in the mantle (Frezzotti and Ferrando, 2016; and references therein). Chemical fractionation in halogen ratios (e.g., Br/Cl and I/Cl) data suggest that recycled halogens represent an important component in diamond fluids, but the amounts derived directly from subducted lithosphere, vs. the amounts recycled in the deep convecting mantle are disputed (cf., Burgess *et al.,* 2002).

Currently there exist very few data on the concentrations and fractionation of halogens in mantle peridotites, and in their fate during fluid-rock interactions. In this respect, the Canary Islands represent a promising setting to investigate the presence of halogens in the lithosphere in intraplate settings associated with plume magmatism. Halogens have been previously reported in fluid inclusions in spinel lherzolite from Tenerife (Canary Islands). Three types of fluid inclusions were detected: pure CO_2 (Type A), carbonate-rich CO_2-SO_2 mixtures (Type B) and polyphase inclusions dominated by silicate glass (Type C) (Frezzotti *et al.,* 2002). Raman microspectroscopy revealed the presence of talc and serpentine and, among the minerals coating the walls of Type A fluid inclusions, NaCl and KCl were identified by SEM. The presence of talc or serpentine and alkali-chlorides coating the cavity walls suggests an original halogen-rich aqueous-rich fluid, and the presence of a former brine.

The present work focuses on the measurement of abundances and ratios of halogens in fluid inclusions present in mantle xenoliths from El Hierro (western Canary Islands). This island was chosen because it is an active volcano in its shield-building phase.

2. Geological and petrological setting

The Canary Island volcanoes lie on oceanic lithosphere aged between *ca*. 180 Ma in the east and *ca.* 150 Ma in the west (Abu El-Rus *et al.,* 2006; and references therein). In fact, the crustal ages beneath the archipelago are based on the location of the M25 magnetic anomaly (156 Ma) between the islands of El Hierro and La Palma and on the location of the S1 anomaly (≈175 Ma) between the easternmost islands and Africa (Widom *et al.,* 1999; and references therein). El Hierro is the smallest and westernmost island of the archipelago (Fig. 1).

The oldest subaerial rocks are related to El Tiñor edifice, active from 1.12 ± 0.2 Ma until 882 ± 13 ka; the youngest products are those pertaining to the current Rift Volcanism (El Golfo edifice), constantly active since 545 ka BP (Carracedo *et al.,* 2001; Guillou *et al.,* 1996). The most recent volcanic eruption occurred in AD 2011 off the N-S rift (Carracedo *et al.,* 2011).

There is no monotonic temporal progression in the time evolution of magmatism of the islands or of the many seamounts. This has triggered an extensive controversy regarding the origin and the petrogenesis of the island chain (Neumann *et al.,* 1995; Van Den Bogaard, 2013; and references therein). The proposed hypotheses can be grouped into thermal and tectonic models (Martinez-Arevalo *et al.,* 2013 and references therein). The most commonly accepted model is the thermal mantle plume, although several inconsistencies raise questions. Among these, the comparatively low magma production relative to other oceanic island volcanoes (e.g., Hawaii), and the absence of a monotonic chronological progression (Van Den Bogaard, 2013).

Rocks constituting the lithosphere beneath the Canary Islands show complex and variable chemical composition, and are mostly dominated by spinel harzburgites and dunites, with subordinate lherzolites (Fig. 2; Neumann *et al.,* 1995; Neumann *et al.,* 2002; 2004; Wulff-Pedersen *et al.,* 1996). Neumann *et al.* (2004) suggested that the original composition of the lithosphere before metasomatism was that of a Primordial Mantle that suffered 25-30 % depletion by partial melting processes. Metasomatic enrichment in peridotites, following melting events, has been reported by several authors (e.g. Abu El-Rus *et al.,* 2006; Neumann *et al.,* 2002; Frezzotti *et al.,*

1994; 2002; Day *et al.,* 2010). In particular, metasomatism with addition of CaO (i.e., silicate-carbonate metasomatic melts) is documented by Neumann *et al.* (2004) and Abu El-Rus *et al.* (2006), who also suggest that analysed lherzolites derived from reactions between metasomatic melts with harzburgite wall-rocks which lead to the formation of olivine + clinopyroxene + Si-rich melt at the expense of orthopyroxene. Clinopyroxene in dunites would also be due to wall-rocks/metasomatic melts reactions (Abu El-Rus *et al.,* 2006; Neumann *et al.,* 1995; 2004). Neumann *et al.* (2004) further suggested that the mantle under the Canary Islands was metasomatised to different extents and with different styles in each island: the strongest degree of metasomatism is reported in xenoliths from Tenerife, where cryptic, modal and Ca-metasomatism occurred, while the lowest is documented in Lanzarote (Neumann *et al.,* 2004).

As for metasomatic agents, the most consistent model for mantle xenoliths from Tenerife was proposed by Frezzotti *et al.* (2002). A volatile-rich, siliceous, alkaline carbonatite melt infiltrated the mantle and, before or after trapping inside fluid inclusions, separated into a mixed CO_2-H_2O-NaCl fluid and a silicate or silico-carbonatite melt. The interstitial melt reacted with wall-rock minerals –primarily orthopyroxene – and unmixed into immiscible carbonaceous silicate melt and CO_2-, H_2O-, and halogen-rich fluid (Frezzotti *et al.,* 2002).

The El Hierro peridotitic xenoliths consist of dominant spinel harzburgite with minor lherzolites and dunites showing a clear depletion by variable degrees of partial melting (Neumann *et al.,* 1991; Hansteen *et al.,* 1991; 1998). Based on fluid inclusion and petrological studies, these authors suggested that the lithosphere beneath El Hierro suffered a complex metasomatic history of crystallisation, heating and cooling due to infiltration of silicate melts and CO_2-rich fluids and melts.

3. Analytical techniques

Cl, Br and I are analyzed by irradiating samples with neutrons and measuring artificial noble gas isotope anomalies in a noble gas mass spectrometer (Jeffery and Reynolds, 1961). Neutron activation produces radioactive halogen isotopes ^{38}Cl, ^{80}Br, ^{82}Br and ^{128}I, whose stable β-decay products are $^{38}Ar_{Cl}$, $^{80,82}Kr_{Br}$ and $^{128}Xe_{I}$. This method offers high sensitivity and precision (Böhlke and Irwin, 1992); it can also provide ^{39}Ar-^{40}Ar ages if the K concentration is sufficient and if the initial $^{40}Ar/^{36}Ar$ ratio can be constrained. Irradiation also produces ^{131}Xe from Ba and several Kr and Xe isotopes from U (Ozima and Podosek, 2002).

Before irradiation, chips of rocks were ultrasonically washed in distilled water and acetone, wrapped in high purity Al-foil and sent to the McMaster University Research Reactor (Hamilton, Canada). Thermal and epithermal neutrons with resonant energies (1 eV – 10 keV) produce the halogen-derived noble gas isotopes; therefore, the irradiation canister must not be Cd-shielded. Long irradiations provide the best detection limits but, to prevent excessive irradiation damage, the fluence of fast neutrons (> 0.1 MeV) is kept below $\approx 5\times10^{18}$ n·cm^{-2} (Kendrick, 2012; and references therein).

To convert the concentrations of artificial noble gases to target element concentrations (in the present case Cl, Br, Ba, I and U), it is necessary to resort to a concentration monitor with independently known composition. As a concentration monitor we used scapolite SY (Kendrick, 2012) with its revised element concentrations (Kendrick *et al.,* 2013a), namely: $X(Cl) = 35.4 \pm 1.6$ mg/g; $X(Br) = 710 \pm 50$ µg/g; $X(I) = 890 \pm 110$ ng/g; $X(K) = 1.16 \pm 0.08$ mg/g.

Noble gas isotope measurements were made at Università di Milano Bicocca on a NuInstruments™ Noblesse™ mass spectrometer, equipped with one Faraday cup and one Mascom™ ion counter. The two rock chips and the scapolite were degassed by stepwise heating in a double-vacuum Ta resistance furnace, followed by purification by two SAES™ C-50 getters.

For sample XML1 and the SY scapolite monitor, the same heating schedule in six 200 °C intervals was followed. For sample XML7, the 1200 and 1400 °C steps were extracted as one step.

Knowing approximately at what temperature decrepitation of fluid inclusions is expected is extremely valuable for data interpretation. Roedder (1965) reported decrepitation experiments on several dunitic nodules from a Hawaiian sample. After heating grains smaller than 1 mm at 1000 °C for a day, only the largest fluid inclusions were lost by decrepitation; at 1200 °C for 30 min the smaller inclusions were still intact and showed no signs of leakage. Complete decrepitation was not achieved even after heating for 20 min at 1300 °C. Finally, Roedder (1965) argued that decrepitation had to be complete at 1500 °C because the sample melted.

Analysis of fluid inclusions by Raman microspectrometry was made at Università di Torino on a Horiba HR Labram spectrometer. The spectrometer has a Peltier-cooled CCD detector and an Argon-ion (532 nm) laser set to an emission power of 80 mW. Confocal optics with an Olympus100× lens focused the laser to analyse a volume of about $1\times1\times3\mu m^3$. Scattered light was analysed with a 100 μm slit and a spectral resolution of 1.5 cm^{-1}, using a 1800 grooves/mm grating. Collection times varied between 5 and 30s, with 1 to 3 accumulations depending on fluorescence and signal intensity. Mineral phase identification was based on our spectral database (Frezzotti *et al.,* 2012).

4. Results

4.1. Petrography

Mantle xenoliths for halogen analysis were selected among some thirty peridotite xenoliths collected at El Julan Valley, a xenolith locality not studied before. The host basaltic lava flow is related to Rift Volcanic activity. In this flow, xenoliths are ubiquitous and mostly unaltered: they measure up to 10 cm and consist of coarse-grained (mm- to cm-sized) olivine and pyroxenes, and finer-grained (≤1 mm) spinel.

A spinel harzburgite (XML7) and a spinel dunite (XML1) were analysed by optical microscopy. Both samples are very coarse grained, and show primary protogranular textures (i.e., recrystallization degrees, ranging from 3 to 20 %; Figs. 4, 5). Two generations of olivine are

186 observed.

187 Olivine porphyroclasts (Ol I) range between 600 μm to 1 cm in size, are mainly subhedral and
188 can present wavy extinction. Olivine porphyroclasts contain many fluid inclusions. Notably, sample
189 XML7 contains carbonate veins associated with silicate glass along grain boundaries. Olivine
190 neoblasts (Ol II) are up to 2 mm in size, and form frequent triple junctions (Fig. 3).

191 Orthopyroxene porphyroclasts are coarse grained (0.4 – 3 mm), and show clinopyroxene
192 exsolution lamellae. Clinopyroxene (0.3 – 1.5 mm) and spinel (0.2 – 2 mm) are mostly anhedral.
193 Two spinel generations are observed in sample XML1: an interstitial one, never included in other
194 phases, and a vermicular one associated with olivine neoblasts (Fig. 4). Fluid and melt inclusions
195 occur in either intragranular or intergranular trails in olivine porphyroclasts, and subordinately in
196 orthopyroxene porphyroclasts. Three main fluid/melt inclusion populations have been characterised
197 by petrography and Raman spectroscopy (Oglialoro *et al.,* submitted):

198 Type I – Early carbonate + silicate glass inclusions and intragranular microveins (ca. 5 μm
199 thick) containing highly birefringent minerals (Figs. 4-5). The same association is also locally
200 present as dendritic inclusion associations from original microveins in porphyroclasts of olivine
201 (Fig. 5). These inclusions are dominant in sample XML7.

202 Type II – Early salt-carbonate-rich CO_2-N_2 fluid inclusions. Inclusions consist of 1-50 μm-
203 sized aggregates of several highly birefringent solid phases (prevalently carbonates, or carbonates +
204 sulphates), one opaque mineral, ± CO_2+N_2.

205 Type III – Late CO_2 fluid inclusions, 2-20 μm in size, were trapped at later stages, mostly
206 along intergranular trails between olivine and orthopyroxene crystals (Fig.6).

207 Fluid composition in Type I inclusions corresponds to a complex CO_2-rich ± N_2 hydrous salt
208 melt, or a C-O-H-N-salt metasomatic fluid, rich in sulphur, Ca, P, alkalis, and probably chlorides.
209 The Raman spectra of the daughter minerals in Fig.7 illustrate the complex chemical composition
210 of fluids. Spectrum 1 shows the presence of anhydrite (peaks at 613, 630, 679, 1019 and 1131 cm^{-1}),
211 sulfohalite (peak at 1004 cm^{-1}) and dolomite (peaks at 1100 and 724 cm^{-1}). Spectrum 2 reveals the

212 additional presence of apatite (peaks at 590, 630 and 963 cm^{-1}) and CO_2, and Spectrum 3 documents
213 the presence of spinel (peak at 687 cm^{-1}). The former presence of water is indicated by a hydrous
214 Mg-sulfate $MgSO_4 \cdot nH_2O$ (peaks at 615, 642, 990, 3305 and 3402 cm^{-1}) in the inclusions (spectrum
215 4 in Fig.8). Unfortunately, Raman microspectroscopy does not allow the detection of chlorides. The
216 distribution and (qualitative) relative abundances of daughter mineral phases within a single
217 inclusion are illustrated in the Raman map in Fig.9.
218 Raman- and microthermometry-based CO_2+N_2 density calculations for Type II inclusions in
219 other xenoliths from the same locality defined a maximum density of 1.19 g/cm^3 (Oglialoro *et al.,*
220 submitted) that corresponds to P = 1.8 GPa, i.e. a depth of about 60 km.

221 ## 4.2. Cl, Br, I, Ba, U concentrations

222 The measured amounts of artificial noble gas isotopes are shown in Table 1 after subtraction
223 of atmospheric contamination (both from the furnace and adsorbed on the sample). Ba, I, Br and Cl
224 element ratios are also shown; their concentrations are only calculated relative to whole rocks, as
225 the mass fraction of fluid inclusions in the whole rocks was not determined on the analysed
226 samples.
227 The stepwise heating data require four isotopically distinct rare gas reservoirs. (i)
228 Atmospheric contamination is detected up to 1000 °C. (ii) Artificial rare gas isotopes from matrix
229 minerals are degassed at 1000 °C, when the decrepitation of fluid inclusions has not yet started
230 (Fig.10). (iii) The release of $^{80,82}Kr$ and ^{128}Xe occurs above 1200 °C, the temperature at which
231 Roedder (1965) observed the onset of fluid inclusion decrepitation. (iv) An unanticipated
232 observation was that halogen-derived noble gases are closely associated with $^{131}Xe_{Ba}$: its presence
233 in the fluid inclusions is in accordance with the fact the Ba is highly mobile in CO_2 fluids.
234 Fig.10 shows the differential degassing of halogen-derived rare gases. Surface contamination
235 consists both of atmospheric rare gases and of halogen-derived Kr_{Br} and Xe_I. The halogen release
236 below 800 - 1000 °C could be contamination of the sample surface (marine aerosol, anthropogenic)

or presence of traces of easily degassed halogen-rich secondary minerals. It is unlikely to be a primary signature, as the halogen element ratios vary in a much narrower interval in the heating steps corresponding to fluid inclusion decrepitation (the $^{38}Ar_{Cl}/^{80}Kr_{Br}$ and $^{128}Xe_{I}/^{80}Kr_{Br}$ ratios range between 15 and 34, and 0.3 and 3 in the 1200 and 1400 °C steps, whereas in the low temperature steps they reach 490 and 4).

The ^{235}U-derived ^{134,136}Xe and ^{85,86}Kr are released mainly in the 1000 °C step. The carrier phase of U was not identified. In principle, all of the U could reside in the fluid inclusions, as U is a mobile element in CO_2-rich fluids, and indeed a minor part of the uranogenic isotopes $^{134}Xe_U$, $^{136}Xe_U$, $^{85}Kr_U$ and $^{86}Kr_U$ is hosted in fluid inclusions. If this were the case, the predominant release of these four isotopes in the 1000 °C step would require that they were produced in the fluid inclusions but were entirely recoiled out of them and implanted into the surrounding olivine, from which they would have been released earlier than the FI decrepitation temperature. However, olivine is quite impervious to noble gases below 1200 °C, and the hypothesis is unlikely. Moreover, the fission recoil length in minerals is < 0.1 μm, which corresponds to < 0.5 μm in the less dense FI fluid. In a fluid inclusion larger than 2 μm most of the U-derived Kr and Xe would therefore remain in the fluid. Apatite would be a more attractive possibility, as it can host U concentrations > 1 mg/g; the release of uranogenic Kr and Xe is also accompanied by a slight enhancement of the Cl and Br release. Considering the low U concentration of the whole rock (< 1 μg/g), the total U budget is accounted for by an apatite mass fraction around 10^{-4}, undetected by petrographical observations.

The isotopic composition of the Xe produced from U are similar to those reported by Kendrick *et al.* (2015). The $^{136}Xe/^{134}Xe$ ratio > 1 suggests a component deriving from ^{238}U, that is, retention of radiogenic Xe. The Kr measurements are not sufficiently precise to prove or disprove it. However, analysis of an unirradiated sample detected no enrichment of the $^{136}Xe/^{129}Xe$ ratio. It is possible that uranogenic Xe produced in the core of the McMaster reactor (thermal, epithermal and fast neutrons) has a different isotopic composition from that in textbooks.

5. Discussion

Data collected from petrography, Raman microspectroscopy and mass spectroscopy allow us to better delineate geochemical and petrological characteristics of the lithospheric mantle beneath El Hierro in the frame of existing models for the genesis of volcanism.

Fluid inclusion compositions indicate that complex CO_2-hydrous salt melts or C-O-H-salt metasomatic fluids, rich in CO_2, sulfur, water, Ca, P, alkalis, represent the metasomatic agent in the lithospheric mantle beneath El Hierro. These metasomatic fluids at El Hierro are chemically similar to mantle fluids present at Tenerife which consist of dominant carbonate-rich CO_2–SO_2-H_2O-chloride mixtures: Frezzotti *et al.* (2012) also suggested a volatile-bearing, siliceous, carbonatite melt and Cl-rich fluids (trapped in the fluid inclusions) as the dominant metasomatic agent. Since the fluid inclusions are only present in olivine and orthopyroxene porphyroclasts and absent in neoblasts, they bear witness that metasomatism occurred at an early stage, predating magmatic activity. The halogen ratios in fluid inclusions of mantle xenoliths from El Hierro are shown in Fig.11. The present data plot away from intraplate and MORB mantle sources. The fluids contained in the fluid inclusions of our samples also plot far from the seawater signature: the Br/Cl ratio is lower by ca. 30%, whereas the I/Cl ratio is about 2 orders of magnitude higher. Low-temperature serpentinisation operates in the opposite direction (increasing the Br/Cl ratio and decreasing the Br/I ratio). Interaction with pore fluids in ocean-floor sediments does increase the I/Cl ratio, but the Br/Cl ratio as well; moreover, it is not expected to be significant at 60 km depth. This rules out any secondary low-temperature alteration. The observed halogen patterns are a primary reflection of the metasomatic mantle fluids present at depths greater than 50 km.

Molar I/Cl ratios of *ca*. 2×10^{-4} (corresponding to $6\text{-}7\times10^{-4}$ by weight) in mantle fluids from the lithosphere beneath El Hierro are over one order of magnitude higher than in typical MORB mantle (Fig.11). This requires either an I-rich source or a process capable of enriching I relative to Cl. If one views element ratios as controlled by physical reservoirs, then the iodine enrichment of subduction setting rocks and fluids is to be attributed to a sediment component (You *et al.,* 1994), in

288 a subduction-zone geodynamic settings. A process-oriented view considers the high I/Cl ratio found
289 at convergent margins as a fractionation due to petrologic causes, such as breakdown of serpentine
290 minerals and associated fluid release (Kendrick *et al.,* 2013b; 2014).

291 Pagé *et al.* (2016) highlight the role of the halogen carrier phases. In their study of the
292 Tavşanlıblueschists, it can be noted that the blueschist rocks lie on the trend defined by the ocean-
293 floor porewaters (Pagé *et al.,* 2016, their Fig.7a). As sediments become dehydrated during
294 subduction, the halogens associated to the porewater can be partitioned into phases that remain
295 stable to high *P* (lawsonite, phengite, etc.). Their observation, concordant with that by John *et al.*
296 (2011) and Kendrick *et al.* (2015), is that Br/Cl and I/Cl are positively correlated during
297 dehydration.

298 The process proposed by Broadley *et al.* (2016) accounts for the negative correlation of Br/Cl
299 with I/Cl of the fluid inclusion samples from North Victoria Land (Antarctica). These authors
300 attribute an important role to the different fluid/mineral partition behaviour of Br and I as a function
301 of pressure. This explains the empirically observed upward curvature of the field of marine pore
302 fluids in Fig. 11. Fluid inclusions from Mount Overlord have I/Br > 1, the most extreme ones a
303 molar ratio I/Br > 10. It is remarkable that Broadley *et al.* (2016, Table 2) document that fluid
304 inclusions in olivine are never in chemical equilibrium with those in orthopyroxene; the relative
305 enrichment of the I/Br ratio ranges between 2 and 300. This is not just an effect of the ionic radius,
306 as the Xe/Kr ratio of all samples in Table 2 is constant within a factor of 2 and shows no correlation
307 with I/Br. It can be speculated that primary and secondary inclusions could record very different
308 conditions of entrapment, and that their mass balance could be extremely variable among rocks and
309 among minerals of the same rock. Broadley *et al.* (2016) point out that the trapping of halogens in
310 the xenoliths was not a single-stage process, and suggest that a recent infiltration from the
311 asthenosphere was superimposed on a pre-existing subcontinental lithospheric mantle.

312 The coupled increase of I/Cl and decrease of Br/Cl of El Hierro fluid inclusions relative to the
313 "typical" mantle Br/Cl and I/Cl values is thus incompatible with a single-stage dehydration process.

314 The high I/Cl ratios of our samples approach, but do not reach, the most extreme samples from Mt.
315 Overlord (Broadley *et al.,* 2016). This could be explained either as fluids originated by dehydration
316 or melting of eclogite-facies serpentinites and metasediments in the mantle (Kendrick *et al.,* 2013b;
317 and references therein) or as remnants of the West African continental lithosphere (likely to bear
318 witness to multiple Proterozoic subduction events during its assembly) that were dismembered but
319 not entirely obliterated during the Jurassic rifting episode that created the present-day Atlantic.
320 Independently of the present work, the hypothesis that in the mantle beneath El Hierro there
321 might be a destabilised, crustal component had already been proposed in the literature. Day *et al.*
322 (2010) reported radiogenic isotope data in alkali-basalts from La Palma and El Hierro, and more
323 generally for the Canary Islands and interpreted it to suggest the presence of recycled oceanic crust
324 in their source (Marcantonio *et al.,* 1995; Widom *et al.,* 1999; Gurenko *et al.,* 2009; Day *et al.,*
325 2010). The present halogen data support the proposed geochemical anomaly of the upper mantle
326 beneath the Canary Islands (Day *et al.,* 2010, and references therein), relative to the "typical"
327 oceanic litho-spheric mantle. This anomaly could have been induced by metasomatic fluids
328 originating from portions of recycled old oceanic crust (subducted metabasalts + metasediments) at
329 lithospheric depths.
330 The Ba/Br ratio of the El Hierro fluid inclusions is 2-3 orders of magnitude higher than in
331 fluid inclusions from crustal granites (Kurosawa *et al.,* 2016). This may constrain future models that
332 attempt to characterise the processes giving rise to the metasomatising fluids in the lithospheric
333 mantle at 60 km depth. At present, the relative behaviour of Ba and Br is not widely reported; the
334 possibility to quantitatively determine it in the fluid inclusions by analysing $^{131}Xe_{Ba}$ should vastly
335 increase the available data-base, which at presents consists of just two papers.
336
337
338

6. Conclusions

The fluid inclusions of both analysed mantle rocks from El Hierro, spinel harzburgite and spinel dunite, have indistinguishable Br/Cl and I/Cl ratios. The Ba/Br ratio is also nearly uniform in the two rocks.

The halogen pattern in the fluid inclusions is distinct from the MORB/OIB field. Their Br/Cl ratio is lower by ca. 30%, and the I/Cl ratio higher by a factor of at least 30, than what is presently considered the "typical" oceanic basalt (e.g., Kendrick *et al.,* 2014). This halogen pattern is unusual, but it is not the most extreme observed in the literature. In order to fractionate the halogens at mantle depths in the direction of the El Hierro fluid inclusions it is necessary to envisage a two-stage process, by which fresh infiltration of fluids from the asthenosphere is superimposed on a pre-existing lithospheric signature involving remnants of continental crust.

Acknowledgements

Mark Kendrick provided the SY scapolite monitor, without which the halogen ratio measurements would have been impossible. Thomas Pettke determined Br and U concentrations on scapolite SY. Simona Ferrando provided facilities for Raman analyses. Funding was provided by Department funds, Dipartimento di Scienze dell'Ambiente e della Terra, Università di Milano Bicocca.

References

Abu El-Rus, M.A., Neumann, E.R., Peters, V. (2006). Serpentinization and dehydration in the upper mantle beneath Fuerteventura (eastern Canary Islands): Evidence from mantle xenoliths. *Lithos*, *89*, 24–46.

Andersen, T., O'Reilly, S.Y., Griffin, W.L. (1984). The trapped fluids phase in upper mantle xenoliths from Victoria, Australia: implications for mantle metasomatism. *Contrib. Mineral. Petrol., 88*, 72-85.

Andersen, T., Neumann, E.R. (2001). Fluid inclusions in mantle xenoliths. *Lithos, 55*, 301-320.

Anguita, F., Hernán, F. (2000). The Canary Islands origin: a unifying model. *Journal of Volcanology and Geothermal Research*, *103*(1-4), 1–26.

Bali, E., Audetat, A., Keppler, H. (2011). The mobility of U and Th in subduction zone fluids: an indicator of oxygen fugacity and fluid salinity. *Contrib. Mineral. Petrol., 161*, 597-613.

Becerril, L., Cappello, A., Galindo, I., Neri, M., Del Negro, C. (2013). Spatial probability distribution of future volcanic eruptions at El Hierro Island (Canary Islands, Spain). *Journal of Volcanology and Geothermal Research*, *257*, 21–30.

Böhlke J.K., Irwin J.J., 1992. Laser microprobe analyses of Cl, Br, I and K in fluid inclusions: Implications for sources of salinity in some ancient hydrothermal fluids. *Geochimica et Cosmochimica Acta*, *56*, 203-225.

Broadley, M.W., Ballentine, C.J., Chavrit, D., Dallai, L., Burgess, R. (2016) Sedimentary halogens and noble gases within Western Antarctic xenoliths: Implications of extensive volatile recycling to the sub continental lithospheric mantle. *Geochimica et Cosmochimica Acta, 176*, 139–156.

Bureau, H., Keppler, H. (1999). Complete miscibility between silicate melts and hydrous fluids in the upper mantle: experimental evidence and geochemical implications. *Earth Planet. Sci. Lett., 165*, 187-196.

Burgess, R., Layzelle, E., Turner, G., Harris, J.W. (2002). Constraints on the age and halogen composition of mantle fluids in Siberian coated diamonds. *Earth Planet Sci. Lett., 197*, 193-203.

Carracedo, J.C., Badiola, E.R., Guillou, H., de La Nuez, J., Pérez Torrado, F.J. (2001). Geology and volcanology of La Palma and El Hierro (Canary Islands). *Estudios Geol.*, *57*, 175-273.

Carracedo, J.C., Pérez Torrado, F., Rodríguez González, A., Soler, V., Fernández Turiel, J.L., Troll, V.R., Wiesmaier, S. (2011). The 2011 submarine volcanic eruption in El Hierro (Canary Islands). *Geology Today*, *28*(2), 53–58.

Dasgupta, R., Hirschmann, M. M., Smith, N. D. (2007). Partial melting experiments of peridotite + CO2 at 3 GPa and genesis of alkalic ocean island basalts. *J Petrology*, *48*(11), 2093–2124.

Day, J.M.D., Pearson, D.G., Macpherson, C.G., Lowry, D., Carracedo, J.C. (2010). Evidence for distinct proportions of subducted oceanic crust and lithosphere in HIMU-type mantle beneath El Hierro and La Palma, Canary Islands. *Geochimica et Cosmochimica Acta*, *74*, 6565–6589.

De Vivo, B., Frezzotti, M.L., Lima, A. (1988). Spinel lherzolite nodules from Oahu Island (Hawaii): a fluid inclusion study. *Bull. Minéral., 111*, 307-319.

Dixon, J.E., Leist, L., Langmuir, C., Schilling, J.C. (2002). Recycled dehydratrated lithosphere observed in plume-influenced mid-ocean-ridge basalt. *Nature, 420*, 385-389.

Foulger, G.R., Natland, J.H., Anderson, D.L. (2005). A source for Icelandic magmas in remelted Iapetus crust, *141*, 23–44.

Frezzotti, M.L., Andersen, T., Neumann, E. (2002). Carbonatite melt – CO 2 fluid inclusions in mantle xenoliths from Tenerife, Canary Islands: a story of trapping, immiscibility and fluid – rock interaction in the upper mantle, *64*, 77–96.

Frezzotti, M.L., Peccerillo, A. (2007). Diamond-bearing C-O-H-S fluids in the mantle beneath Hawaii. *Earth Planet Sci. Lett., 262*, 273-283.

Frezzotti, M.L., Ferrando, S., Peccerillo, A., Petrelli, M., Tecce, F., Perucchi, A. (2010). Chlorine-rich metasomatic H2O-CO2 fluids in amphibole-bearing peridotites from Injibara (Lake Tana region, Ethiopian plateau): Nature and evolution of volatiles in the mantle of a region of continental flood basalts. *Geochimica et Cosmochimica Acta*, *74*(10), 3023–3039. Frezzotti, M.L., Ferrando, S., Tecce, F., Castelli, D. (2012). Water content and nature of solutes in shallow-mantle fluids. *Earth Planet. Sci. Lett.*, 351-352, 70-83.

Frezzotti, M.L., Ferrando, S. (2016). Halogens in the mantle lithosphere, *in Harlov, D., ed., Halogens in the Earth, Springer*, in press.

Gee, M.J.R., Masson, D.G., Watts, A.B., Mitchell, N.C. (2001). Offshore continuation of volcanic rift zones, El Hierro, Canary Islands. *Journal of Volcanology and Geothermal Research*, *105*(1-2), 109–119.

Guillou, H., Carracedo, J.C., Torrado, F.P., Badiola, E.R. (1996). K-Ar ages and magnetic stratigraphy of a hotspot-induced, fast grown oceanic island: El Hierro, Canary Islands. *Journal of Volcanology and Geothermal Research*, *73*(1-2), 141–155.

Gurenko A.A., Sobolev A.V., Hoernle K.A., Hauff F. and Schmincke H.-U. (2009) Enriched, HIMU-type peridotite and depleted recycled pyroxenite in the Canary plume: a mixed-up mantle. Earth Planet. Sci. Lett.277, 514–524.

Hansteen, T.H., Andersen, T., Neumann, E.R., Jelsma, H. (1991). Fluid and silicate glass inclusions in ultramafic and mafic xenoliths from Hierro, Canary Islands: implications for mantle metasomatism. *Contrib Mineral Petrol*, *107*(2), 242–254.

Ito, E., Harris, D.M., Anderson, A.T. (1983). Alteration of oceanic crust and geologic cycling of chlorine and water. *Geochim. Cosmochim. Acta, 47*, 1613-1624.

Izraeli, E.S., Harris, J.W., Navon, O. (2001). Brine inclusions in diamonds: A new upper mantle fluid. *Earth. Planet Sci. Lett., 187*, 323-332.

John, T., Scambelluri, M., Frische, M., Barnes, J.D., Bach, W. (2011). Dehydration of subducting serpentinite: Implications for halogen mobility in subduction zones and the deep halogen cycle. *Earth and Planetary Science Letters, 308*, 65-76.

Johnson, L.H., Burgess, R., Turner, G., Harris, J.H., Milledge, H.J. (2000). Noble gas and halogens geochemistry of mantle fluids in diamond: comparison of African and Canadian stones. *Geochim. Cosmochim. Acta, 64*, 717-732.

Kawamoto, T., Yoshikawa, M., Kumagai, Y., Mirabueno, M.H.T., Okuno, M., Kobayashi, T. (2013). Mantle wedge infiltrated with saline fluids from dehydration and decarbonation of subducting slab. *Proc. Nat. Acad. Sci., 110*, 9663-9668.

Kendrick, M.A. (2012). High precision Cl, Br and I determinations in mineral standards using the noble gas method. *Chemical Geology, 292-293*, 116-126.

Kendrick, M.A., Arculus, R., Burnard, P., Honda, M. (2013a). Quantifying brine assimilation by submarine magmas: Examples from the Galápagos Spreading Centre and Lau Basin. *Geochimica et Cosmochimica Acta*, *123*, 150–165.

Kendrick, M.A., Honda, M., Pettke, T., Scambelluri, M., Phillips, D., Giuliani, A. (2013b). Subduction zone fluxes of halogens and noble gases in seafloor and forearc serpentinites. *Earth and Planetary Science Letters*, *365*, 86–96.

Kendrick, M. A., Arculus, R. J., Danyushevsky, L. V., Kamenetsky, V. S., Woodhead, J. D., Honda, M. (2014). Subduction-related halogens (Cl, Br and I) and H2O in magmatic glasses from Southwest Pacific Backarc Basins. *Earth and Planetary Science Letters*, *400*, 165–176.

Klein-BenDavid, O., Izraeli, E.S., Hauri, E., Navon, O. (2007). Fluid inclusions in diamonds from the Diavik mine, Canada and the evolution of diamond-forming fluids. *Geochim. Cosmochim. Acta, 71*, 723-744.

Kurosawa, M., Sasa, K., Shin, K.-C., Ishii, S. (2016) Trace-element compositions and Br/Cl ratios of fluid inclusions in the Tsushima granite, Japan: Significance for formation of granite-derived fluids. *Geochimica et Cosmochimica Acta, 182*, 216-239.

Magenheim, A.J., Spivack, A.J., Micheal, P.J., Gieskes, J.M. (1995). Chlorine stable-isotope composition of the oceanic-crust – implications for Earth's distribution of chlorine. *Earth Planet, Sci. Lett., 131*, 427-432.

Marcantonio F., Zindler A., Elliott T. and Staudigel H. (1995) Os isotope systematics of La Palma, Canary Islands: evidence for recycled crust in the mantle source of HIMU ocean islands. Earth Planet. Sci. Lett.133, 397–410.

Martinez-Arevalo, C., Mancilla, F. de L., Helffrich, G., Garcia, A. (2013). Seismic evidence of a regional sublithospheric low velocity layer beneath the Canary Islands. *Tectonophysics*, *608*, 586–599.

McInnes, B.I.A., Gregoire, M., Binns, R.A., Herzig, P.M., Hannington, M.D. (2001). Hydrous metasomatism of oceanic sub-arc mantle, Lihir, Papua New Guinea: petrology and geochemistry of fluid-metasomatised mantle wedge xenoliths. *Earth Planet Sci. Lett., 188*, 169-183.

Neumann, E.R. (1991). Ultramafic and mafic xenoliths from El Hierro, Canary Islands: evidence for melt infiltration in the upper mantle. *Contrib Mineral Petrol, 106,* 236-252.

Neumann, E.R., Wulff-Pedersen, E., Johnsen, K., Andersen, T., Krogh, E. (1995). Petrogenesis of spinel harzburgite and dunite suite xenoliths from Lanzarote, eastern Canary Islands: Implications for the upper mantle. *Lithos*, *35*, 83–107.

Neumann, E.R., Wulff-Pedersen, E., Pearson, N.J., Spencer, E.A. (2002). Mantle Xenoliths from Tenerife (Canary Islands): Evidence for Reactions between Mantle Peridotites and Silicic Carbonatite Melts inducing Ca Metasomatism. *J Petrology*, *43*, 825–857.

Neumann, E.R., Griffin, W.L., Pearson, N.J., O'Reilly, S.Y. (2004). The Evolution of the Upper Mantle beneath the Canary Islands: Information from Trace Elements and Sr isotope Ratios in Minerals in Mantle Xenoliths. *J Petrology, 45*, 2573-2612.

Oglialoro, E., Frezzotti, M.L., Tiraboschi, C., Ferrando, S., Principe, C., Groppelli, G. (submitted). The magma plumbing system of the rift volcanism in El Hierro, Canary Islands: a fluid inclusions study. *Bulletin of Volcanology*, submitted.

Ozima, M., Podosek, F.A. (2002) Noble gas geochemistry, 2nd edition. Cambridge University Press, Cambridge.

Pagé, L., Hattori, K., de Hoog, J.C.M., Okay, A.I. (2016) Halogen (F, Cl, Br, I) behaviour in subducting slabs: A study of lawsonite blueschists in western Turkey. *Earth and Planetary Science Letters, 442,* 133-142.

Philippot, P. (1993). Fluid-melt-rock interaction in mafic eclogites and coesite-bearing metasediments: constraints on volatile recycling during subduction. *Chem. Geol., 108*, 93-112.

Roedder, E. (1965). Liquid CO_2 inclusions in olivine-bearing nodules and phenocrysts from basalts. *The American Mineralogist, 50,* 1746-1782.

Safonov, O.G., Kamenetsky, V.S., Perchuk, L.L. (2011). Links between carbonatite and kimberlite melts in chloride-carbonate-silicate systems: Experiments and application to natural assemblages. *J Petrology*, *52*, 1307–1331.

Scambelluri, M., Piccardo, G.B., Philippot, P., Robbiano, A. Negretti, L. (1997). High salinity fluid inclusions formed from recycled seawater in deeply subducted alpine serpentinite. *Earth Planet. Sci. Lett., 148*, 485-499.

Smith, E.M., Kopylova, M.G., Nowell, G.M., Pearson, D., Ryder, J. (2012). Archean mantle fluids preserved in diamonds from Wawa, Superior Craton. *Geology, 40(12)*, 1071-1074.

Viñuela, J.M. (2004). The Canary Islands Hot Spot. www.MantlePlumes.org

Webster, J.D. (1990). Partitioning of F between $H_2O \pm CO_2$ fluids and topaz rhyolite melt: Implications for mineralizing magmatic-hydrothermal fluids in F-rich granitic systems. *Contrib. Mineral. Petrol., 104*, 424-438.

Webster, J.D. (1992). Fluid-melt interactions involving Cl-rich granites: Experimental study from 2 to 8 kbar. *Geochim. Cosmochim. Acta, 56*, 679-687.

Widom, E., Hoernle, K. a, Shirey, S.B., Schmincke, H.U. (1999). Os Isotope Systematics in the Canary Islands and Madeira: Lithospheric Contamination and Mantle Plume Signatures. *J Petrology*, *40*(2), 279–296.

Wulff-Pedersen, E., Neumann, E.R., Jensen, B.B. (1996). The upper mantle under La Palma, Canary Islands: formation of Si-K-Na-rich melt and its importance as a metasomatic agent. *Contrib Mineral Petrol* , *125*(2-3), 113–139.

Wyllie, P.J. (1989). Origin of carbonatites: Evidence from phase equilibrium studies*, in Bell, K., ed., Carbonatites: Genesis and evolution: Boston, Unwin-Hyman,* p. 500-545.

You, C.F., Butterfield, D.A., Spivack, A.J., Gieskes, J.M., Gamo, T., Campbell, A.J. (1994). Boron and halide systematics in submarine hydrothermal systems: effects of phase separation and sedimentary contributions. *Earth and Planetary Science Letters, 123*, 227–238.

Figure Captions

Fig. 1 – Geological map of El Hierro with sampling localities. Different volcanism stages are presented in legend along with main structural elements (Modified from Becerril *et al*., 2013).

Fig. 2 – Classification of peridotites from the Canary Islands compared to those from the North Mid-Atlantic Ridge (gray field; Neumann *et al*., 2004; and references therein).

Fig. 3 – Olivine porphyroclasts (Ol) forming triple junction, orthopyroxene porphyroclast (Opx) and spinel crystal (Sp). Sample XML7. Crossed polarizers. Scale bar 2 mm.

Fig. 4 – First generation (porphyroclasts; Ol1) and second generation olivine (aligned neoblasts; Ol2). The yellow broken line highlights the foliation. Sample XML1 Crossed polarizers. Scale bar 2 mm.

Fig. 5 – Olivine porphyroclast with carbonate + spinel inclusion and carbonate + silicate melt short dendritic microveins. The high birefringence of solids in glass veins confirm the presence of carbonate aggregates. Crossed (A) and parallel polarizers (B).

Fig. 6 – Intergranular trail (red arrow) of CO_2-rich fluid inclusions.

Fig. 7 – Raman spectra of fluids and phases trapped in Type II fluid inclusion.

Fig. 8 – Raman spectra revealing the presence of $MgSO_4 \cdot nH_2O$ in Type II fluid inclusion.

Fig. 9 – Image and Raman microprobe maps of phases in one Type II fluid inclusion. (a) Image of Type II fluid inclusion. (b) Single Raman spectrum characterizes six different mineral phases: anhydrite, apatite, dolomite, $MgSO_4 \cdot nH_2O$, sulfohalite and spinel. (c) Reconstruction of mineral association recognized within fluid inclusion: anhydrite (Anh), apatite (Ap), dolomite (Dol), $MgSO_4 \cdot nH_2O$, sulfohalite (Shl) and spinel (Sp).

Fig. 10 – Differential release rate, *R*, of Xe and Kr as a function of *T*. (a) Release rate of Xe from whole rock XML1. Four Xe components, corresponding to different carrier phases, are evidenced. (b) Kr release from XML1. Three components mirror the corresponding ones observed in the Xe release. (c) Coincident differential release of uranogenic Xe and Kr in whole rock XML1. (d) Differential release of halogen-derived Ar, Kr and Xe for sample XML1. Up to 1000 °C, mineral phases and possible surface contamination dominate the halogen release, in which the three noble gases are decoupled. Parallel release of Ar, Kr and Xe in the 1200 and 1400 °C steps are best explained by decrepitation of saline fluid inclusions.

Fig. 11 – Br/Cl vs. I/Cl ratio diagram for fluid inclusions in different terrestrial rock types (after Kendrick *et al*., 2014, and Pagé *et al*., 2016).

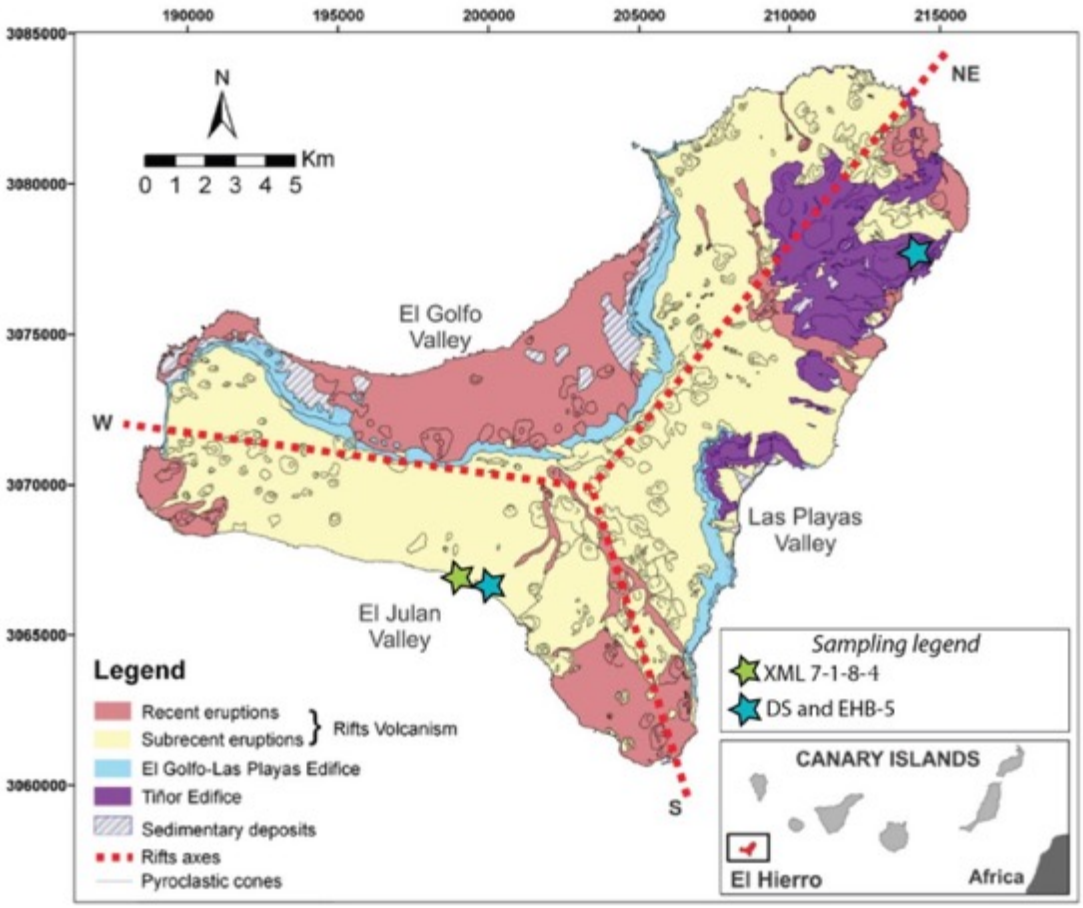

Villa et. al-**Fig. 1**

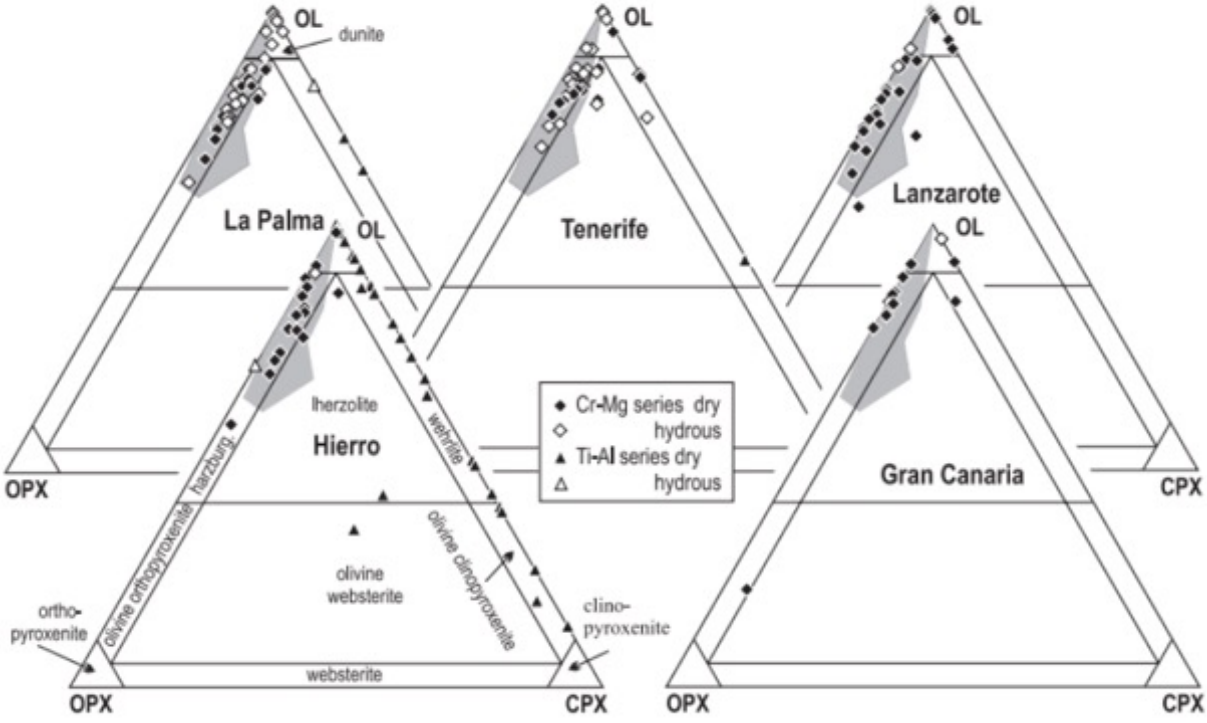

Villa et. al-**Fig. 2**

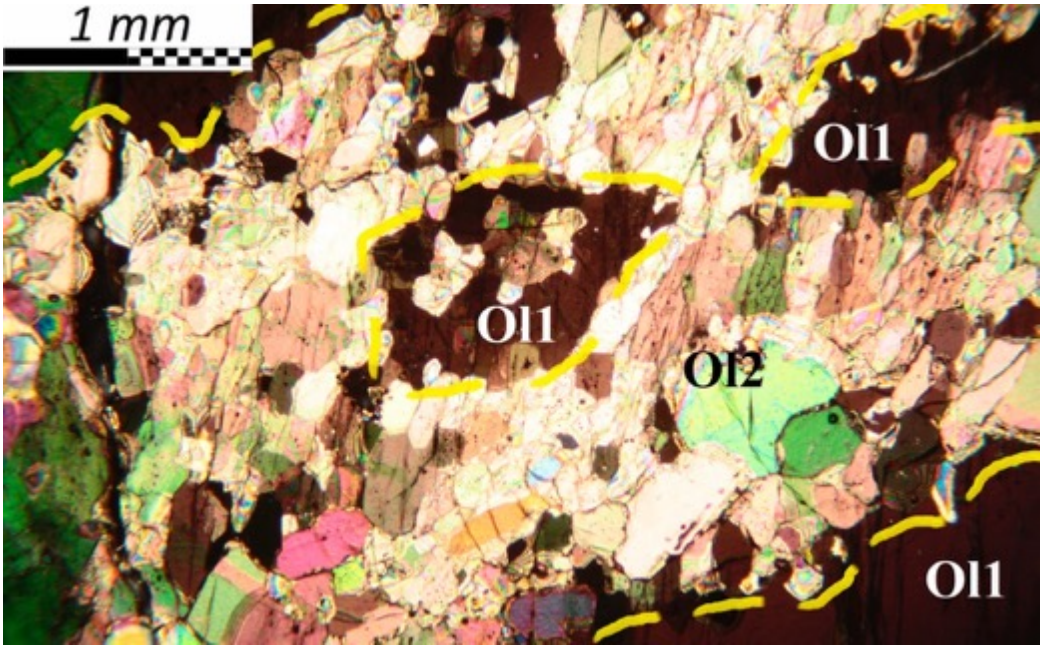

Villa et. al-**Fig. 3**

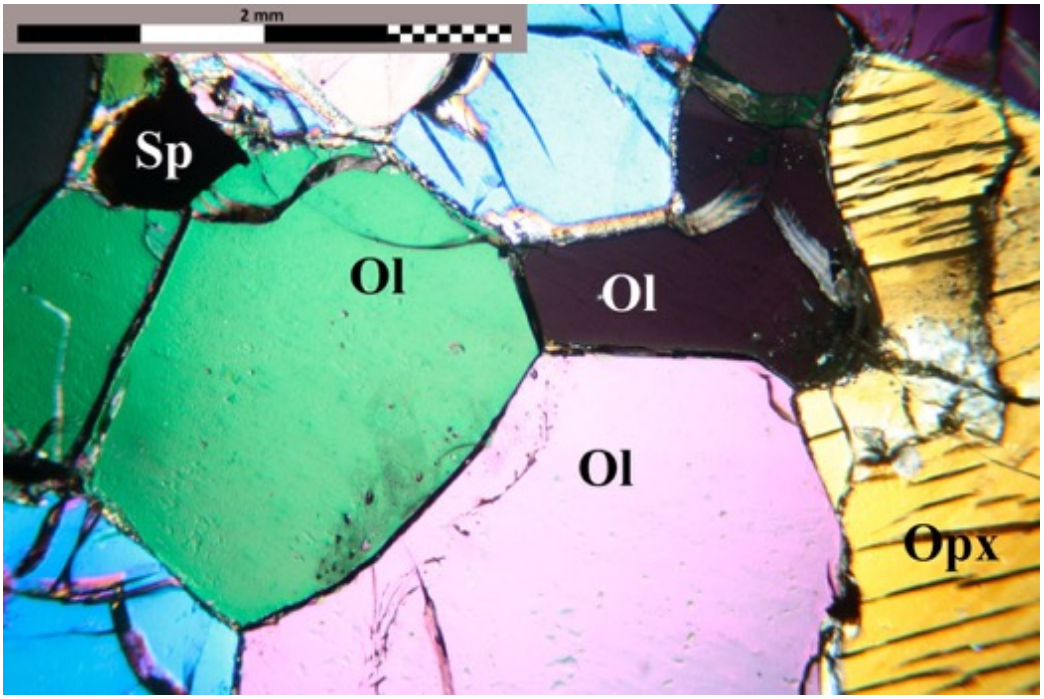

Villa et. al-**Fig. 4**

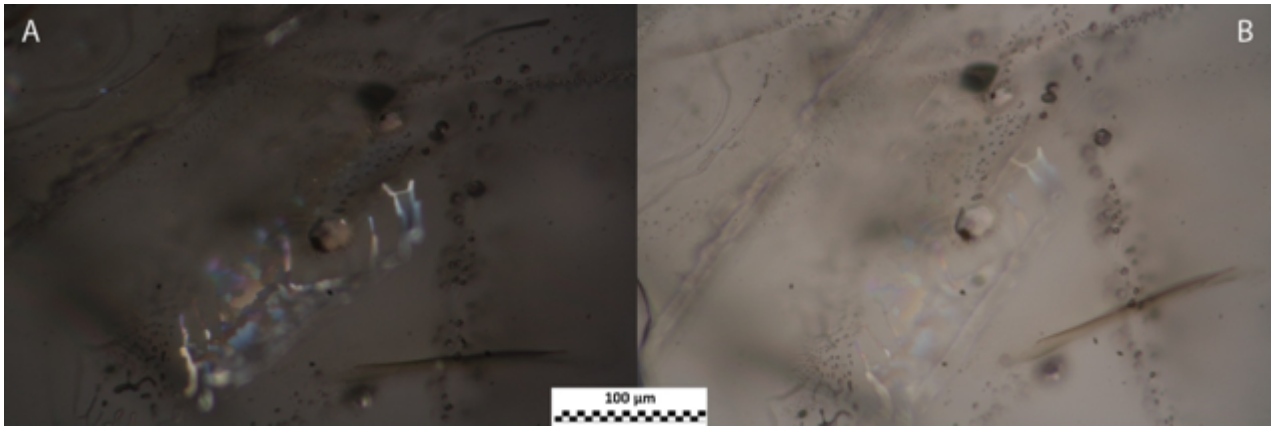

Villa et. al-**Fig. 5**

Villa et. al-**Fig. 6**

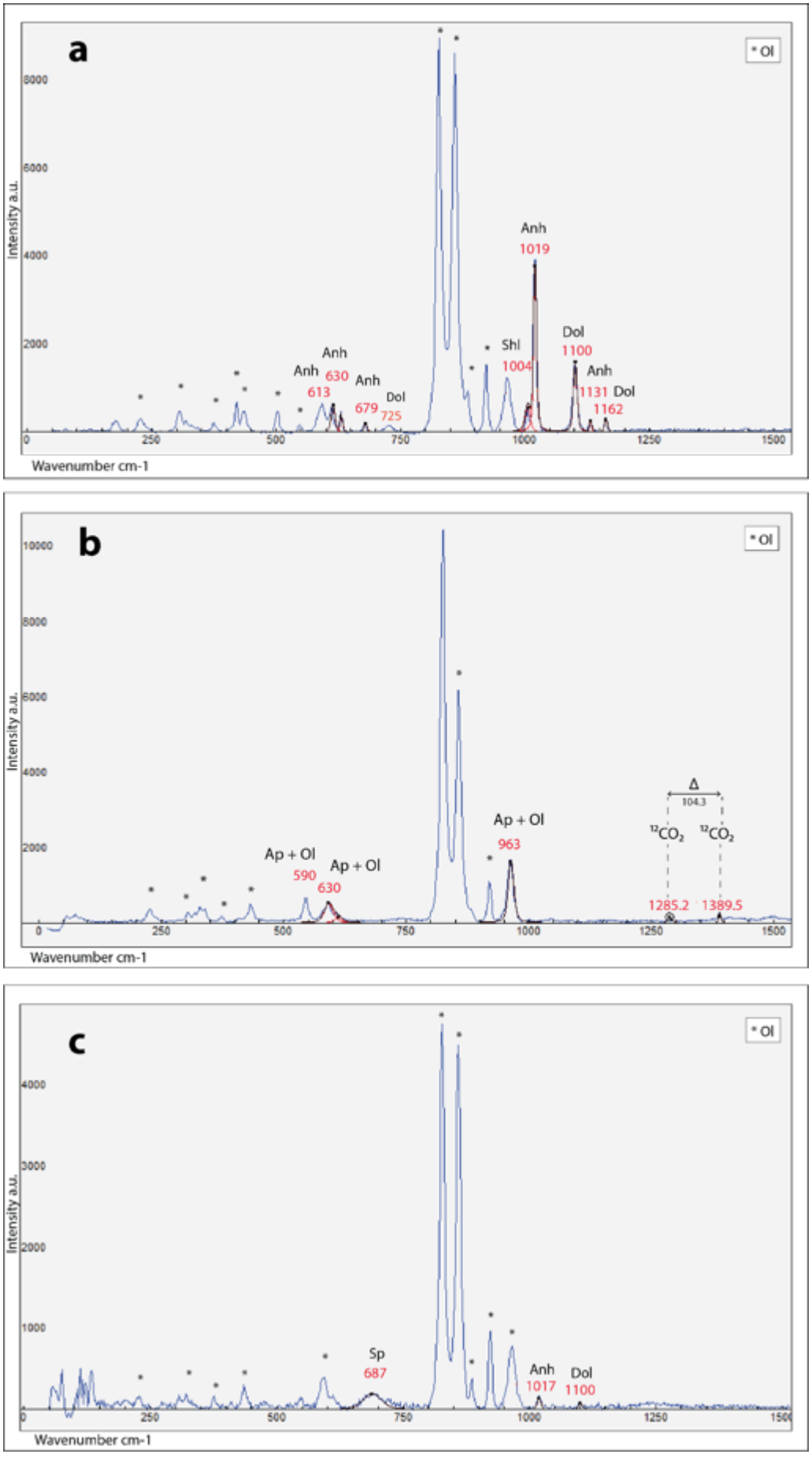

Villa et. al-**Fig. 7**

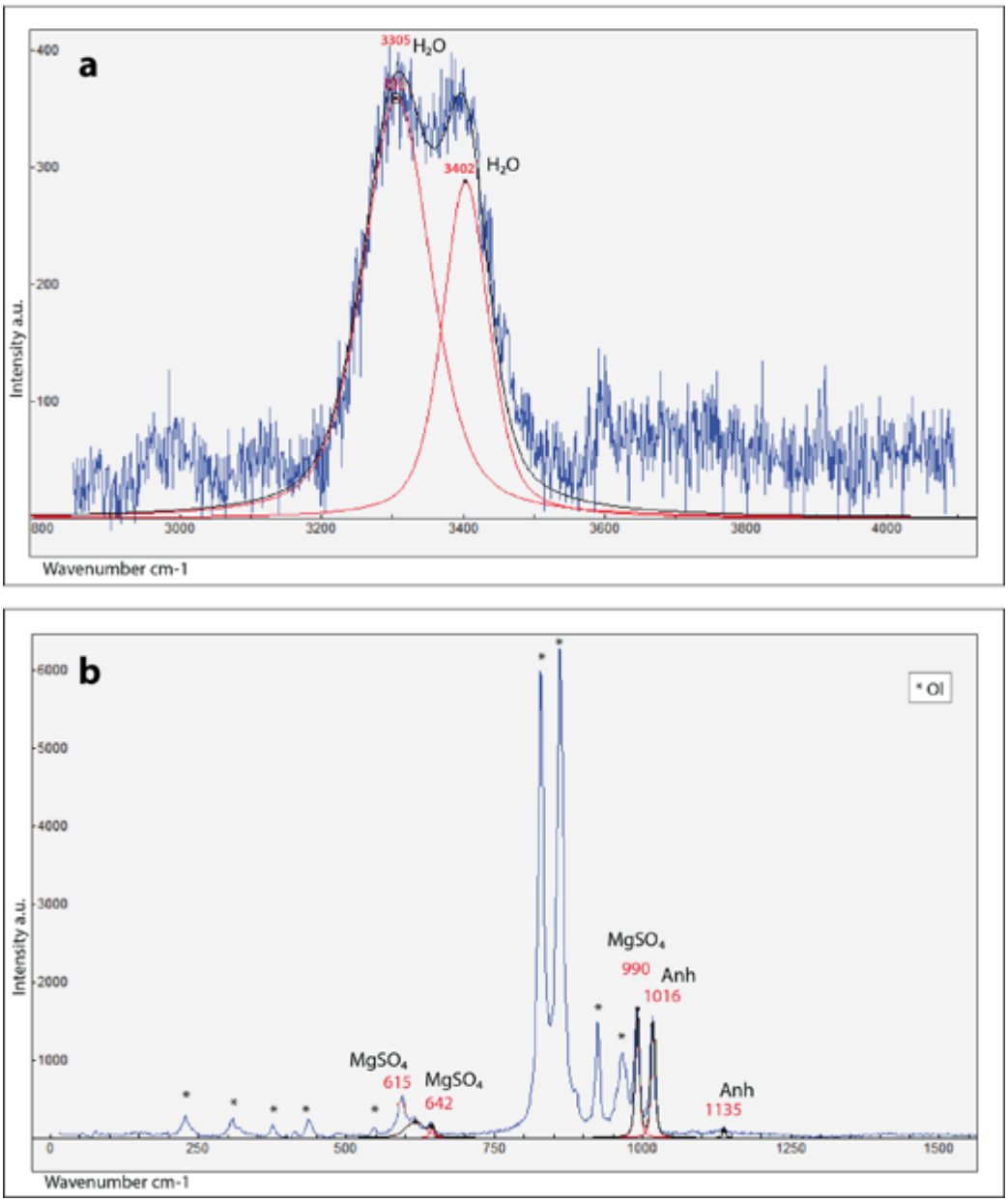

Villa et. al-**Fig. 8**

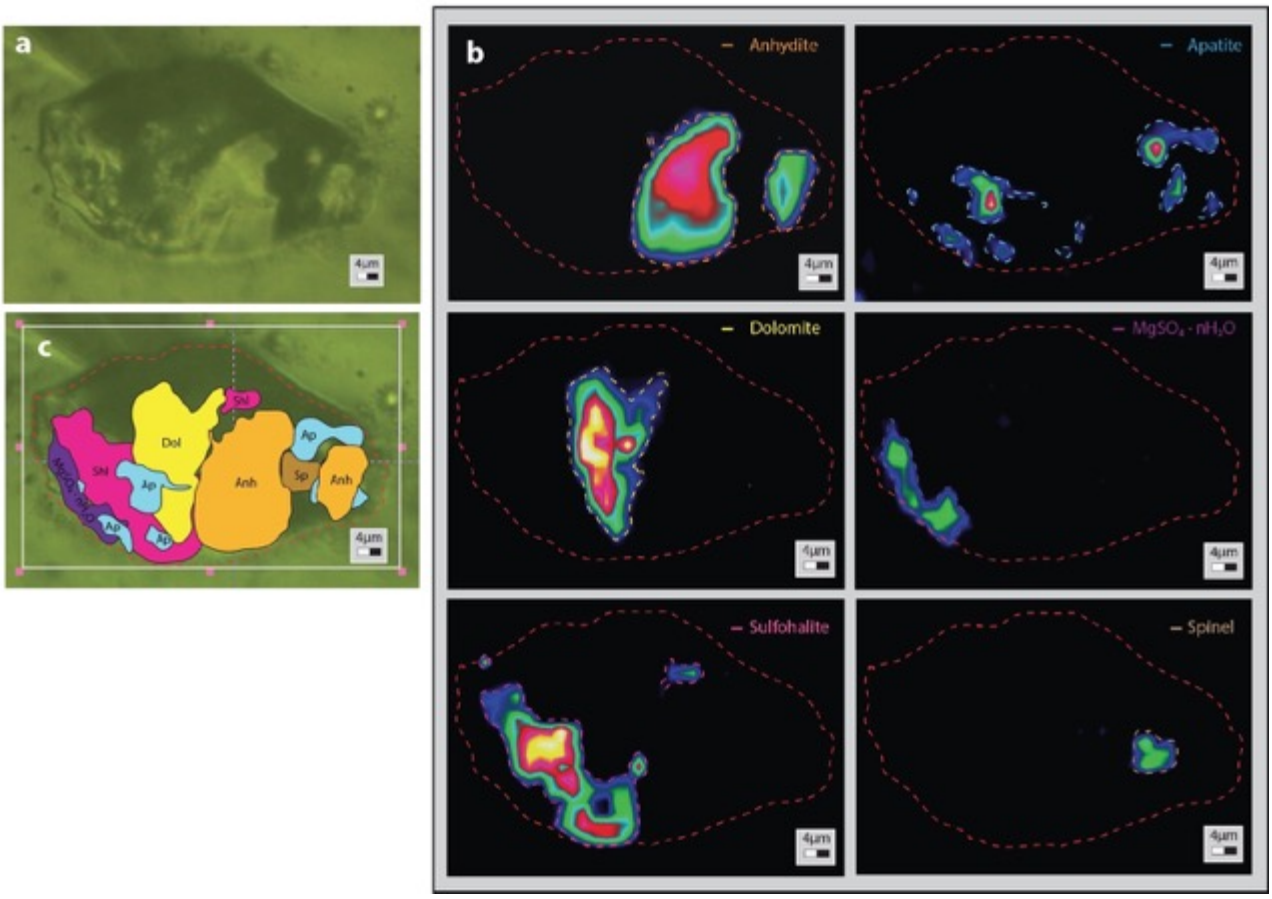

Villa et. al-**Fig. 9**

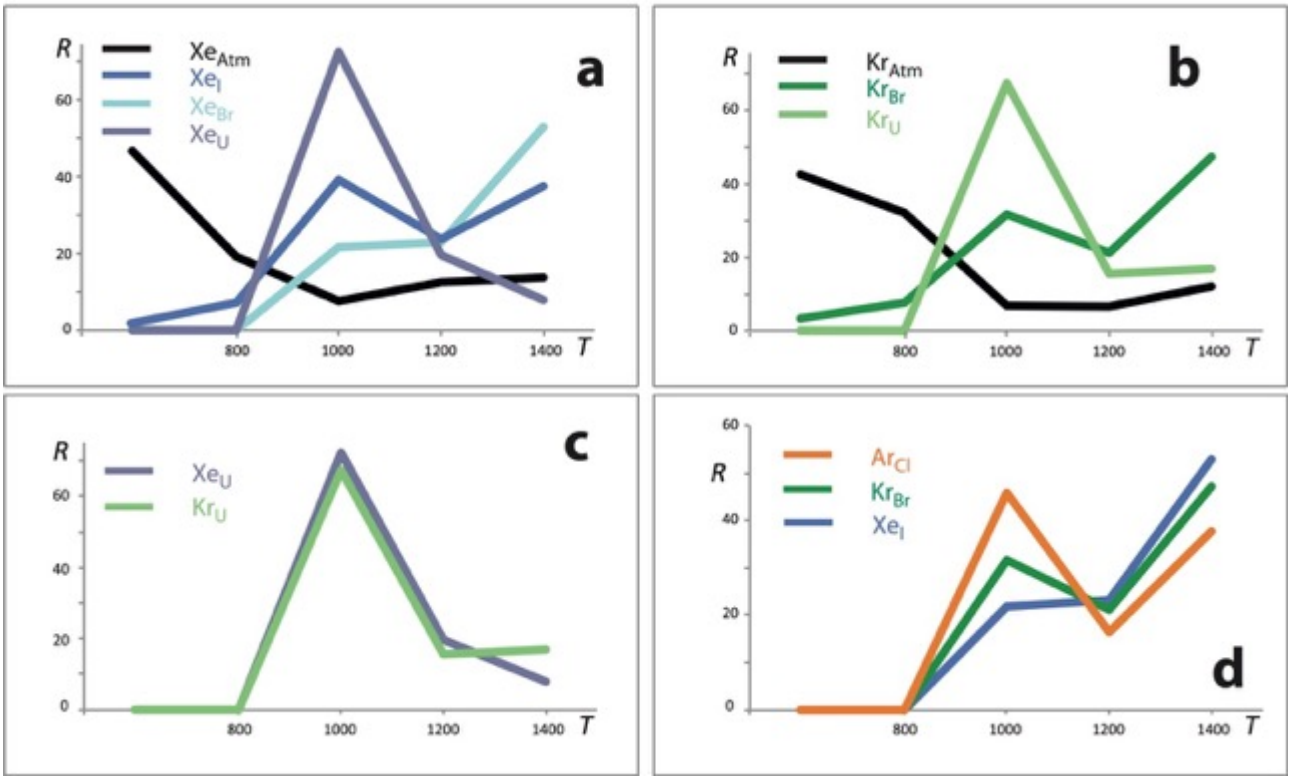

Villa et. al-**Fig. 10**

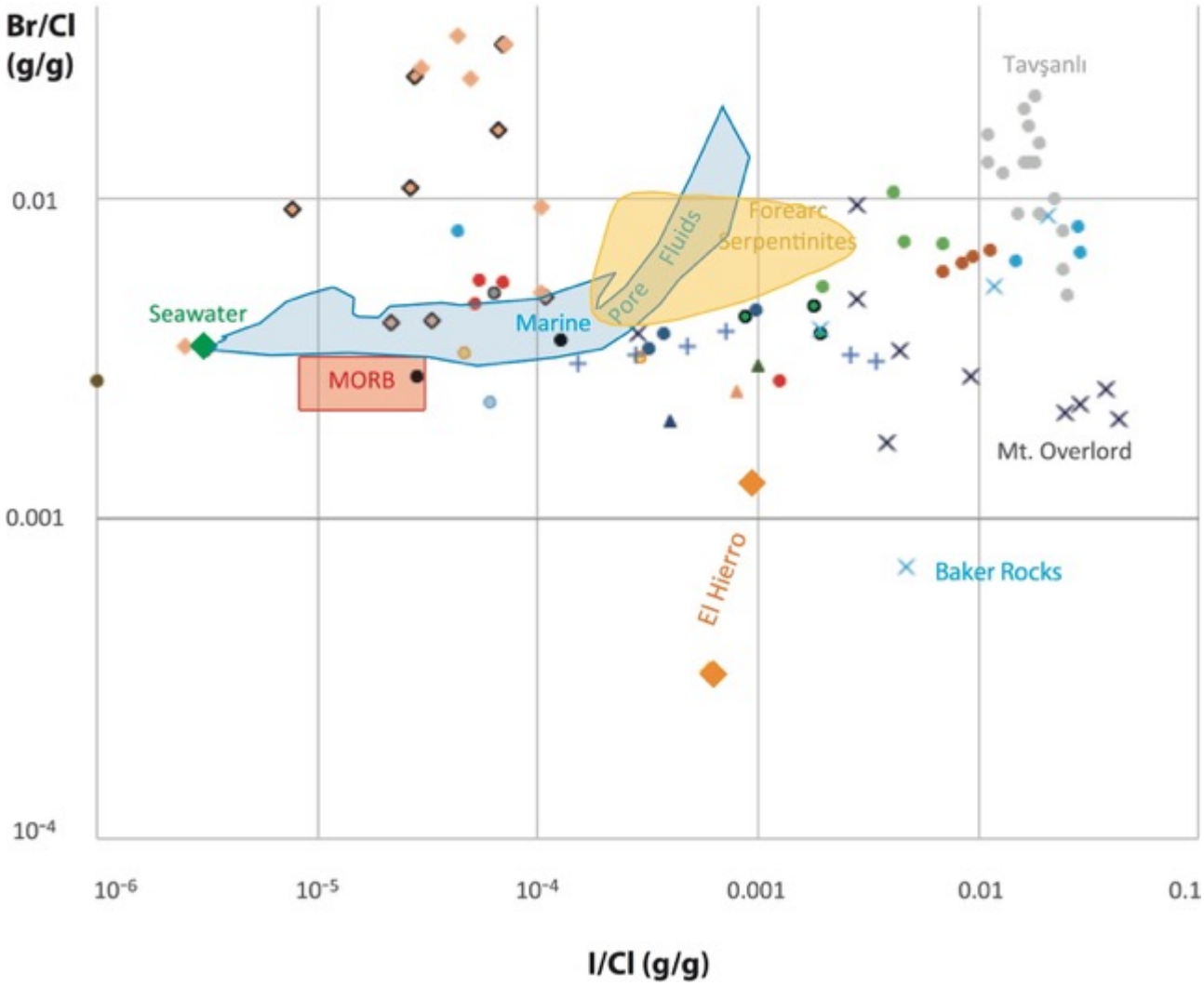

Villa et. al-**Fig. 11**

sample	T	128Xe	err	128XeI	XeI%	129Xe
XML1-step1	600	2.61E-18	2.83E-19	2.82E-19	1.8	3.20E-17
XML1-step2	800	1.78E-18	2.83E-19	8.22E-19	5.3	1.32E-17
XML1-step3	1000	5.97E-18	2.36E-19	5.59E-18	36.2	5.20E-18
XML1-step4	1200	4.01E-18	2.52E-19	3.38E-18	21.9	8.63E-18
XML1-step5	1400	6.05E-18	2.44E-19	5.37E-18	34.8	9.25E-18
XML7-step1	600	1.01E-17	2.57E-19	6.90E-18	9.1	4.37E-17
XML7-step2	800	3.77E-17	3.08E-19	3.48E-17	45.8	3.98E-17
XML7-step3	1000	2.91E-17	3.08E-19	2.87E-17	37.7	5.78E-18
XML7-step4	1400	6.47E-18	2.06E-19	5.68E-18	7.5	1.08E-17

Villa et. al-**Tab.1**

6. MANUSCRIPT 2: *submitted to Bulletin of Volcanology on 16th January 2017*

Lithospheric magma dynamics beneath El Hierro, Canary Islands: a fluid inclusion study

E. Oglialoro[1], M.L. Frezzotti[1], S. Ferrando[2], C. Tiraboschi[1], C. Principe[3], G. Groppelli[4], I.M. Villa,[1,5,6]

1-Dipartimento di Scienze dell'Ambiente e della Terra, Università di Milano Bicocca, 20126 Milan, Italy
2-Dipartimento di Scienze Mineralogiche e Petrologiche, Università diTorino, 70125 Turin, Italy
3-Istituto di Geoscienze e Georisorse, Consiglio Nazionale delle Ricerche, 56121 Pisa, Italy
4-Istituto per la Dinamica dei Processi Ambientali-sezione di Milano, Consiglio Nazionale delle Ricerche, 20131 Milan, Italy
5-Institut für Geologie, Universität Bern, 3012 Bern, Switzerland
6-Centro Universitario Datazioni e Archeometria, Università di Milano Bicocca, 20126 Milano, Italy

Corresponding author: eduoglia88@gmail.com; e.oglialoro@campus.unimib.it

Abstract

In active volcanoes, fluid inclusions and petrological studies combined with volcanological data have been proven to represent a reliable approach to define the depth conditions of magma storage and degassing paths, which lead to the characterization of the magma plumbing system. This approach has been applied to investigate the Rift Volcanism activity during the last 50 ka, in El Hierro (Canary Islands). In particular, fluid inclusion studies have been conducted on ultramafic xenoliths in a lava flow of El Julan Cliff Valley. Two fluid inclusions groups have been observed: i) *Type I*, early multiphase CO_2+N_2-rich fluid inclusions, trapped prior to the ascent of the host xenoliths; ii) *Type II*, late pure CO_2 fluid inclusions trapped during the ascent into the host magma. Density values have been obtained through microthermometry and Raman analysis. *Type I* fluid inclusions exhibit scattered density values as low as 0.87 g/cm^3 to extremely high at 1.19 g/cm^3, suggesting pressures from 0.95 to 1.8 GPa (30–60 km), describing a deep origin of the fluid. *Type II* fluid inclusions show a bimodal distribution of homogenization temperature, corresponding to two density intervals: from 0.99 to 1.11 g/cm^3 and from 0.65 to 0.75 g/cm^3. These data indicate a pressure interval from 0.67 to 1 GPa and from 0.26 to 0.34 GPa. We propose a model where the eruptive dynamics originate from a vertically stacked magma reservoir in the lithospheric mantle, which has been identified, for the first time in El Hierro Island, from 22 to 36 km depth, followed by local magma accumulation at lower crustal levels from 10 to 12 km (0.26–0.34 GPa). The results obtained have been compared with the dynamics of magma ascent of the last eruption of 2011-2012 of the island, in order to understand whether the magma plumbing system beneath El Hierro island was involved during the last 40 ka.

Introduction

Modelling the magma plumbing system of ancient and/or active volcanoes is an essential prerequisite to evaluate the monitoring strategies for forecasting volcanic eruptions (e.g. Scandone et al. 2007, and references therein). Pressure, and hence depth, conditions of magma rest in the crust and/or in the mantle can be revealed by using different investigation methods, including geophysics, petrology, geochemistry, and experimental petrology (e.g. Hansteen et al. 1998; Klügel et al. 2000; Bertagnini et al. 2002; Schwarz et al. 2004; Klügel et al. 2005; Mattioli et al. 2006; Morgan et al. 2007; Stroncik et al. 2009). Fluid inclusion geothermobarometry combined with petrological studies represent an effective additional method to reconstruct the magma plumbing system of active volcanoes (e.g., Roedder 1983; Zanon et al. 2003; Frezzotti and Peccerillo 2004; Hansteen and Klügel 2006). This approach has been successfully applied to reconstruct the evolution and conditions of magma ascent in active volcanoes in oceanic and continental settings, such as Hawaii Islands (e.g. Roedder 1983; De Vivo et al. 1988), Cape Verde archipelago (e.g., Hildner et al. 2011; Holm et al. 2008), Azores archipelago (e.g. Zanon and Frezzotti 2013; Zanon. 2015), Canary Islands (e.g., Hansteen et al. 1991, 1998; Frezzotti et al. 1994, 2002; Andersen et al. 1995; Neumann et al. 1995; Klügel et al. 2005), and Aeolian Islands (Belkin and De Vivo 1993; Frezzotti et al. 2003; Zanon et al. 2003; Vaggelli et al. 2003; Bonelli et al. 2004; Peccerillo et al. 2006; Zanon and Nikogosian 2004; Di Martino et al. 2010). In the Canary Islands, geothermobarometric studies of fluids and minerals in mantle xenoliths rocks have been proposed for Gran Canaria, La Palma, El Hierro, Lanzarote, and La Gomera (e.g., Hansteen et al. 1991, 1998; Frezzotti et al. 1994, 2002; Andersen et al. 1995; Neumann et al. 1995; Klügel et al. 2005). The presence of one or more magma reservoirs at the Moho and/or in the lower oceanic crust have been proposed for all the islands of the archipelago (cf., Hansteen et al. 1998).

At El Hierro, the youngest and westernmost of Canary Islands, an important multidisciplinary effort has been concentrated to characterize the magma dynamics of El Hierro volcano since last

eruption of 2011-2012 in the area of La Restinga (SE of the island) (i.e., Meletlidis et al. 2012; Becerril et al. 2013b; González et al. 2013; Martí et al. 2013a, b; Longpré et al. 2014). Proposed model, based on several independent analytical approaches (e.g., mineral/melt geochemistry, fluid inclusion, geophysics, feeder dykes structures, and geodetic-picture analyses) suggests two main interconnected reservoirs of magma, in the lower oceanic crust and in the lithospheric mantle (cf. Martì et al. 2013b). As recently summarized by Klügel et al. (2015), at El Hierro, eruptive magma transport is characterized by sub-horizontal and lateral magma pathways forming temporary deep sheet intrusions (sills) in the lower crust. Less is, however, known on the deeper magma ascent mechanisms, although the intense pre-eruptive seismicity recorded at 20-25 km suggests that eruption of basanitic magmas originated from a deep-seated reservoir located in the lithospheric mantle beneath El Hierro Island (cf., Martì et al. 2013a).

In this work, we concentrate on the reconstruction of the magma plumbing system of El Hierro Island, focussing on magma ascent dynamics in the lithospheric mantle. Following the approach of Frezzotti and Peccerillo (2004), have performed a detailed petrological and fluid inclusion investigation in ultramafic xenoliths from a lava flow of El Julan (Fig. 1b, red star) (SE of the island; 50 ka; Guillou et al. 1996; Carracedo et al. 2001), which is considered as representative for volcanic activity at about 40 ka (Rift Volcanism activity; 158 ka-present; Becerril et al. 2013a). We discuss the dynamics of magma ascent and rest from upper mantle conditions to the Earth's surface. Results indicate, for the first time, that the magma ascent in the lithospheric mantle occurs as a continuous migration through a plexus of vertically-stacked interconnected magma pockets, at depths consistent with those recorded by the pre/sin-eruptive seismic sequences of the 2011-2012 eruption.

Geological setting and volcanic history

The Canary Archipelago (Spain) is composed of seven main volcanic islands located on the continental rise off Cape Juby, (northwest Africa) and it extends for roughly 500 km in a ridge that

86 has devoloped on the passive margin of the African Plate in the eastern (central Atlantic Ocean)
87 (Fig. 1a), (Robertson and Stillman 1979; Marinoni and Pasquarè 1994; Carracedo et al. 1999;
88 Marinoni and Gudmundsson 2000). A model focusing on the genesis of Canary Island has been
89 recently proposed by Duggen et al. (2009): there is theorized the presence of a flow-mantle plume
90 material along a sub continental lithospheric corridor, located under the western Canaries; it also
91 supposed that the material flows to the east beneath the Atlas Mountains (Africa) and interacts with
92 the tectonic processes characterizing the lithosphere in this region (Martinez-Arevalo et al. 2013;
93 Martí et al. 2013a). The main regional tectonic structures have been classified in Atlantic or
94 "oceanic" (N160–N180°E, N120–N135°E) and in African or "continental" (N20°E, N45°E, N75°E)
95 (Anguita and Hernan 1975, 2000; Fuster 1975; Geyer and Martí 2010). The depth of Moho
96 discontinuity is variable below the Canary Islands: at about 35 km for Lanzarote and, for a
97 progressive thinning of the crust, at 15-12 km for El Hierro Island (Martinez-Arevalo et al. 2013).
98 The presence of Jurassic basaltic oceanic crust beneath the entire Canary Island archipelago has
99 been documented by MORB-composition metabasalt and gabbro fragments occurring in Miocene
100 fanglomerates on Gran Canaria and by abundant MORB-gabbro xenoliths in basanite lava on La
101 Palma and Lanzarote (Schmincke et al. 1998; Abu El-Rus et al. 2006). The sub-aerial volcanic
102 activity in the Archipelago show a westwards decrease in age and different stage of growth of the
103 islands: *post-erosional stage* [Fuerteventura (20 Ma), Lanzarote (15.5 Ma) and Gran Canaria (14.5
104 Ma)], *repose or gap stage* [La Gomera (12 Ma)], and *shield stage* of growth [Tenerife (7.5Ma), La
105 Palma (2 Ma) and El Hierro (1.12 Ma)] (Fig.1 a), (Schmincke 1982; Carracedo 1999). Large
106 chemical composition from picrite basalts to mafic trachytes, with abundant intermediate terms, is
107 well defined in the volcanic products of the islands (Hoernle and Schmincke 1993; Stoncik et al.
108 2009).

109 El Hierro Island is smallest and westernmost of the Canary Archipelago. With an area of
110 about 269 km^2, this volcanic island in its shield stage of growth rises from a depth of 3700-4000m
111 and the entire volcanic building reaches a height of 1500 m a.s.l. (Carracedo et al. 2001). The

current morphology of the island supposes the presence of three main rifts arranged at 120° from each other (the western rift at 275°, north-eastern rift at 35° and the southern rift at 155°; Carracedo 1996; Gee et al. 2001). The presence and the relative evolution of a three armed rift is still most discussed for the island. Recently Becerril et al. (2015) proposed an important characterization about the structural evolution of El Hierro Island, where the radial structures defined a uniform stress fields during the constructive episodes, that result affected by the combination of gravitational spreading, overburden pressure, stresses induced by magma ascent in each of the volcanic edifices. Conversely, in the shallower parts of the edifice the structures with strikes NE–SW, N–S and WNW–ESE reflect local stress fields related to the formation of giant landslides and able to mask the general and regional fields of stress (Becerril et al. 2015).

The sub-aerial volcanic activity in El Hierro starts at 1.12 Ma, with massive lava flows in the NE of the island (Guillou et al. 1996). The most widely accepted interpretation of El Hierro geology describes three main volcanic cycles, namely Tiñor Edifice (1.12 - 0.88 Ma), Golfo-Las Playas Edifice (0.545 - 0.176 Ma), and Rift Volcanism (0.158 Ma - Present) (Carracedo et al. 2001; IGME 2010a, b, c, d; Becerril et al. 2013a). The cycles are separated by a period of quiescence, structural deformation and sector collapses: four main amphitheatres Las Playas I and II (~545 - 0.176 Ma and 0.176 - 0.145 Ma respectively), El Julan (~0.158 Ma) and the Golfo (~87 - 39 ka) (Masson 1996; Masson et al. 2002; Masson et al. 2006; Gee et al. 2001; Longpré et al. 2011).

A significant variation of the chemical composition is appreciable: from picrite basalts to mafic trachytes. Lavas erupted by Tiñor volcano are characterized by picritic to hawaiitic-tephritic lavas, whereas lavas of the Golfo range from nephelinitic to basanitic to trachytic. Lavas erupted during the last 158 ka (the Rift Volcanism) are mainly alkali picrites and basanites with minor tephrites (Carracedo et al. 2001). The increase in alkalinity is clearly apparent along the entire volcanic history evolution of the island (Stroncik et al. 2009). The last cycle of activity, Rift Volcanism (158 ka - Present), is characterized by emission vents and cinder cones with usually relatively thin layer of basaltic lava flows that covered most of the island. Radiometric age range

from 158 to 2.5 ka and K-Ar ages from 145 to 11 ka (Guillon et al. 1996; Carracedo et al. 2001) indicate that the activity in this late volcanic stage is mainly continuous. However, few radiometric data are available for the Rift Volcanism activity, characterized by much lava thin flows that cover almost the entire topographic surface of El Hierro Island. Over the last 600 years only one submarine eruption was recorded in 2011-2012 in La Restinga area (Lopez et al. 2012; Martí et al. 2013a, b; Longpré et al. 2014).

Methods

The modal composition of ultramafic xenoliths was defined by multicolour image-analysis (ImageJ and Photoshop C5 software), through the reconstruction of the total pixel areas of the single minerals identified in thin sections. A Wavelength Dispersive System (WDS) microprobe has been used for major element composition of mineral phases in peridotites, using double polished thick sections. WDS analyses have been performed with a JEOL JXA 8200 Superprobe, equipped with five wavelength-dispersive spectrometers, Energy Dispersive X-ray spectroscopy (EDS), and cathode luminescence detector at University of Milan (Italy). The operating conditions consist of an acceleration voltage of 15 kV, at a beam current of 15 nA at 30s counting time for element, with a spot size of 1μm. The typical detection limit for each element was 0.01%. Natural and synthetic minerals have been used as standard during the calibration phase of the instrument. Structural formulae of minerals have been processed through the software NORM of Ulmer (1986).

Microthermometric measurements in fluid inclusions have been carried out with a Linkam THMS600 heating/freezing stage and equipped with a Leitz microscope (40× objective) at the University of Milan Bicocca (Italy), which operates in a temperature range between -196 and 600 °C. The instrument has been calibrated using natural and synthetic fluid inclusions (SYN-FLINC) as temperature standards, checking the temperature at the CO_2 and H_2O triple points (-56.6 and 0.1 °C, respectively). In the temperature interval between -90 and 31 °C, an accuracy of ± 0.1 °C has been estimated at the standard reference points, and ± 0.2 °C at other temperatures. The melting

163 temperature (T_m) and the homogenization temperature (T_h) of fluid inclusions have been measured
164 with a heating rates variable from 0.3 to 0.1 °C/min. The density of CO_2 inclusions has been
165 defined by the equation of Duschek et al. (1990), (BULK software; Bakker 2003). Isochores have
166 been calculated using the equation of Holloway (1981), (ISOCHORE software; Bakker 2003). The
167 selected equation is valid up to least 2000 °K and 1.5 GPa. Molar volumes of CO_2–N_2 have been
168 derived by plotting fluid composition determined by Raman spectroscopy and measured sequences
169 of phase transitions in the CO_2–N_2 T-X diagram (van den Kerkhof 1989; Klemd et al. 1992).
170 Isochores for CO_2–N_2 fluid inclusions have been calculated using the equation of Holloway (1977)
171 valid from 373 to 1273 °K and up to 2 GPa, (ISOCHORE software; Bakker 2003), based on relative
172 mole %.

173 Fluid inclusions have been further characterized with the Horiba Labram HR800 Raman
174 microspectrometer, of the Interdepartmental Center "G.Scansetti" at the University of Torino (Italy).
175 A polarized Nd green laser operating at 532 nm wavelength and 80 mW incident power was used as
176 the excitation source, with a spot size resolution of 1×1×3 μm. The slit width was 300 μm, the
177 grating was 600 grooves/mm, and the corresponding spectral resolution was ±1.5 cm^{-1}. Fluid
178 inclusions Raman spectra have been collected with a 100× Olympus objective and 30s acquisition
179 times (3 accumulations per spectrum). The calibration of the instrument has been daily checked,
180 using the 521 cm^{-1} silicon band. The molar fractions (X) of end-member components in a CO_2–N_2
181 mixture, as well as the characterization of daughter and host minerals of fluid inclusions has been
182 made following Frezzotti et al. (2012a). Spectra statistical fitting has been performed with Fityk
183 0.9.8 free analysis software, applying PseudoVoigt functions. The Raman densimeter for pure CO_2
184 fluid inclusions (e.g. Rosso and Bodnar 1995), based on the distance of the CO_2 Fermi doublet (Δ,
185 in cm^{-1}; Wang and Wright 1973; Garrabos et al. 1980) was applied using the equation of Kawakami
186 et al. (2003), with a range of application from 0.1 to 1.24 g/cm^3 with an accuracy better than 5%.
187 Selection of the Raman densimeter equation was performed based on double check (Raman and
188 microthermometry) of densities in 20 fluid inclusions.

Composition and *P-T* equilibration conditions of peridotites

In the island of El Hierro, abundant ultramafic xenoliths are reported from several lava flows and pyroclastic rocks (e.g. Neumann et al. 1991, 2004; Hansteen et al. 1991). For this study xenolith samples have been collected in a locality in the El Julan valley, not sampled before (27°41'27"N - 18°02'49"W) along an abandoned road used for water tunnel investigations. The outcrop consists of a thick and massive basaltic lava flow (Fig. 2a) belonging to the Rift Volcanism phase based on geological maps, attitude of the flow and available radiometric data. About 1 km south-western of the sampled xenolith rich flow Carracedo et al. (2001) present 2 K-Ar radiometric ages (SJ 01 41±2 ka and SJ 02 31±2 ka) related to two lava flows that form a continuous lava flow succession without any important unconformity inside. Therefore, the investigated xenolith rich lava flow belongs to this succession and presents an age between 50 and 30 ky.

Ultramafic xenoliths are from sub-angular to angular in shape and about 10 cm in size on average. They have a pale green colour, characteristic for fresh peridotites. The contours of rocks are sharp, and host lava infiltrations are absent or very limited. Among 35 collected samples, 11 xenoliths have been selected for petrographic and fluid inclusion studies.

Petrography

Studied rocks are type I peridotites: olivine-orthopyroxene-spinel series, following the classification of Frey and Prinz (1978). Ultramafic rocks show variable modal composition (modal composition = %), and consist of 3 dunites (ol 92-94, cpx 1-4, opx 4-6, %; samples XML 1, 5, and 10), 3 lherzolites (ol 63-78, cpx 11-12, opx 11-26, %; samples XML 3, 6, and 8) and 5 harzburgites (ol 59-78, cpx 2-4, opx 18-38, %; samples XML 4, 7, 9, 11, and 12). Most harzburgites and lherzolites show a protogranular texture, with variable recrystallization degrees, generally for 10 to 30 %. Only lherzolite sample (XML 3) shows a porphyroclastic texture (neoblasts > 50 % of the sample).

213 In peridotites, two generations of olivine and orthopyroxene are observed: large and elongated
214 strained grains (porphyroclasts with a size of 4 mm), and smaller polygonal strain-free ones
215 (neoblasts). Olivine porphyroclasts (Ol I) are typically coarse-grained, with several olivine grains
216 having sized up to 25 mm. Olivine porphyroclasts show kink-bands (Fig. 2b), and may contain
217 trails of spinel inclusions. Similar textural characteristics have been also previously reported by
218 Neumann et al. (1991). Orthopyroxene porphyroclasts (Opx I) present different characteristics in
219 peridotites showing variable recrystallization degrees. In less recrystallized protogranular samples,
220 Opx I shows clinopyroxene ± spinel exsolution lamellae (Fig. 2c). In more recrystallized
221 protogranular samples (about 30 %) and in the porphyroclastic one, Opx I generally does not
222 contain exolution lamellae (Fig. 2e), or shows clear rims (Fig. 2d).

223 Olivine and orthopyroxene neoblasts (Ol II and Opx II), with a grain size < 2 mm, are
224 polygonal and strain-free which may include minute spinel grains (Fig. 2f), present as interstitial
225 grains showing frequent triple junctions. In the spinel dunites, neoblasts of olivine (2mm) are
226 concentrated along preferred orientations within the large Ol I deformed grains, showing a rock
227 foliation (Fig. 2h).

228 Clinopyroxene and spinel grains have smaller sizes (1mm), and occur both as subhedral and
229 as interstitial crystals. They may form symplectites with orthopyroxene and olivine. (Fig. 2g).

230 *Mineral chemistry*

231 In spinel harzburgites and lherzolites, Olivine presents a narrow Mg# (Mg# = Mg/Mg+Fe)
232 ranging from 89.3 to 91, with slightly higher values in harzburgites. CaO content varies from 0.01
233 to 0.17 wt%, Al_2O_3 from 0 to 0.05 wt% and NiO from 0.31 to 0.48 wt% (weight percent = wt%).
234 No significant chemical variation between porphyroclasts and neoblasts has been observed, with the
235 exception of higher CaO contents, up to 0.17 wt%, in neoblasts.

236 Orthopyroxene also covers a narrow Mg# interval, from 0.90 to 0.91. Al_2O_3 content ranges
237 from 2.1 to 3.7 wt%, Cr_2O_3 from 0.24 to 0.7 wt% and CaO from 0.36 to 0.81. TiO_2 content is very
238 low (<0.17 wt%).
239 Clinopyroxene is Cr-diopside with Mg# ranging from 0.89 to 0.93. Cr_2O_3 varies from 0.48 to
240 1.1 wt%, Al_2O_3 content varies from 1.68 to 4.55 wt% and TiO_2 from 0 to 1.25 wt%. Spinel is a
241 magnetite–spinel solid-solution with a Cr# [=Cr/ (Cr + Al)] ranging from 0.25 to 0.35. Cr_2O_3 ranges
242 from 20.84 to 28.98 wt% and TiO_2 from 0 to 0.22 wt%. Chromite-rich rims are observed in some
243 grains with a Cr# from 0.4 to 0.5.

244 *P–T equilibration conditions in the lithosphere*

245 Equilibration temperatures for peridotites from El Hierro were estimated considering the
246 partitioning of Fe^{2+}, Mg and Ca between orthopyroxene porphyroclasts and clinopyroxene (Wells
247 1977; We), the two-pyroxene and the Ca-in-opx thermometers (Brey and Koehler 1990; BK2px and
248 BKopx), the solubility of Ca and Al in orthopyroxene in equilibrium with olivine, clinopyroxene
249 and spinel (Witt-Eickschen and Seck 1991; WS). Temperature estimates were performed in
250 exsolved porphyroclasts cores and in clear porphyroclasts and neoblasts of harzburgites and
251 lherzolites.
252 Exsolved orthopyroxene porphyroclasts provide equilibration temperatures comprised
253 between 800 and 950 °C. BK2px provides the lowest equilibration temperatures at 800 °C, while
254 the We and BKopx thermometers provide consistent temperatures, ranging from 800 to 920 °C. WS
255 thermometer provides the higher estimates, with temperatures reaching 950 °C. Clear
256 porphyroclasts thermometry shows higher temperatures, compared to the exsolved crystals
257 thermometry, ranging from 900 to 1100 °C. BK2px provides also in this case the lower estimates
258 with temperatures of approximately 900 °C. We and BK opx thermometers yield to more elevated *T*
259 condition, reaching 980 °C. WS thermometer gives the higher equilibration temperatures, from 950

to 1100 °C. Temperatures estimates in neoblasts show that peridotites from El Hierro have been locally heated to $T > 1100$ °C (We and BK thermometers).

From mineral geothermometry it is possible to distinguish two groups of peridotites: a first group is represented by harzburgites and lherzolites that present exsolved orthopyroxene porphyroclasts, which show equilibration temperature from 800 to 950 °C (LT peridotites; XML 7, 8, 10 and 11). A latter group corresponds to harzburgites and lherzolites that contain clear orthopyroxene porphyroclasts and higher equilibration temperatures from 900 to 1100 °C (HT peridotites; XML 3, 4, 5 and 9). In peridotites from El Hierro and other Canary Islands, this bimodal temperature distribution, in the same temperature intervals, was previously reported (i.e., HEXO and HTR peridotites) by Neumann et al. (2002).

Pressures were estimated employing the Koehler and Brey (1990) geobarometer (KB), which considers the diffusion of calcium in olivine. The minimum equilibration pressures correspond to 1.5 GPa, while the maximum condition reaches pressures of 2 GPa. It has to be noted, however, that the KB barometer is strongly temperature dependent, consequently pressure estimates have to be considered affected by a significant uncertainty.

Fluid inclusion study

Petrography of fluid inclusions

Nine representative peridotite samples LT and HT peridotites have been selected for fluid inclusion studies. Selected samples consist of 3 dunites (XML 1, 5, and 10), 4 harzburgites (XML4, 7, 9 and 11), and 2 lherzolites (XML3 and 9). Fluid inclusions are most abundant in porphyroclasts of LT peridotites. Neoblasts, generally do not contain fluid inclusions. On the basis of textural features, two main fluid inclusion assemblages (Roedder, 1984; Bodnar, 2003) have been recognized.

Early *Type I* inclusions are present only in olivine and exsolved orthopyroxene porphyroclasts of LT peridotites. They have rounded or negative-crystal shapes and occur either in spatially

isolated small clusters and trails, or as short alignments along preferred crystallographic orientations (Fig. 3a, c). *Type I* inclusions are associated with carbonate-rich inclusions and veins (Fig. 3b). The size of these inclusions is in a range from ≤ 3 μm to 50 μm (Fig. 3c, d). At room temperature, *Type I* fluid inclusions are generally single phase (L; Fig. 3c), or they can contain several daughter minerals (Fig. 3a and d; i.e., carbonates, or carbonates + sulphates, ± chlorides ± phosphates), and an opaque mineral (two-phase L + S inclusions). The composition of mineral phases present in some *Type I* fluid inclusions has been determined by Raman microspectroscopy (Fig. 4). Carbonates are dolomite, or Mg-calcite and magnesite; sulphates include anhydrite, sulphalite and $MgSO_4+nH_2O$; phosphate is apatite; the opaque phase is either Cr-spinel, or magnetite, or hematite.

They often show several micro-fractures and are surrounded by haloes of tiny inclusions (1-3 μm) (red arrows in Fig.3d). Similar textures are commonly observed in fluid inclusions in mantle xenoliths and interpreted as evidence for partial decrepitation during magma ascent, due to internal fluid overpressure (e.g., Roedder 1965; Pasteris 1987; De Vivo et al. 1988; Bodnar 2003).

Late *Type II* fluid inclusions are generally present in olivine, orthopyroxene and clinopyroxene, of both LT and HT peridotites. *Type II* inclusions occur both as intragranular and intergranular trails of variable length, and as isolated clusters. (Fig. 5a, c). They have negative-crystal or rounded shapes and sizes ranging from less 1 μm to 25 μm. At room temperature, fluid inclusions are generally single phase CO_2 (L) or, less commonly, two phases (L+V) and do not contain daughter minerals. In exsolved orthopyroxene fluid inclusions are also observed along preferential crystallographic orientations (010) (Fig. 5d). Decrepitation textures are more frequent in inclusions of HT peridotites (Fig. 5b).

Composition and density of trapped fluids

The chemical composition and the density of the fluids preserved in *Type I* and *Type II* inclusions has been determined by microthermometric and Raman microspectroscopic analyses. For analyses, only *Type I* fluid inclusions which do not contain daughter mineral phases have been

selected. Those *Type II* inclusions with a size < 3µm, which cannot be measured by microthermometry method, composition and density have been obtained by Raman microspectroscopy.

***Type I* fluid inclusions**

Phase transitions have been observed in 15 one-phase (L) *Type I* inclusions present in LT peridotites within the range from -190 °C to 20 °C of two LT peridotites. On cooling down, 14 *Type I* inclusions freeze in a temperature range from -95 to -80 °C. On subsequent heating, inclusions show slow melting of solid CO_2 in a 2-3 °C interval with initial melting (T_i) around -60 °C, and final CO_2 melting temperatures (T_m) from -58.6 to -56.9 °C (Fig. 6). Homogenization temperatures to the liquid phase (T_{hL}) are recorded between -52 and 8 °C. According to the classification of Van den Kerkhof (1988), the recorded phase transition (T_i; S+L→S+L+V, T_m; S+L+V→ L+V, T_{hL}; SL+V→L) identifies *H3* type CO_2-rich inclusions containing minor additional CH_4 and/or N_2 species.

A single *Type I* inclusion (~10µm in size, red arrow in Fig. 7a) shows a different microthermometric behaviour. On cooling down to -190 °C, the inclusion does not freeze completely but consists of solid CO_2, coexisting with a liquid and a vapour phase. On heating, 4 subsequent phase transitions are observed: partial homogenization in presence of solid CO_2 (Th_S; S+L+V→S+L) is recorded at about -152 °C; then a small bubble re-appears at about -95 °C (T_i; S+L→S+L+V). On further heating, the partial homogenisation in presence of solid CO_2 (Th_S; S+L+V→S+L) is measured at -61.0 °C. The last phase transition occurs by melting of CO_2 in a one-phase liquid-like fluid (T_s; S+L→L) at -60 °C. According to Van de Kerkhof (1988) and Klemd et al. (1992) the observed sequence of phase transitions (*S4* CO_2-N_2 fluid inclusions = *S4*) is typical of extremely high-density CO_2–N_2 fluids.

The presence of nitrogen has been confirmed in all *Type I* fluid inclusions by Raman microspectroscopy, by the nitrogen band recorded at 2228-2330 cm^{-1} (Fig.7). A N_2 molar fraction (X_{N2}) of 0.18, has been calculated for the *S4* CO_2-N_2 inclusion. The others inclusions (*H3* CO_2-N_2

fluid inclusions) contain less N_2, being X_{N2} comprised between 0.05 and 0.09 (Fig. 7). Once known the molar fraction of N_2, the molar volume of CO_2-N_2 mixtures has been derived by plotting the measured sequences of phase transitions in the CO_2-N_2 T-X diagram of Klemd et al. (1992; Fig. 8). For the *S4* inclusion (X_{N2} = 0.18 and Th_s= -152 °C) the corresponding molar volume is 34.5 cm^3/mol (d = 1.19 g/cm^3). For most *H3* inclusions, molar volumes range from 38.5 cm^3/mol (*H3* with X_{N2}= 0.05 - 0.09 and T_{hL}= -52 and -51 °C), to 40 to 45 cm^3/mol (*H3* with X_{N2}= 0.01 and T_{hL}= -35 and -34 °C). Molar volumes of fluid inclusions with the highest T_{hL} (from 2 to 8°C; X_{N2}= 0.01) are ~50 cm^3/mol.

***Type II* fluid inclusions**

The microthermometric behaviour of *Type II* fluid inclusions has been investigated in both LT and HT peridotites samples. On cooling, the CO_2 fluid inclusions froze in a range of temperature from - 95 to – 65 °C. CO_2 melted instantaneously at temperatures variable from - 57.3 to - 56.5 ± 0.1 °C (n = 50), with most data at -56.6 ±0.1 °C (Fig. 4). This melting behaviour indicates that fluid inclusions consist of pure CO_2, as confirmed by Raman analysis. Liquid water and/or clathrates have not been observed in any of the measured inclusions by both analytical techniques.

Type II CO_2 inclusion homogenization generally occurs to the liquid phase (Th_L). Only the 2% of analysed fluid inclusions shows homogenization to the vapour phase (Th_V). Fig. 9 illustrates the histograms of distribution of measured Th_L (n = 512) by microthermometry. Homogenization temperatures range from -37.5 to +31 ±0.1 °C, with a corresponding CO_2 density range from 1.11 to 0.65 ±0.01 g/cm^3.

The scattered distribution of Th_L values form two frequency maxima occurring at slightly different temperatures in LT and HT peridotites (Fig. 10). In LT peridotites, the two intervals of Th_L maxima are from -37.5 to -12 °C, and from 20 to 31 °C, respectively (Fig. 10a). In HT peridotites, *Type II* fluid inclusions show the first Th_L interval at relatively higher temperatures, from -24 to 0 ± 0.1 °C, while the second Th_L distribution maximum occurs from 20 to 31 ± 0.1 °C (Fig. 10b).

Based on Th_L distribution maxima, CO_2 density values ranges between 1.11 and 1 ± 0.01

362 g/cm^3 and between 0.75 and 0.65 ± 0.01 g/cm^3 in LT peridotites, while in HT peridotites, CO_2
363 density show values between 1.04 and 0.91 ± 0.01 g/cm^3 and between 0.75 and 0.65 ± 0.01 g/cm^3.
364 The consistency of Th_L measurements in *Type II* fluid inclusions has been investigated
365 according to the host mineral phase. As shown by the histograms in Fig. 11, Th_L distributions are
366 comparable for inclusions in orthopyroxene and clinopyroxene. In olivine, *Type II* fluid inclusions
367 show a Th_L distribution at lower temperatures: that is they have lower densities. This suggests that
368 none among the densest CO_2 inclusions in olivine has preserved the original fluid density.
369 To test if partial decrepitation of *Type II* CO_2 inclusions in olivine is dependent on inclusion
370 size (e.g. Bodnar et al. 1989; Campione et al. 2015), the density of 37 inclusions with a size ≤ 3 μm
371 in olivine from LT peridotites has been calculated by the Raman densimeter (Rosso and Bodnar
372 1995). Measured distances of the Fermi doublet (Δ) in CO_2 Raman spectra from 105.17 to 104.46
373 ±0.03 cm^{-1} correspond to CO_2 density ranges between 1.11 to 0.85 ± 0.01g/cm^3 (Fig. 11).

374 ## Discussion

375 ### *Significance of fluid inclusion data*

376 Fluid inclusions in mantle xenoliths represent either metasomatic fluids in the lithosphere,
377 unrelated to xenoliths transport to the surface, or fluids degassed by the ascending magmas during
378 xenolith ejection at the surface (Andersen and Neumann 2001; Hansteen and Klügel 2014; Frezzotti
379 and Touret 2014, and references therein). The densities of metasomatic and magmatic fluids are
380 generally different, since trapping occur at different pressure conditions. Thus, in principle the
381 density distribution of fluid inclusions in mantle xenoliths may provide ample information on the
382 depths of origin of mantle rocks, and on magma ascent dynamics (Andersen and Neumann 2001;
383 Zanon et al. 2003; Frezzotti and Peccerillo 2004; Hansteen and Klügel 2006).
384 At trapping conditions, the pressure of the fluid inside the inclusions equals the lithostatic
385 pressure. During syn-eruptive magma rise, however, the fluid inside the inclusions develops
386 relevant overpressures, since the external lithostatic or magmatic pressure becomes progressively

387 significantly lower than fluid internal pressure governed by the fluid equation of state (Roedder
388 1984). If fluid overpressure exceeds the mechanical strength of the enclosing mineral, fluid
389 inclusions undergo decrepitation and/or stretching, with partial-to-complete fluid loss, and/or an
390 increase of the inclusion volume, resulting in a decrease of fluid density. Decrepitation of fluid
391 inclusions is a complex process that depends on a number of variables, such as the composition,
392 size, and distribution of the fluid inclusions, and the mechanical strength of the host mineral (e.g.,
393 Bodnar et al. 1989; Vityk and Bodnar 1998; Campione et al. 2015), but it generally does not reflect
394 a decrease of magma decompression rates. Only if decrepitation and/or stretching reset fluid
395 inclusion densities to a newly defined, low-pressure interval, and/or novel episodes of fluid trapping
396 occur, a slowing down in the ascent rate of magmas can be proposed, which corresponds to magma
397 rest episodes at confined depths (Frezzotti and Peccerillo, 2004).

398 In El Hierro mantle xenoliths, the petrographic study of fluid inclusions shows trapping of
399 distinct fluids in subsequent events. Early *Type I* fluid inclusions represent the earliest fluids, as
400 indicated by their distribution as small clusters or as crystallographically oriented groups in olivine
401 and orthopyroxene porphyroclasts which are preserved only in LT peridotites. *Type I* fluids are
402 CO_2-rich and contain variable amounts of N_2; the highest N_2 content of 18 mole % is recorded in
403 the highest (1.19 g/cm^3) density inclusions. Their association with CO_2-rich ($\pm N_2$) inclusions,
404 containing carbonates, sulphates, ± chlorides and spinel, and with carbonate-silicate glass micro-
405 veins suggest formation of *Type I* CO_2-N_2 fluids by immiscibility processes from an original
406 carbonate-sulphate-rich silicate melt. The chemical nature of *Type I* fluids, associated with their
407 extremely high density, suggest a deep metasomatic origin in the mantle lithosphere (Villa et al.
408 submitted). Invasion of metasomatic fluids cannot occur during the ascent of xenoliths but testify
409 evolution of peridotites at mantle conditions.

410 The chemical composition of metasomatic fluids described by present study in El Hierro
411 peridotites, is in agreement with previous studies on mantle peridotites from the Canary Islands.
412 CO_2-N_2 lithospheric fluids were previously reported in peridotites from Lanzarote (Andersen et al.

413 1995). Presence of N_2 in CO_2 inclusions was also in this case revealed by combining
414 microthermometry with Raman microspectroscopy, the latter one being the only analytical
415 technique able to detect a few mole % N_2 in CO_2-rich inclusions of small size. Further, evidence for
416 carbonate metasomatism was previously reported in peridotites from Tenerife, Lanzarote, and La
417 Gomera islands (Frezzotti et al. 1994; 2002a; 2002b; Neumann et al. 1995; 2002; 2004).

418 At a later stage, ingression of pure CO_2 fluids in both LT and HT peridotites is testified by
419 *Type II* fluid inclusions. Their distribution along intergranular trails is suggestive of fluid trapping
420 events during micro-fracturing of host rocks. The clear-cut variation of chemistry of *Type II* fluids,
421 which consist of pure CO_2, suggests a different origin, probably by degassing in basaltic magmas.

422 *Type II* fluid inclusion Th_L frequency intervals show two density intervals that should be
423 discussed separately. The presence of these suggests two distinct events of fluid trapping and/or re-
424 equilibration (Fig. 10). In rocks equilibrated at lower temperatures comprised between 800 and 950
425 °C (LT peridotites), frequency maxima between -37.5 and -12 ± 0.1 °C, and between 20 and 31 ±
426 0.1 °C (Fig. 10a), correspond to density intervals from 1.11 to 0.99 ± 0.01 g/cm^3 and from 0.75 to
427 0.65 ± 0.01 g/cm^3, respectively (Fig. 12a). Density values calculated applying the "Raman
428 densimeter" in *Type II* fluid inclusions in olivine with a size ≤ 3μm are in the range between 1.11 to
429 0.85 ± 0.01 g/cm^3 (Kawakami et al. 2003), (Fig. 12a). This density interval is similar to that
430 obtained in larger CO_2 inclusions in orthopyroxene and clinopyroxene (Fig. 11), suggesting that
431 olivine is less resistant than pyroxenes to mechanical failure.

432 In peridotites equilibrated at higher temperatures (900-1100 °C; HT peridotites), the two Th_L
433 distribution maxima for *Type II* fluid inclusions are from -24 to 0 ±0.1 °C, and from 20 to 31 ± 0.1
434 °C (Fig. 10b), corresponding to densities from 1.04 to 0.91 ± 0.01 g/cm^3 and from 0.75 to 0.65 ±
435 0.01 g/cm^3, respectively. Interestingly, CO_2 fluids in HT peridotites systematically show slightly
436 lower density values (Fig. 12b). A similar CO_2 density distribution pattern between peridotites
437 equilibrated at high and low temperatures was previously recognized at El Hierro and Tenerife by

438 Hansteen et al. (1998). These authors interpreted the decrease of density in fluids of HT peridotites
439 as the result of isobaric heating at depth.
440 Once the composition and density of the fluids have been defined, the temperature of fluid
441 trapping should be known in order to define the pressure of fluid trapping conditions (Roedder
442 1965;1984). Fluid trapping temperatures have been assumed based on equilibration temperatures
443 between 800 and 950 °C in LT peridotites, and between 900 and 1100 °C in HT peridotites (mineral
444 geothermometry by Wells 1977, Brey and Koehler 1990 and Witt-Eickschen and Seck 1991). From
445 each interval, the highest temperature value has been selected as representative for fluid trapping
446 conditions, assuming the presence of a component of increasing temperature caused by the ascent of
447 mantle xenoliths in the basaltic host lavas.
448 The extremely high density of *Type I* fluids in LT peridotites (1.19g/cm^3; inclusion *S4)*,
449 correspond to pressure conditions of 1.8 ± 0.02 GPa at 950 °C (grey star in Fig. 13) and can be
450 considered as representative of equilibration conditions in the lithosphere. Calculated pressures are
451 in agreement with those independently defined by mineral geobarometry, which are comprised
452 between 1.5 and 2.0 ± 0.02 GPa (Koehler and Brey 1990), at the same temperature of 950 °C.
453 At lower pressures, trapping and/or re-equilibration of CO_2 fluids in both LT and HT
454 peridotites occurred during two distinct episodes of magma rest during xenolith's ascent in the host
455 basaltic lavas (Fig. 13). Fluxes of CO_2 probably originated by magma degassing episodes. Since
456 petrological studies indicate that peridotites, which are host for fluid inclusions, record different
457 temperature conditions, fluid density data in LT and HT rocks will be treated separately.
458 In LT peridotites, densities of *Type II* inclusions between 1.11 to 0.99 ± 0.01 g/cm^3
459 correspond to pressures from 1 to 0.67 ± 0.02 GPa, at 950 °C. In HT peridotite samples, fluid
460 densities between 1.04 to 0.91 ± 0.01 g/cm^3 correspond to somewhat lower pressure conditions from
461 0.89 to 0.6 ± 0.02 GPa, at 1100 °C. As illustrated in the P-T diagram in Fig. 13, the almost complete
462 overlap of pressure intervals defined by isochores for *Type II* CO_2 fluids at different temperatures
463 allows us to consider both types of inclusions as representative for a single deep CO_2 trapping

episode. The slightly higher pressure conditions recorded by fluids in LT rocks (Fig. 13) suggest that fluid inclusions are better preserved in LT peridotites.

A second CO_2 trapping event or re-equilibration (Fig. 13) is recorded by *Type II* fluid inclusion densities between 0.75 and 0.65 g/cm^3 that correspond to an interval of pressures from 0.34 to 0.26 ± 0.02 GPa at 950 °C (LT peridotites) and from 0.36 to 0.28 ± 0.02 GPa at 1100 °C (HT peridotites). The values obtained differ from each other of 0.02 GPa, a negligible pressure variation conform to the accuracy of pressure estimates. This event corresponds to the last fluid trapping episode prior to eruption.

The magma plumbing system beneath El Hierro Island

In order to describe magma ascent dynamics based on fluid inclusion studies in peridotite xenoliths of El Julan, once having found the *P-T* conditions of for *Type I* and *Type II* fluids, we have to define the corresponding depths. Pressure conditions have been converted into depths, following the relation: ***H= P/(g*d)***, where **H** is the depth of origin or trapping of the fluids, **P** the lithostatic pressure, **g** the acceleration of gravity (9.81 m/sec^2), and **d** the density of column-rocks. Rock densities have been defined based on the following simplified stratigraphic reconstruction: a sequence of volcanic products and rocks with a density of 2.5 g/cm^3 has been considered for the entire volcanic edifice (emergent and submarine height of island of about 4500 m; Acosta et al. 2005; Carracedo et al. 2012), a basaltic oceanic crust with a density of 2.7 g/cm^3 (about 8500 m), and a mantle lithosphere with a density of 3 g/cm^3. The Moho beneath El Hierro island has been assumed between at about 12.5-15 km from geophysical data (Martinez et al. 2013).

Fluid inclusions and petrological studies suggest a multistage magma ascent from a depth of about 60 km till the Earth's surface for the Rift Volcanism activity of El Hierro volcano at about 50 ka. The resulting model is illustrated schematically in Fig. 14 and discussed in the following sections.

488 The densest among *Type I* CO_2-N_2 mantle metasomatic fluids suggests 60 km as the minimum
489 equilibration depth in the lithosphere for LT peridotites (grey star in Fig. 14; P = 1.8 ± 0.02 GPa).
490 Fluid inclusion data are in agreement with 70 to 50 km calculated by mineral geothermobarometry
491 of peridotites. Calculated pressures represent the minimum depths of origin of mantle rocks in the
492 deep oceanic lithosphere. Noteworthy, similar depths are the highest ever recorded by fluid
493 inclusions in mantle xenoliths from the Canary Islands.
494 *Type II* CO_2 fluids were trapped after the withdrawal of peridotites by the rising basaltic
495 magma and record ascent dynamics to shallower conditions through the mantle and the crust.
496 Geothermobarometric studies of Type II inclusions in both peridotite groups clearly identify two
497 main magma accumulation regions (Fig. 14): the first one from 36 to 22 km (P = 1 - 0.67 ± 0.02
498 GPa), and the latter one from 12 to 10 km (P = 0.34 - 0.21± 0.02 GPa).
499 The first magma reservoir is identified in the lithospheric mantle from 36 to 22 km (Fig. 14).
500 This region, where magma accumulates forming a partially molten magma reservoir, is particularly
501 thick (14 km), suggesting that magma is likely to be stored in a series of vertically interconnected
502 pockets distributed over a wide depth interval (Fig. 14). Magma accumulation in the lithospheric
503 mantle as vertically-stacked small magma reservoirs has been previously characterized for Kilauea
504 and Piton de la Fournaise (Decker 1987; Ryanet al. 1988; de Voogd et al. 1999; Michon et al.
505 2015). Deep ascent dynamics has been interpreted as the result of magma migration either through a
506 micro-fracture network system over a wide depth interval at high pressures (e.g. magma-fracking by
507 CO_2 degassing; Shaw et al. 1980; Pollard et al. 1983; Decker 1987), or in a porous mantle matrix
508 (Gudmundsson 1987). Similar reservoirs are considered to be long-lived (Shaw et al. 1980; Pollard
509 et al. 1983; Decker 1987), and although their formation is still not unanimously accepted, they
510 could be related to slow magma ascent (e.g. Shaw et al. 1980), which would be in agreement with
511 the long-term magma supply rate of El Hierro Island (0.12-0.36 km^3/ka; Carracedo 1999).
512 This mantle magma accumulation region fed the shallower reservoir in the lower crust (12 to
513 10 km; P = 0.34 to 0.21 GPa) from where basalts erupted. This shallower reservoir appears to be

514 temporary, since the preservation of several high-density fluid inclusions in all studied samples
515 suggests a relatively "short" residence time in the lower crust, probably in the timescale of hours or
516 days (Wanamaker and Evans 1989; Hansteen and Klügel et. al. 2008). Longer magma stagnation
517 should have caused a complete resetting of fluid densities to these new ambient pressures.

518 Present model for recent Rift Volcanic activity at El Hierro shares several similarities with the
519 magma ascent dynamics proposed for the 2011-2012 eruption (Meletlidis et al. 2012; Becerill et al.
520 2013b; González et al., 2013; Marti et al. 2013; Longpré et al. 2014; Klügel et al. 2015), suggesting
521 that the magma plumbing system has not changed during last 40 ka. In first place, the two main
522 magma accumulation levels, one in the lower oceanic crust and one in the lithospheric mantle, are
523 located at comparable depths. In addition, the deep-seated lithospheric reservoir (25 and 20 km
524 depth for the 2011-2012 eruption; Marti et al. 2013; Longpré et al. 2014), is also proposed to fed the
525 magma reservoir in the lower crust. Residence of magma in the lower oceanic crust (from 14 to 5
526 km) is likewise considered ephemeral, not developing into a long-term reservoir (e.g. Becerill et al.
527 2013b; Longpré et al. 2014; Marti et al. 2013; Klügel et al. 2015). These authors interpreted the pre-
528 eruptive sub-horizontal magma migration of about 15–20 km as evidence of sill propagation.

529 The reconstruction of the dynamics of magma ascent in active volcanoes through time can
530 help in the investigation of the cause that produce different magma emission rates during eruptions,
531 one of the most important information applicable to the volcanic hazard and risk mitigation
532 eruptions. One main result from present study is that it resolves the geometries of the magma
533 storage system in the lithospheric mantle. The proposed plexus of small interconnected magma
534 pockets, from depths of 36 km extending to about 22 km, is in the same interval of depths (20-25
535 km) evidenced by geophysical data during the 2011-2012 eruption (Martì et al. 2013a, b). Since
536 earthquakes are generally recorded at the top of magma reservoirs, and/or mark the ascent of
537 magma from deeper to the shallower reservoirs, it might be tentatively proposed that diffuse micro-
538 fracture network magma storage and migration system in the lithospheric mantle also governs
539 present magma dynamics.

Summary and conclusions

The major objective of this study was the reconstruction of the recent (40 ka) magma dynamics beneath El Hierro Island, based on combined fluid inclusion and petrological investigations in mantle xenoliths in basaltic lavas of the Rift Volcanism activity. In peridotites, two distinct fluid phases have been identified and characterized by microthermometry and Raman microspectroscopy. Earlier metasomatic fluids are CO_2-N_2 (*Type I* fluid) trapped at pressure conditions of 1.8 ± 0.02 GPa, or 60 km in depth, prior to xenolith uptake by host lava. Two shallower trapping events of CO_2 degassed from basaltic magmas (*Type II* fluids) are recorded in peridotites; the first at pressures from 1 to 0.6 ± 0.02 GPa, or 36 to 22 km in depth, in the lithospheric mantle, and the latter from 0.34 to 0.21± 0.02 GPa, or 10 to 12 km depth in the lower oceanic crust. The deeper accumulation region is interpreted as a vertically staked system of small magma reservoirs distributed in the lithospheric mantle beneath the Island. Our observations are consistent with a deep magma source beneath El Hierro volcano, in agreement with the previous models for last eruption in 2011-2012. Finally, present paper demonstrates the potentiality to study the geometries of deep magma reservoirs by fluid inclusion studies in peridotites, when combined with detailed petrological investigations of rocks.

Acknowledgements

This paper is a part of E.O. Ph.D. thesis. We are grateful to M. Campione and N. Malaspina for helpful discussions. Funding was provided by the University of Milan Bicocca, FAR -2015 to M.L.F and I.M.V. Raman facilities were provided by the Interdepartmental Center “G. Scansetti” for studies on asbestos and other toxic particulates at the University of Turin.

References

Abu El-Rus MA, Neumann ER, Peters V (2006) Serpentinization and dehydration in the upper mantle beneath Fuerteventura (eastern Canary Islands): Evidence from mantle xenoliths. Lithos 89:24–46. http://doi.org/10.1016/j.lithos.2005.09.005

Acosta J, Uchupi E, Muñoz A, Herranz P, Palomo C, Ballesteros M, Working ZE (2005) Geologic evolution of the Canarian Islands of Lanzarote, Fuerteventura, Gran Canaria and La Gomera and comparison of landslides at these islands with those at Tenerife, La Palma and El Hierro. Mar Geophys Res 24:1–40. http://doi.org/10.1007/s11001-004-1513-3

Amelung F, Day S (2002) InSAR observations of the 1995 Fogo, Cape Verde, eruption: implications for the effects of collapse events upon island volcanoes. Geophys Res Lett 29:12. http://dx.doi.org/10.1029/2001GL013760.

Andersen T, Burke EJ, Neumann ER (1995) Nitrogen-rich fluid in the upper mantle: fluid inclusions in spinel dunite from Lanzarote, Canary Islands. Contrib Mineral Petr 120:20–28. http://doi.org/10.1007/BF00311005

Andersen T, Neumann ER (2001) Fluid inclusions in mantle xenoliths. Lithos 55:301–320. http://doi.org/10.1016/S0024-4937(00)00049-9

Anguita F, Hernan F (1975) A propagating fracture model versus a hot spot origin for the Canary Islands. Earth Planet Sci Lett 27:11–19. http://doi.org/10.1016/0012- 821X(75)90155-7

Anguita F, Hernán F (2000) The Canary Islands origin: a unifying model. J Volcanol and Geother Res 103:1–26. http://doi/10.1016/S0377- 0273(00)00195- 5

Bakker RJ (2003) PackageFLUIDS1. Computer programs for analysis of fluid inclusion data and for modelling bulk fluid properties. Chem Geol 194:3–23

Becerril L, Cappello A, Galindo I, Neri M, Del Negro C (2013a) Spatial probability distribution of future volcanic eruptions at El Hierro Island (Canary Islands, Spain). J Volcanol and Geother Res 257:21–30. http://doi.org/10.1016/j.jvolgeores.2013.03.005

Becerril L, Galindo I, Gudmundsson A, Morales JM (2013b) Depth of origin of magma in eruptions. Sci Rep 3:1–6. http://doi.org/10.1038/srep02762

Becerril L, Galindo I, Martí J, Gudmundsson A (2015) Three-armed rifts or masked radial pattern of eruptive fissures? The intriguing case of El Hierro volcano (Canary Islands). Tectonophysics 647:33–47. http://doi.org/10.1016/j.tecto.2015.02.006

Belkin HE, De Vivo B (1993) Fluid inclusion studies of ejected nodules from plinian eruptions of Mt. Somma-Vesuvius. J Volcanol and Geother Res 58:89–100. http://doi.org/10.1016/0377-0273(93)90103-X

Bertagnini A, Métrich NN, Francalanci L, Landi P, Tommasini SC (2002) Volcanology and magma geochemistry of the present-day activity: constraints on the feeding system. In: Calvari S, Inguaggiato S, Puglisi G, Ripepe M. (Eds.), Amer Geophys Union 19-37

Bodnar RJ (2003) Introduction to aqueous-electrolyte fluid inclusions. Fluid Inclusions: Analysis and Interpretation. Mineral Canada, short course 32:81-100

Bodnar RJ, Binns PR, Hall DL (1989) Synthetic fluid inclusions-VI. Quantitative evaluation of the decrepitation behaviour of fluid inclusions in quartz at one atmosphere confining pressure. J Metamorphic Geol 7:229–242

Bonelli R, Frezzotti ML, Zanon V, Peccerillo A (2004) Evolution of the volcanic plumbing system of Alicudi (Aeolian Islands): Evidence from fluid inclusions in quartz xenoliths. Annuals Geophysic 47:1409–1422

Brey GP, Köhler T (1990) Geothermobarometry in four-phase lherzolites II. New thermobarometers, and practical assessment of existing thermobarometers. J Petrology31:1353–1378

Campione M, Malaspina N, Frezzotti ML (2015) Threshold size for fluid inclusion decrepitation. J Geophys Res Solid Earth 120:7396–7402

612 Carracedo JC (1994). The Canary Islands: an example of structural control on the growth of large
613 ocean-island volcanoes. J Volcanol and Geother Res 60:225–241. http://doi.org/10.1016/0377-
614 0273(94)90053-1
615 Carracedo JC (1999) Growth, structure, instability and collapse of Canarian volcanoes and
616 comparisons with Hawaiian volcanoes. J Volcanol and Geother Res 94:1–19.
617 http://doi.org/10.1016/S0377-0273(99)00095-5
618 Carracedo JC, Badiola ER, Guillou H, de La Nuez J, Pérez Torrado FJ (2001) Geology and
619 volcanology of La Palma and El Hierro (Canary Islands). Estudios Geol 57:175–273.
620 Carracedo JC, Perez-Torrado FJ, Rodriguez-Gonzalez A, Fernandez-Turiel JL, Klügel A, Troll, VR,
621 Wiesmaier S (2012) The ongoing volcanic eruption of El Hierro, Canary Islands. Eos 93: 89–
622 90. http://doi.org/10.1029/2012EO090002
623 Collier JS, Henstock TJ, Peirce C, Watts AB, (1998) A detailed geophysical study in the Canary
624 Basin (eastern Atlantic): implications for the internal structure of 130 Ma oceanic crust.
625 Geophys J Int 135:943–963
626 De Vivo B, Frezzotti ML, Lima A, Trigila R (1988) Spinel lherzolite nodules from Oahu Island
627 (Hawaii): a fluid inclusion study. Bull Min 111:307–319
628 Decker RW, Wright TL, Stauffer, S (1987). Volcanism in Hawaii US Government Printing Office
629 pp1606
630 Di Martino C, Frezzotti ML, Lucchi F, Peccerillo A, Tranne C, Diamond LW (2010) Magma
631 storage and ascent at Lipari Island (Aeolian archipelago, Southern Italy) at 223-81 ka: The role
632 of crustal processes and tectonic influence. Bull Vulcanol 72:1061–1076.
633 http://doi.org/10.1007/s00445-010-0383-6
634 Duggen S, Hoernle K, Hauff F, Klügel, A, Bouabdellah M, Thirlwall MF (2009) Flow of Canary
635 mantle plume material through a subcontinental lithospheric corridor beneath Africa to the
636 Mediterranean. Geology 37:283–286. http://doi.org/10.1130/G25426A.1
637 Duschek W, Kleinrahm R, Wagner W (1990) Measurement and correlation of the (pressure,
638 density, temperature) relation of carbon dioxide I. The homogeneous gas and liquid regions in
639 the temperature range from 217 K to 340 K at pressures up to 9 MPa. J Chem Ther 22:827–
640 840. http://doi.org/10.1016/0021-9614(90)90172-M
641 Fall A, Tattitch B, Bodnar RJ (2011) Combined microthermometric and Raman spectroscopic
642 technique to determine the salinity of H_2O-CO_2-NaCl fluid inclusions based on clathrate
643 melting. Geochim Cosmochim Ac 75: 951–964. http://doi.org/10.1016/j.gca.2010.11.021
644 Frey FA, Prinz M (1978) Ultramafic inclusions from San Carlos, Arizona: petrologic and
645 geochemical data bearing on their petrogenesis. Earth Planet Sci Lett 38:129–176
646 Frezzotti ML, Touret JL, Lustenhouwer WJ, Neumann ER (1994) Melt and fluid inclusions in
647 dunite xenoliths from La Gomera, Canary Islands: tracking the mantle metasomatic fluids.
648 Europ J Mineral 6:805–817
649 Frezzotti ML, Andersen T, Neumann ER, Simonsen SL (2002a) Carbonatite melt–CO_2 fluid
650 inclusions in mantle xenoliths from Tenerife, Canary Islands: a story of trapping, immiscibility
651 and fluid–rock interaction in the upper mantle. Lithos 64:77–96. http://doi.org/10.1016/S0024-
652 4937(02)00178-0
653 Frezzotti ML, Touret JL, Neumann ER (2002b) Ephemeral carbonate melts in the upper mantle.
654 Europ J Mineral 14:891–904.
655 Frezzotti ML, Peccerillo A (2004a) Fluid inclusion and petrological studies elucidate reconstruction
656 of magma conduits. Eos 85:157–160 http://doi.org/10.1029/2004EO160001
657 Frezzotti ML, Peccerillo A, Zanon V, Nikogosian I (2004b) Silica-rich melts in quartz xenoliths
658 from Vulcano Island and their bearing on processes of crustal anatexis and crust–magma
659 interaction beneath the Aeolian Arc, Southern Italy. J Petrol 45:3–26
660 Frezzotti ML, Tecce F, Casagli A (2012) Raman spectroscopy for fluid inclusion analysis. J
661 Geochem Explor 112:1–20. http://doi.org/10.1016/j.gexplo.2011.09.009
662

Füster J, Paez A, Sagredo J (1969) Significance of Basic and Ultramafic Rock Inclusions in the Basalts of Canary Islands. Bull Vulcanol 33:665–693

Garrabos Y, Tufeu R, Le Neindre B, Zalczer G, Beysens D (1980) Rayleigh and Raman scattering near the critical point of carbon dioxide. J Chem Physics 72:4637–4651

Gee MJR, Masson DG, Watts AB, Mitchell NC (2001) Offshore continuation of volcanic rift zones, El Hierro, Canary Islands. J Volcanol and Geother Res 105:107–119. http://doi.org/10.1016/S0377- 0273(00)00241-9

Geyer A, Martí J (2010) Tectonophysics The distribution of basaltic volcanism on Tenerife, Canary Islands: Implications on the origin and dynamics of the rift systems. Tectonophysics 483: 310–326. http://doi.org/10.1016/j.tecto.2009.11.002

González PJ, Samsonov SV, Pepe S, Tiampo KF, Tizzani P, Casu F, Sansosti E (2013) Magma storage and migration associated with the 2011 – 2012 El Hierro eruption: Implications for crustal magmatic systems at oceanic island volcanoes, J Geoph Res Solid Earth 118:4361–4377. doi:10.1002/jgrb.50289, 2013

Gudmundsson A (1987) Geometry, formation and development of tectonic fractures on the Reykjanes Peninsula, southwest Iceland. Tectonophysics 139: 295–308

Gudmundsson A (2006) How local stresses control magma-chamber ruptures, dyke injections, and eruptions in composite volcanoes. Earth Sci Rev 79:1–31

Guillou H, Carracedo JC, Torrado FP, Badiola ER (1996) K-Ar ages and magnetic stratigraphy of a hotspot-induced, fast grown oceanic island: El Hierro, Canary Islands. J Volcanol and Geother Res 73:141–155. http://doi.org/10.1016/0377-0273(96)00021-2

Hansteen TH, Andersen T, Neumann ER, Jelsma H (1991) Fluid and silicate glass inclusions in ultramafic and mafic xenoliths from Hierro, Canary Islands: implications for mantle metasomatism. Contrib Mineral Petrol 107:242–254

Hansteen TH, Klügel A, Schmincke HU (1998) Multi-stage magma ascent beneath the Canary Islands: evidence from fluid inclusions. Contrib Mineral Petrol 132:48–64. http://doi.org/10.1007/s004100050404

Hansteen TH, Klügel A, (2008) Fluid inclusion thermobarometry as a tracer for magmatic processes. In: Putirka KD, Tepley FJ Reviews in Mineralogy Min Soc Amer 149:143–177

Hildner E, Klügel A, Hauff F, (2011) Magma storage and ascent during the 1995 eruption of Fogo, Cape Verde Archipelago. Contrib Mineral Petrol 162:751–772.

Hoernle K, Schmincke HU (1992). The Role of Partial Melting in the 15-Ma Geochemical Evolution of Gran Canada: A Blob Model for the Canary Hotspot, J Petrology 34:599–626

Holm PM, Grandvuinet T, Friis J, Wilson JR, Barker AK, Plesner S (2008) An 40Ar-39Ar study of the Cape Verde hot spot: Temporal evolution in a semi-stationary plate environment. Journal of Geophysical Research: Solid Earth 113 http://doi.org/10.1029/2007JB005339

IGME (2010a) Mapa Geológico de España, Escala 1:25.000. Isla de El Hierro. Hoja 1105- II, Valverde, 96 pp

IGME (2010b) Mapa Geológico de España, Escala 1:25.000. Isla de El Hierro. Hoja 1105- III, Sabinosa, 71 pp

IGME (2010c) Mapa Geológico de España, Escala 1:25.000. Isla de El Hierro. Hoja 1105- IV, Frontera, 84 pp.

IGME (2010d) Mapa Geológico de España, Escala 1:25.000. Isla de El Hierro. Hoja 1108- I/II, La Restinga, 55 pp

Kawakami Y, Yamamoto J, Kagi H (2003) Micro-Raman Densimeter for CO_2 Inclusions in Mantle-Derived Minerals. Applied Spectrosc 57:1333–1339

Klemd R, Van den Kerkhof, AM, Horn EE (1992) High-density CO_2− N_2 inclusions in eclogite-facies metasediments of the Münchberg gneiss complex, SE Germany. Contrib Mineral Petrol 111:409–419

712 Klügel A, Hansteen TH, Galipp K (2005) Magma storage and underplating beneath Cumbre Vieja
713 volcano, La Palma (Canary Islands). Earth Planet Sci Lett 236:211–226.
714 http://doi.org/10.1016/j.epsl.2005.04.006
715 Klügel A, Longpré MA, García-Cañada L, Stix J, (2015) Deep intrusions, lateral magma transport
716 and related uplift at ocean island volcanoes. Earth Planet Sci Lett 43:140–149.
717 http://doi.org/10.1016/j.epsl.2015.09.031
718 Koehler TP, Brey GP, (1990) Calcium exchange between olivine and clinopyroxene calibrated as a
719 geothermobarometer for natural peridotites from 2 to 60 kb with applications. Geochim
720 Cosmochim Ac 54:2375–2388
721 Longpré MA, Chadwick JP, Wijbrans J, Iping R (2011) Age of the El Golfo debris avalanche, El
722 Hierro (Canary Islands): New constraints from laser and furnace 40Ar/ 39Ar dating. J Volcanol
723 and Geother Res 203:76–80. http://doi.org/10.1016/j.jvolgeores.2011.04.002
724 Longpré MA, Klügel A, Diehl A, Stix J (2014) Mixing in mantle magma reservoirs prior to and
725 during the 2011 – 2012 eruption at El Hierro, Canary Islands. Geology, 42:315–318
726 http://doi.org/10.1130/G35165.1
727 Marinoni LB, Pasquaré G (1994) Tectonic evolution of the emergent part of a volcanic ocean
728 island: Lanzarote, Canary Islands. Tectonophysics 239:111–137. http://doi.org/10.1016/0040-
729 1951(94)90110-4
730 Marinoni LB, Gudmundsson A (2000) Dykes, faults and palaeostresses in the Teno and Anaga
731 massifs of Tenerife (Canary Islands). J Volcanol and Geother Res 103:83–103
732 http://doi.org/10.1016/S0377- 0273(00)00217-1
733 Martí J, Pinel V, Lõpez C, Geyer A, Abella R, Tárraga M, Rodríguez C (2013a) Causes and
734 mechanisms of the 2011-2012 El Hierro (Canary Islands) submarine eruption. J Geophy Res
735 Solid Earth, 118:823–839. http://doi.org/10.1002/jgrb.50087
736 Martí J, Castro A, Rodríguez C, Costa F, Carrasquilla S, Pedreira R, Bolos X (2013b) Correlation
737 of magma evolution and geophysical monitoring during the 2011-2012 El Hierro (Canary
738 Islands) submarine eruption. J Petrology, 54:1349–1373.
739 http://doi.org/10.1093/petrology/egt014
740 Martinez-Arevalo C, Mancilla FD, Helffrich G, Garcia A (2013) Seismic evidence of a regional
741 sublithospheric low velocity layer beneath the Canary Islands. Tectonophysics 608:586–599.
742 http://doi.org/10.1016/j.tecto.2013.08.021
743 Masson DG (1996) Catastrophic collapse of the volcanic island of Hierro 15 ka ago and the history
744 of landslides in the Canary Islands. Geology 24: 231–234. http://doi.org/10.1130/0091-
745 7613(1996)024<0231:CCOTVI>2.3.CO;2
746 Masson DG, Watts B, Gee MJR, Urgeles R, Mitchell NC, Le Bas TP, Canals M. (2002) Slope
747 failures on the flanks of the western Canary Islands. Earth Sci Rev 57:1–35.
748 http://doi.org/10.1016/S0012-8252(01)00069-1
749 Masson DG, Harbitz CB, Wynn RB, Pedersen G, Løvholt F (2006) Submarine landslides:
750 processes, triggers and hazard prediction. Philosophical Transactions. Series A, Math, Physical
751 Eng Sci 364:2009–2039
752 Meletlidis S, Roberto A, Di Pompilio M, Bertagnini A, Iribarren I, Felpeto A, Oriano CD (2012)
753 Xenopumices from the 2011 – 2012 submarine eruption of El Hierro (Canary Islands, Spain):
754 Constraints on the plumbing system and magma ascent, Geophy Res Let 39:1–6.
755 http://doi.org/10.1029/2012GL052675
756 Menand T (2011) Physical controls and depth of emplacement of igneous bodies: a review.
757 Tectonophysics 500:11–19
758 Michon L, Ferrazzini V, Di Muro A, Villeneuve N, Famin V (2015) Rift zones and magma
759 plumbing system of Piton de la Fournaise volcano: How do they differ from Hawaii and Etna?
760 J Volcanol and Geother Res 303:112–129. http://doi.org/10.1016/j.jvolgeores.2015.07.031
761 Morgan DJ, Jerram DA, Chertkoff DG, Davidson JP, Pearson DG, Kronz A, Nowell GM (2007)
762 Combining CSD and isotopic microanalysis: Magma supply and mixing processes at Stromboli

763 Volcano, Aeolian Islands, Italy. Earth Planet Sci Lett 260:419–431
764 http://doi.org/10.1016/j.epsl.2007.05.037
765 Neumann E (1990) Ultramafic and mafic xenoliths from Hierro, Canary Islands: evidence for melt
766 infiltration in the upper mantle. J Chem 53:1689–1699.
767 http://doi.org/10.1017/CBO9781107415324.004
768 Neumann ER, Wulff-Pedersen E, Johnsen K, Andersen T, Krogh E (1995) Petrogenesis of spinel
769 harzburgite and dunite suite xenoliths from Lanzarote, eastern Canary Islands: Implications for
770 the upper mantle. Lithos 35:83–107. http://doi.org/10.1016/0024-4937(95)91153-Z
771 Neumann ER, Wulff-Pedersen E, Pearson NJ, Spencer EA (2002) Mantle Xenoliths from Tenerife
772 (Canary Islands): Evidence for Reactions between Mantle Peridotites and Silicic Carbonatite
773 Melts inducing Ca Metasomatism. J Petrology 43:825–857.
774 http://doi.org/10.1093/petrology/43.5.825
775 Neumann ER, Griffin WL, Pearson NJ, O'Reilly SY (2004) The evolution of the upper mantle
776 beneath the Canary Islands: Information from trace elements and Sr isotope ratios in minerals
777 in mantle xenoliths. J Petrology 45: 2573–2612. http://doi.org/10.1093/petrology/egh063
778 Nimis P, Taylor WR (2000) Single clinopyroxene thermobarometry for garnet peridotites. Part I.
779 Calibration and testing of a Cr-in-Cpx barometer and an enstatite-in-Cpx thermometer. Contrib
780 Mineral Petrol 139:541–554. http://doi.org/10.1007/s004100000156
781 Pasteris JD, Wopenka B, Seitz JC (1988) Practical aspects of quantitative laser Raman microprobe
782 spectroscopy for the study of fluid inclusions. Geochim Cosmochim Acta 52:979–988
783 Peccerillo A, Frezzotti ML, De Astis G, Ventura G (2006) Modeling the magma plumbing system
784 of Vulcano (Aeolian Islands, Italy) by integrated fluid-inclusion geobarometry, petrology, and
785 geophysics. Geology 34:17. http://doi.org/10.0030/G22117.1
786 Pollard DD, Delaney PT, Duffield WA, Endo ET, Okamura AT (1983) Surface deformation in
787 volcanic rift zones. Tectonophysics 94:541–584
788 Robertson AHF, Stillman CJ (1979) Submarine volcanic and associated sedimentary rocks of the
789 Fuerteventura Basal Complex, Canary Islands. Geol Mag 116:203–214
790 http://doi.org/10.1017/S0016756800043612
791 Roedder E (1965) Liquid CO_2 inclusions in olivine-bearing nodules and phenocrysts from basalts.
792 Am Miner 50:20–40
793 Roedder E (1984) Geothermobarometry of ultramafic xenoliths from Loihi seamount, Hawaii, on
794 the basis of CO_2 inclusions in olivine. Earth Planet Sci Lett 66:369-379
795 Rosso KM, Bodnar RJ (1995) Detection limits of CO_2 in fluid inclusions using microthermometry
796 and laser Raman spectroscopy and the spectroscopic characterization of CO_2. Geochim
797 Cosmochim Acta 59:3961–3975
798 Ryan MP (1988) Structure of Active Magmatic Systems' Kilauea Volcano, Hawaii. Journal of
799 Geophys Res, 93(B5), 4213–4248.
800 Scandone R, Cashman KV, Malone SD (2007) Magma supply, magma ascent and the style of
801 volcanic eruptions. Earth Planet Sci Lett 253:513–529
802 http://doi.org/10.1016/j.epsl.2006.11.016
803 Schmincke HU (1982) Volcanic and chemical evolution of the Canary Islands. Geol African cont
804 marg pp. 273−306
805 Schmincke HU, Sumita M, (1998) Volcanic evolution of Gran Canaria reconstructed from apron
806 sediments: synthesis of vicap project drilling. Proceedings of the Ocean Drilling Program, Sci
807 Res 157:443–469. http://doi.org/10.2973/odp.proc.sr.157.135.1998
808 Schwarz S, Klügel A, Wohlgemuth-Ueberwasser C (2004) Melt extraction pathways and stagnation
809 depths beneath the Madeira and Desertas rift zones (NE Atlantic) inferred from barometric
810 studies. Contrib Mineral Petrol 147:228–240. http://doi.org/10.1007/s00410-004-0556-4
811 Shaw HR (1980) The fracture mechanisms of magma transport from the mantle to the surface.
812 Physic magma processes 64:201-264

Stroncik NA, Klügel A, Hansteen TH (2009) The magmatic plumbing system beneath El Hierro (Canary Islands): constraints from phenocrysts and naturally quenched basaltic glasses in submarine rocks. Contrib Mineral Petrol 157: 593–607. http://doi.org/10.1007/s00410-008-0354-5

Touret JL (2001) Fluids in metamorphic rocks. Lithos 55:1-25

Ulmer P (1986) NORM-Program for cation and oxygen mineral norms. Computer Library, Institut für Mineralogie und Petrographie

Vaggelli G, Francalanci L, Ruggieri G, Testi S (2003) Persistent polybaric rests of calcalkaline magmas at Stromboli volcano, Italy: pressure data from fluid inclusions in restitic quartzite nodules. Bull Volcanol 65:385–404. doi:10.1007/s00445-002-0264-8

Van den Kerkhof AM (1988) The system CO_2 –CH_4 –N_2 in fluid inclusions: theoretical modelling and geological applications. PhD Dissertation, Amsterdam Free University, 206 pp.

Villa IM, Peverelli V, Oglialoro E, Frezzotti ML (submitted) Halogens in the lithospheric mantle beneath El Hierro (Canary Islands). Chem Geol

Viti C, Frezzotti ML (2000) Re-equilibration of glass and CO_2 inclusions in xenolith olivine: A TEM study. Am Mineral 85:1390-1396

Vityk MO, Bodnar R J (1998) Statistical microthermometry of synthetic fluid inclusions in quartz during decompression reequilibration. Contrib Mineral Petrol 132:149-162

Voog DB, Palomé SP, Hirn A, Charvis P, Gallart J, Rousset D, Perroud H (1999) Vertical movements and material transport during hotspot activity: Seismic reflection profiling offshore La Réunion. J Geophy Res 104:2855-2874

Wanamaker B.J, Evans B (1989) Mechanical re-equilibration of fluid inclusions in San Carlos olivine by power-law creep. Contrib Mineral Petrol 102:102-111

Wang X, Chou IM, Hu W, Burruss RC, Sun Q, Song Y (2011) Raman spectroscopic measurements of CO_2 density: Experimental calibration with high-pressure optical cell (HPOC) and fused silica capillary capsule (FSCC) with application to fluid inclusion observations. Geochim Cosmochim Ac 75:4080–4093. http://doi.org/10.1016/j.gca.2011.04.028

Wells PR (1977) Pyroxene thermometry in simple and complex systems. Contrib Mineral Petrol 62:129-139

Witt-Eickschen G, Seck HA (1991) Solubility of Ca and Al in orthopyroxene from spinel peridotite: an improved version of an empirical geothermometer. Contrib Mineral Petrol, 106:431-439

Wright RB, Wang CH (1973) Density effect on the Fermi resonance in gaseous CO_2 Raman scattering. J Chem Phys 58: 2893–2895

Wulff-Pedersen E, Neumann ER, Jensen BB (1996) The upper mantle under La Palma, Canary Islands: formation of Si−K−Na-rich melt and its importance as a metasomatic agent. Contrib Mineral Petrol 125: 113–139. http://doi.org/10.1007/s004100050210

Yamamoto J, Kagi H (2006) Extended Micro-Raman Densimeter for CO_2 Applicable to Mantle-originated Fluid Inclusions. Chemistry Lett 35:610–611. http://doi.org/10.1246/cl.2006.610

Zanon V (2003). Magmatic feeding system and crustal magma accumulation beneath Vulcano Island (Italy): Evidence from CO_2 fluid inclusions in quartz xenoliths. J Geophy Res 108:2298. http://doi.org/10.1029/2002JB002140

Zanon V, Nikogosian I (2004) Evidence of crustal melting events below the island of Salina (Aeolian arc, southern Italy). Geol Mag 141:525–540. http://doi.org/10.1017/S0016756804009124

Zanon V, Frezzotti ML (2013) Magma storage and ascent conditions beneath Pico and Faial islands (Azores archipelago): A study on fluid inclusions. Geochemistry, Geophysics, Geosystems 14:3494–3514. http://doi.org/10.1002/ggge.20221

Zanon V (2015) Conditions for mafic magma storage beneath fissure zones at oceanic islands. The case of São Miguel island (Azores archipelago). Geol Soc, Lond Special Public 422: 85–104

Figure Captions

Fig. 1 a Geographical setting of Canary Islands showing the location and age of the volcanic products and the main building edifices (Post-erosional stage, Post-shield gap, Shield stage), (Carracedo1999, Acosta et al., 2003). The yellow lines define the main structures of Atlantic and African tectonic units; **b** DEM image of El Hierro Island showing its morpho-structural setting. The red star is the outcrop of ultramafic xenoliths rocks collected along the El Julan Valley, relative to Rift Volcanism cycle.

Fig. 2 a basaltic lava flow with ultramafic xenoliths in the outcrop of El Julan cliff Valley; **b-h** microphotographs of peridotites, **b** Olivine porphyroclasts (Ol I) with kink-bands, harzburgite XML9, crossed polarizers; **c** Orthopyroxene porphyroclasts (Opx I) with exsolution lamellae of clinopyroxene (Cpx), lherzolite XML8, crossed polarizers; **d** Orthopyroxene porphyroclasts (Opx I) with rims free of exsolution lamellae of Cpx, harzburgite XML7, parallel polarizers; **e** Orthopyroxene porphyroclasts (Opx I) without exsolution lamellae, harzburgite XML4, parallel polarizers; **f** Olivine porphyroclasts (Ol I) forming triple junctions, and spinel (Sp), harzburgite XML7, crossed polarizers; **g** The neoblast assemblage of Ol + Opx + Cpx + Sp in narrow zone. lherzolite XML3, crossed polarizers; **h** Olivine porphyroclasts (Ol I) and neoblasts (Ol II) forming narrow alignments highlighted by yellow broken lines, dunite XML1, crossed polarizers. Pictures are made on double polish section - 100µm.

Fig. 3 Microphotographs of early *Type I* fluid inclusions: **a, c** Intragranular trails and spatially isolated clusters of *Type I* fluid inclusions, harzburgite XML7, parallel polarizers; **b** Carbonate (high birefringence) in fluid inclusions and veins (red arrows) in intragranular trails in olivine porphyroclast (Ol), harzburgite XML7, crossed polarizers; **d,** Multiphase fluid inclusions with polygonal-rounded shapes and evidences of decrepitation (red arrows), harzburgite XML7 parallel polarizers.

Fig. 4 a Microphotographs of Type 1 inclusion containing several daughter mineral phases identified by Raman analysis, including anhidrite (Anh), dolomite (Dol), Sulfohalite, $MgSO_4$+H_2O, apatite (Ap), spinel (Sp), and CO_2+N_2 fluids; **b** Raman spectrum of apatite; **c** Raman spectrum of anhydrite; **d** Raman spectrum of water in $MgSO_4$; **e)** Raman spectrum of anhydrite, sulfohalite, and dolomite; **f** Raman spectrum of spinel and anhidryte. Numbers in spectra report vibrations in $cm^{-1.}$ Asterisk indicates host mineral vibrations.

Fig. 5 Microphotographs of late *Type II* fluid inclusions; **a** intergranular trails (red arrows) in orthopyroxene and clinopyroxene porphyroclasts; **b** decrepitated fluid inclusion in Olivine porphyroclast; **c** spatially isolated clusters of *Type II* fluid inclusions (red arrows); **d** fluid inclusions along preferential crystallographic orientation (010) in Orthopyroxene porphyroclast with exolution lamellae (red arrows).

Fig. 6 Histogram of CO_2 melting temperatures (T_m) for *Type II* (grey square) fluid inclusions, and final CO_2 melting temperatures (T_m) for *Type I* fluid inclusions (black square).

Fig. 7 a Microphotograph of a cluster of *Type I* fluid inclusions. *S4* type (red arrow) and *H3* type (green arrows), see text; molar volumes in yellow; **b, c** Raman spectrum of a CO_2+ N_2 fluid inclusion; (Δ) =Fermi doublet.

Fig. 8 CO_2 – N_2 diagram of Klemd et al. (1992). Green dots are molar volume of fluids. Fluid inclusion *S4* (red arrow) and *H3* (red broken circle-line).

907 **Fig. 9** Histogram of distribution for Th_L measured by microthermometry in 512 fluid *Type II*
908 inclusions. Data from Orthopyroxenes (black square), Clinopyroxenes (grey square), Olivine (polka
909 dots square).

910 **Fig. 10** Histograms of *Type II* fluid inclusions in LT (a) and HT-type (b). Data from
911 Orthopyroxenes (black square), Clinopyroxenes (grey square), Olivine (dotted square).

912 **Fig. 11** Histograms of Th_L measured in *Type II* fluid inclusions ≥ 3μm made based on host
913 minerals: Orthopyroxenes (black square), Clinopyroxenes (grey square), Olivine (polka dots
914 square).

915 **Fig. 12** Histograms of the density values in *Type II* fluid inclusions of LT and HT-type of rocks
916 (respectively **a** and **b**). Two main peaks of distribution can be appreciated in both of the histograms.

917 **Fig. 13** Isochoric P-T diagram for analysed fluid inclusions. The purple start indicates the the origin
918 condition depth of *Type I* fluid inclusions. The couple of blue and green stars indicate the
919 intersection of the isochores of LT and HT-type of rocks respectively. Red arrows describe the
920 isobaric heating.

921 **Fig. 14** Schematic representation of the plumbing magma system of El Hierro island at 50 ka,
922 during the volcanic activity phase of the Rift Volcanism phase. The black star on the bottom
923 represents the depth condition of mantle xenoliths. A deep-seated reservoir is identified from 36 to
924 22 km, which fed a shallower reservoir at about 12-10 km.

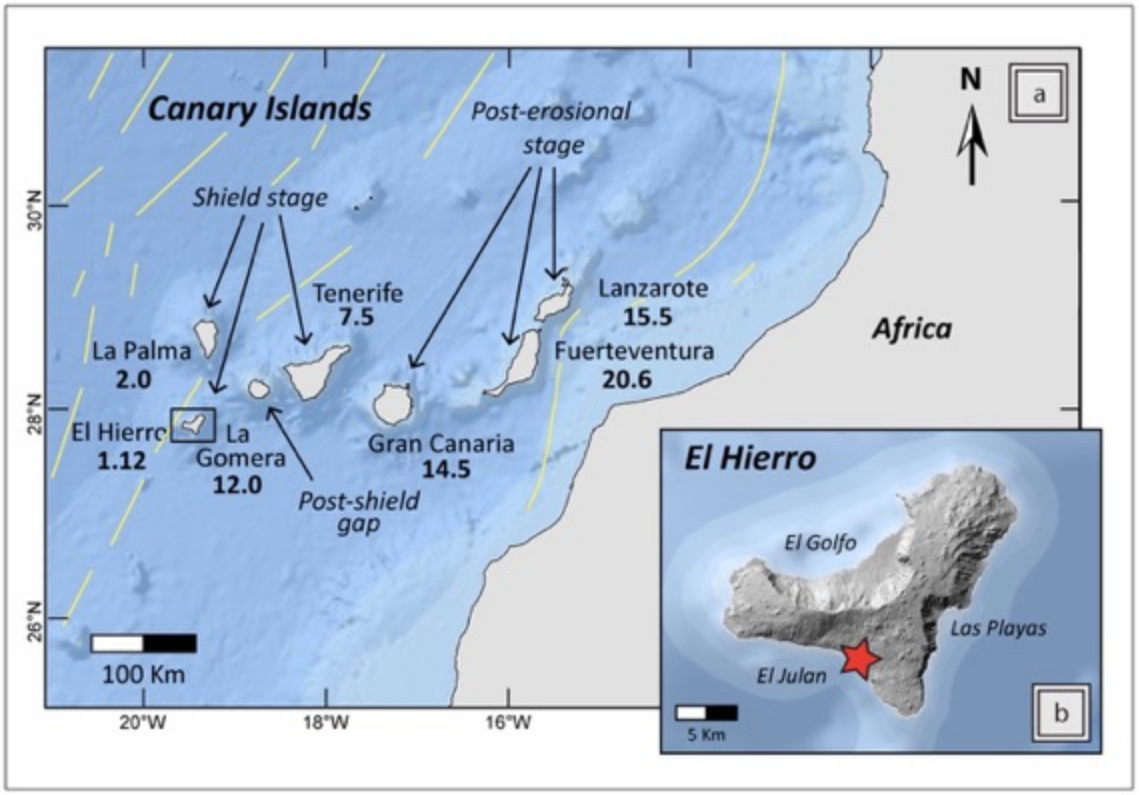

Oglialoro et. al-**Fig. 1**

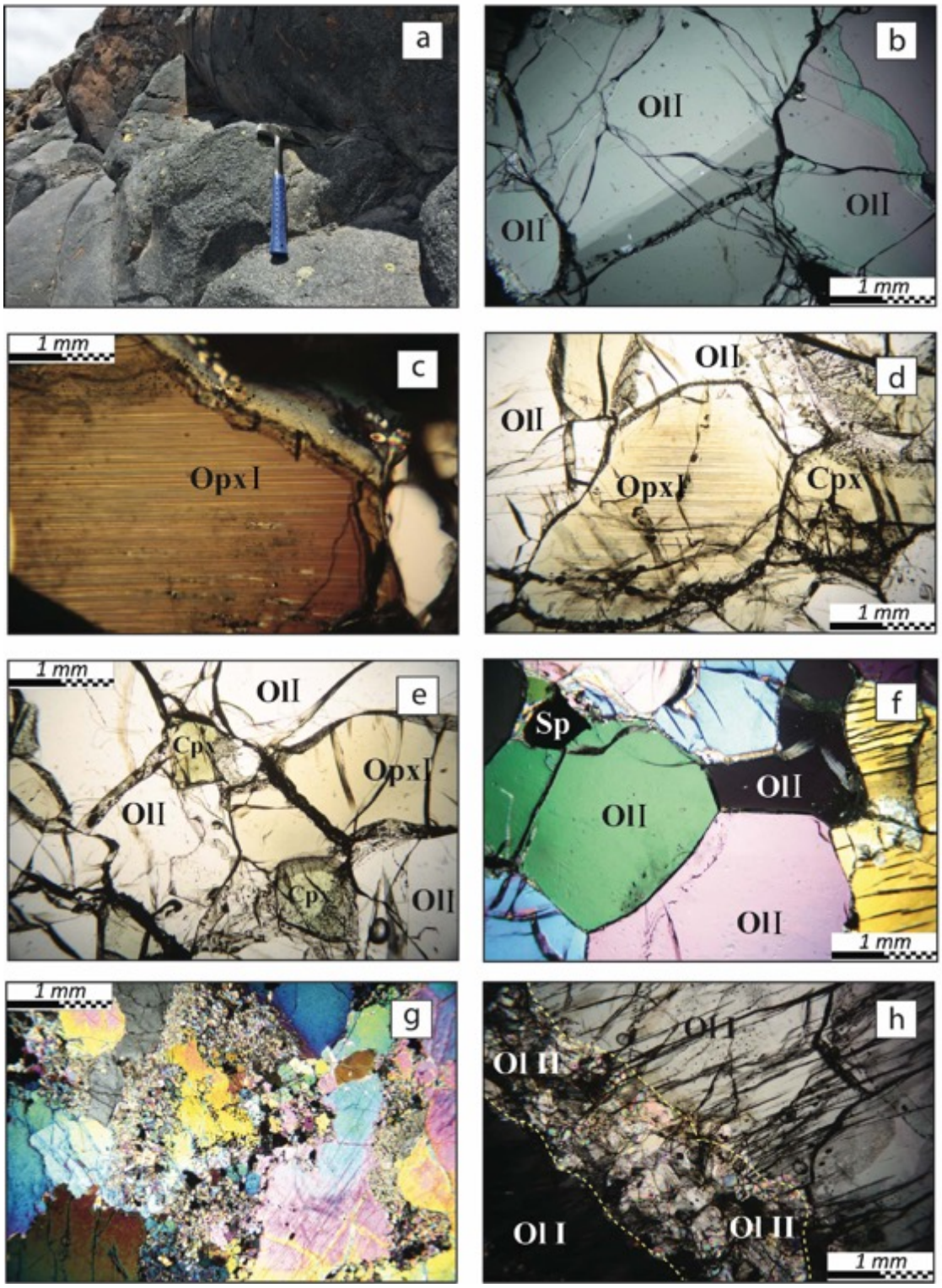

Oglialoro et. al-**Fig. 2**

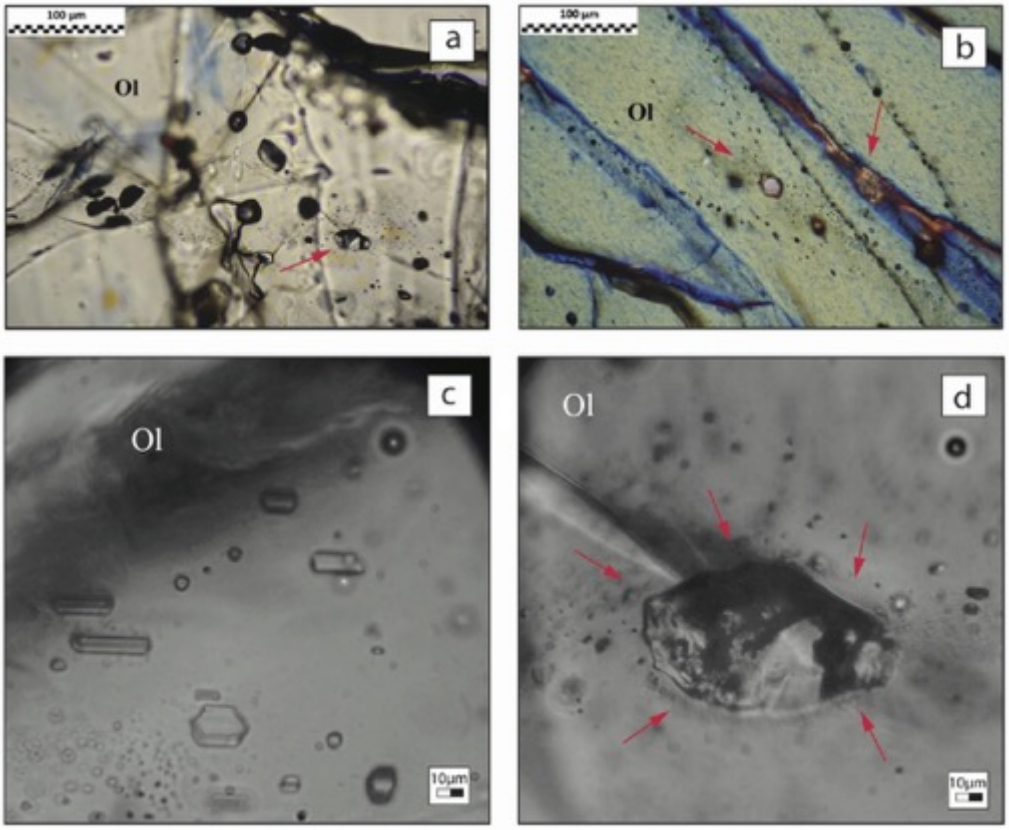

Oglialoro et. al-**Fig. 3**

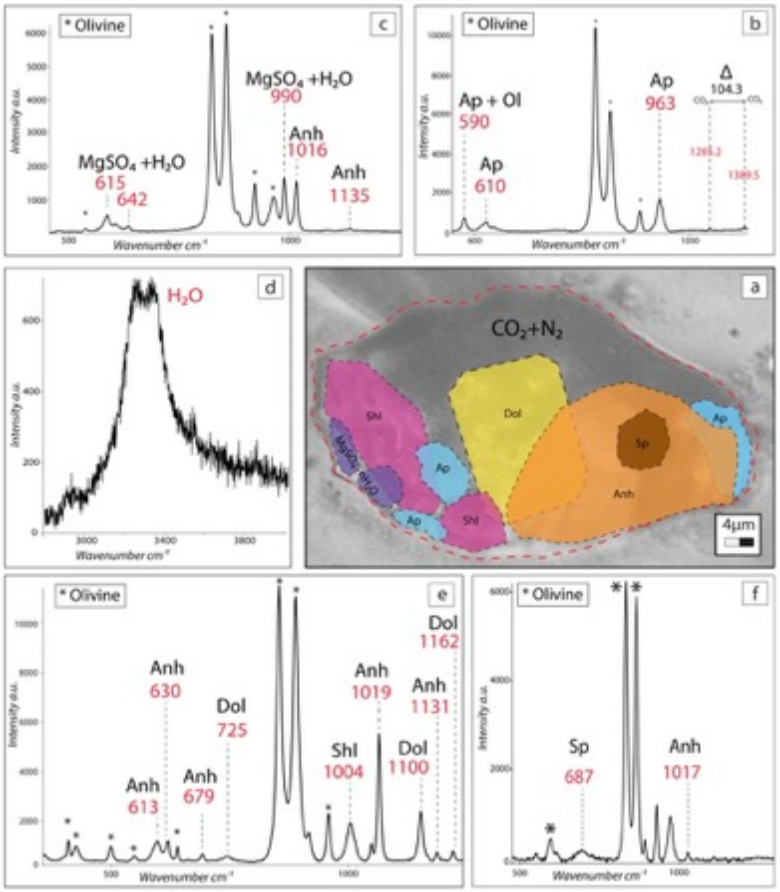

Oglialoro et. al-**Fig. 4**

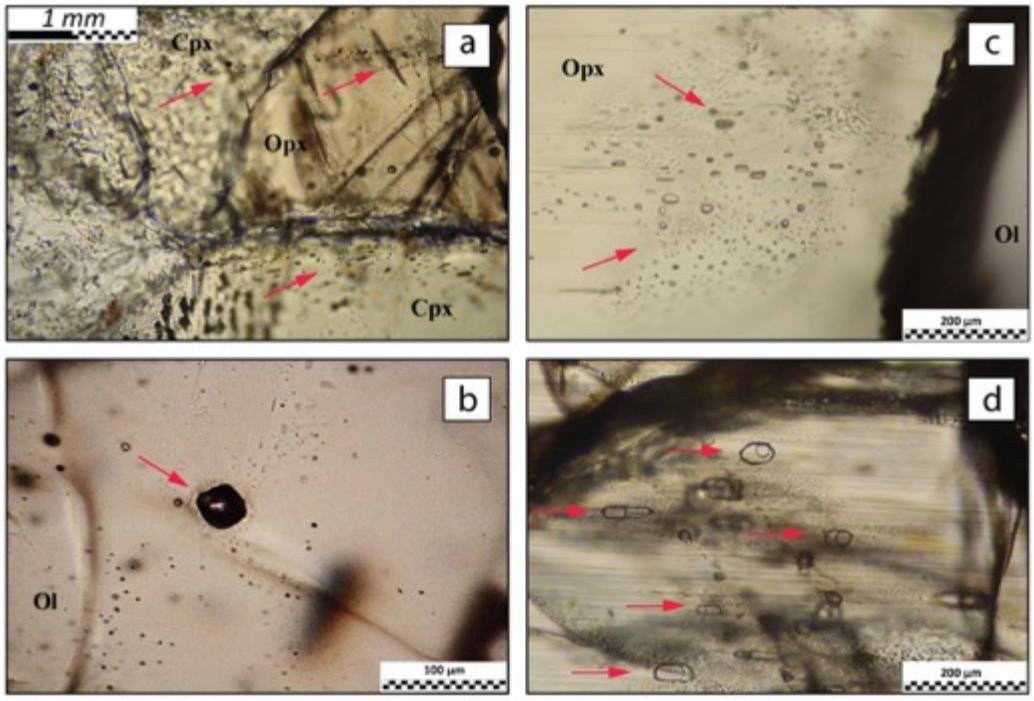

Oglialoro et. al-**Fig. 5**

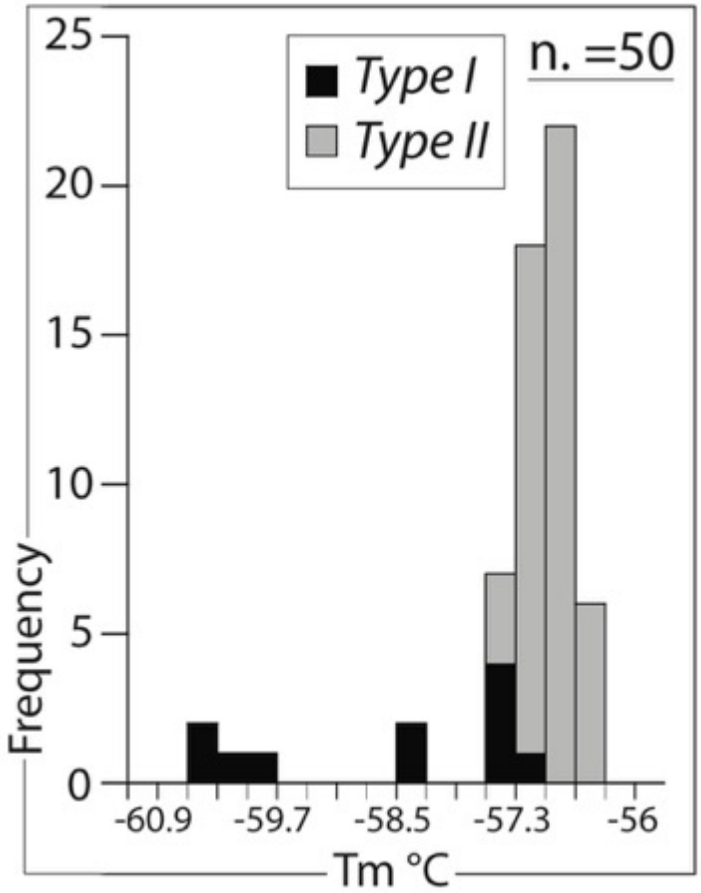

Oglialoro et. al-**Fig. 6**

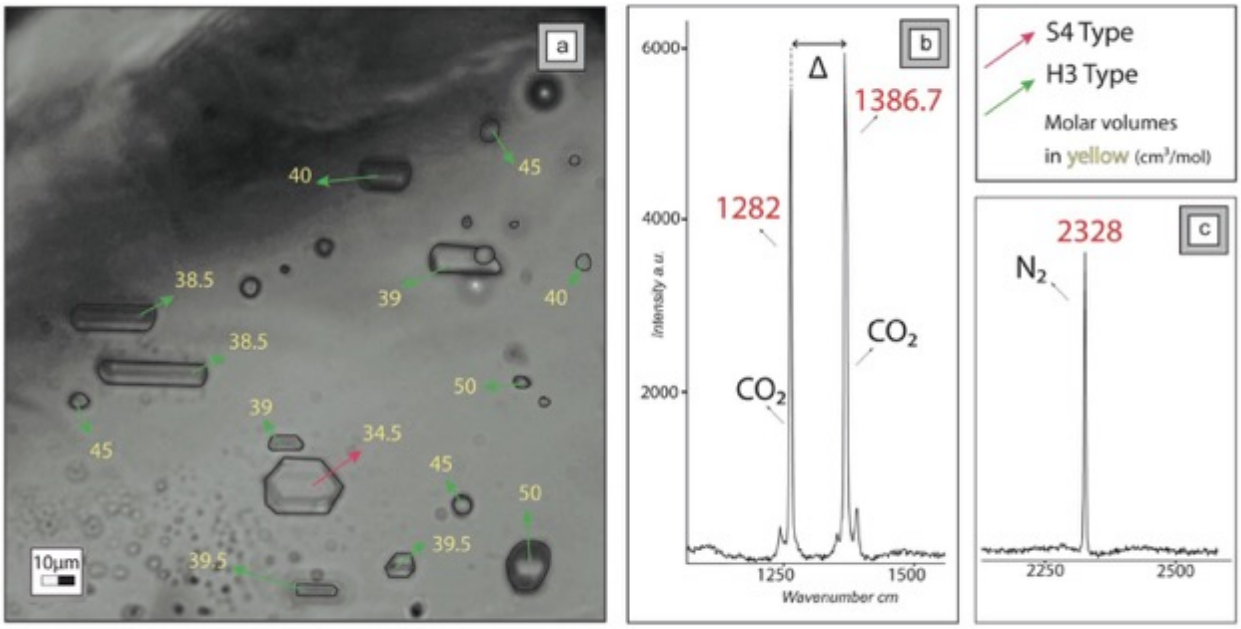

Oglialoro et. al-**Fig. 7**

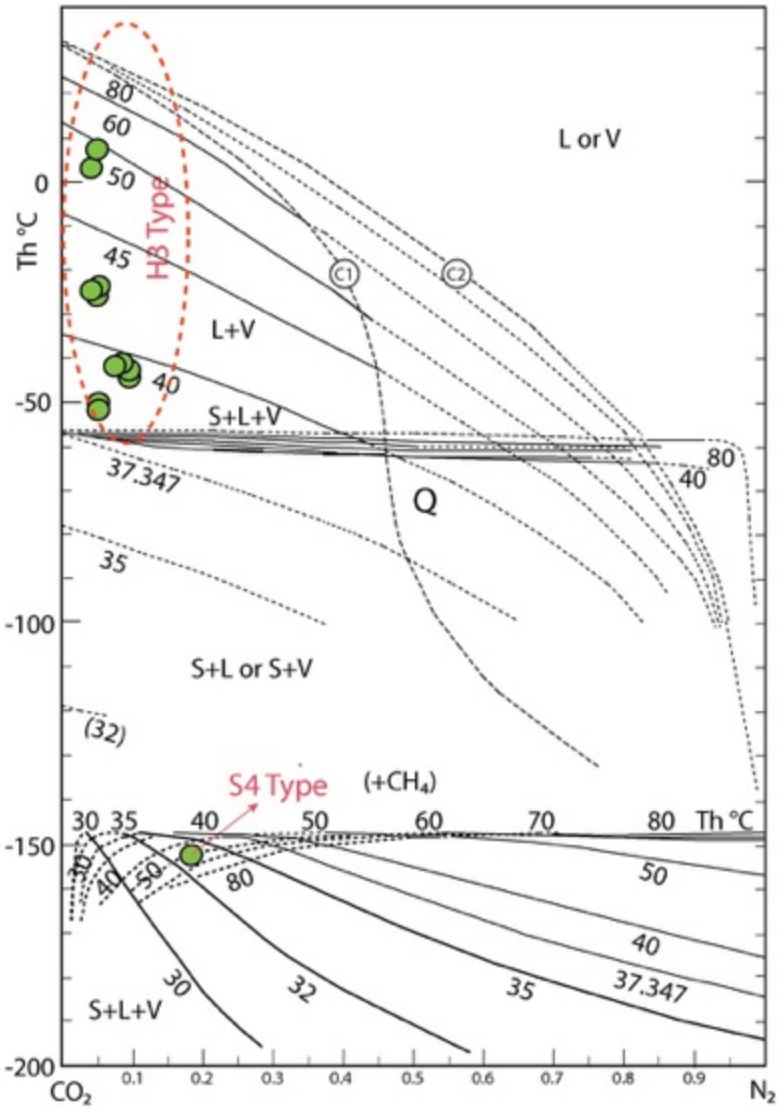

Oglialoro et. al-**Fig. 8**

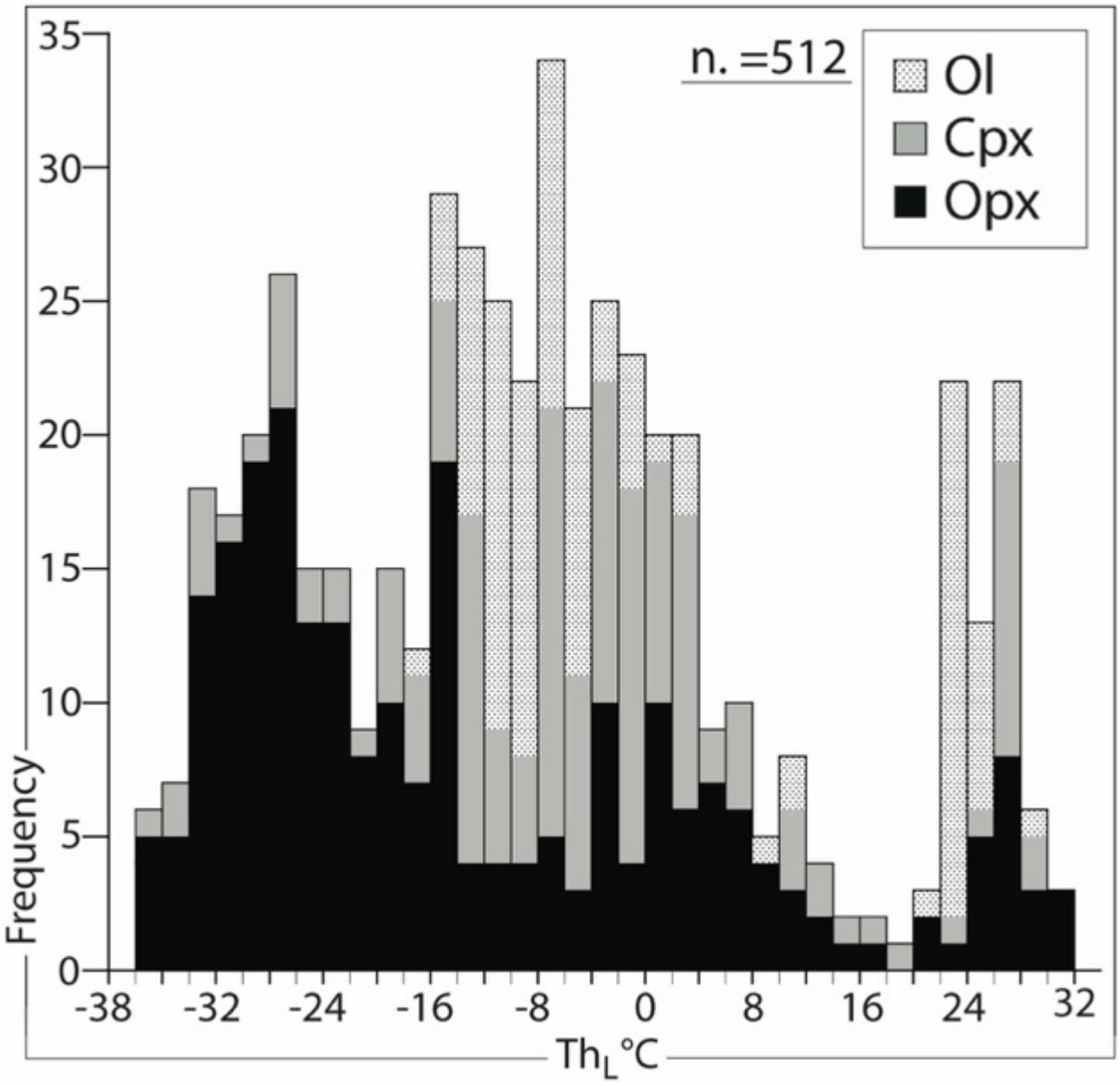

Oglialoro et. al-**Fig. 9**

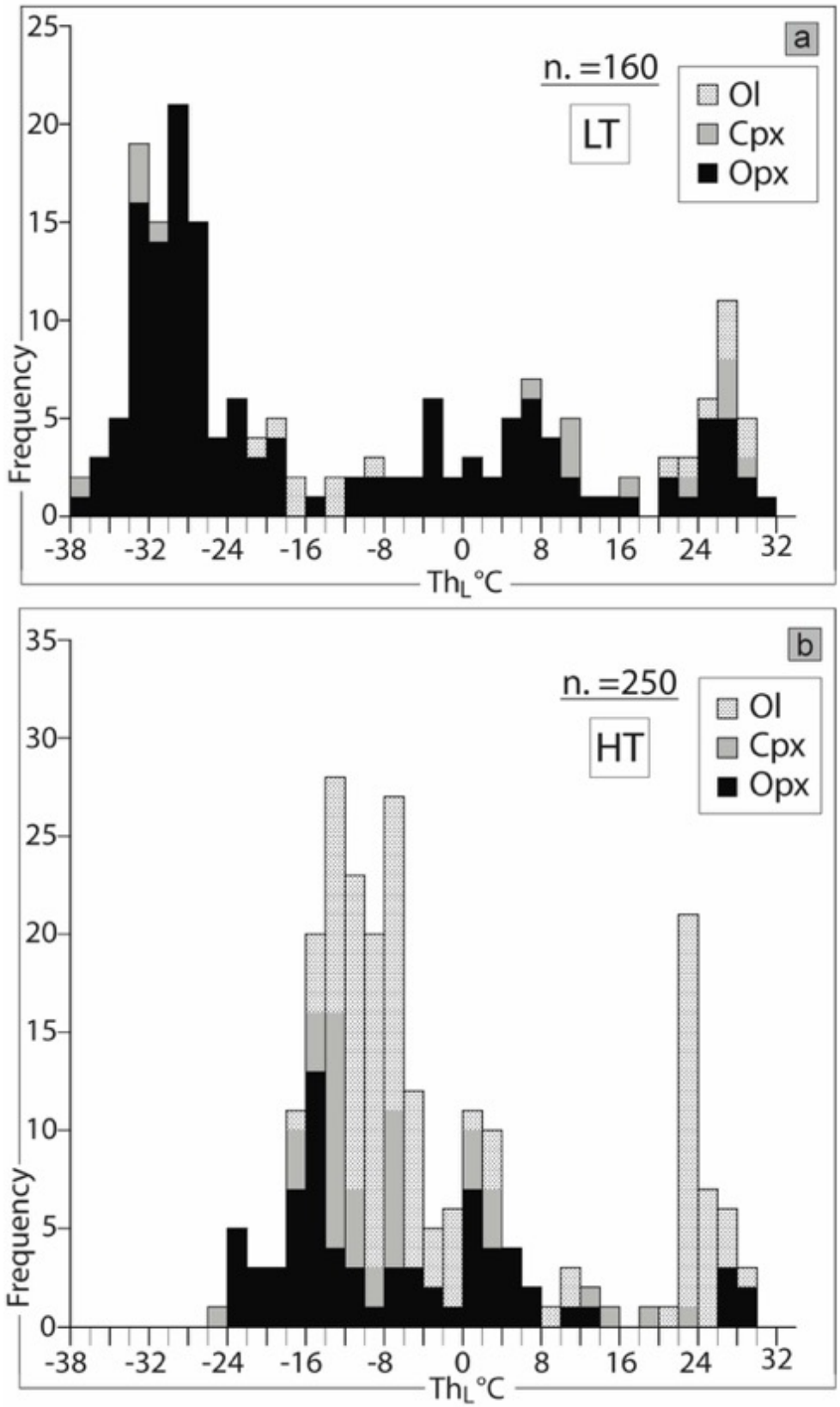

Oglialoro et. al-**Fig. 10**

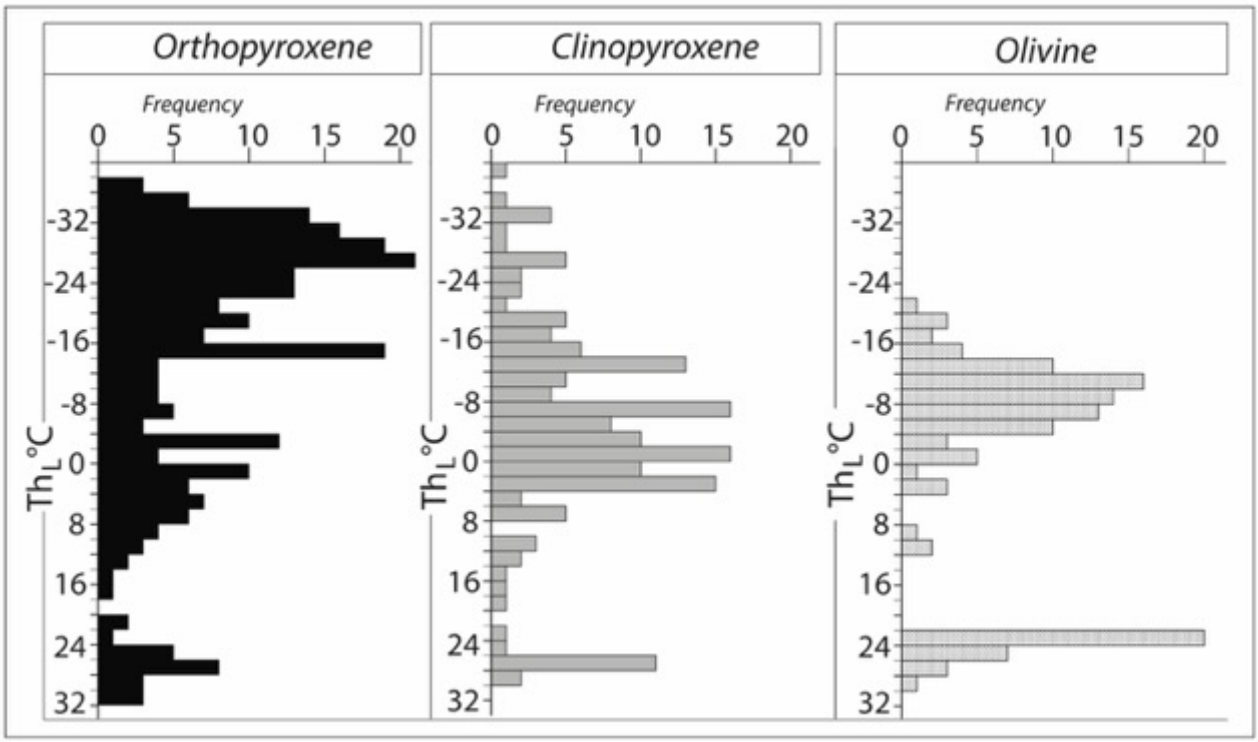

Oglialoro et. al-**Fig. 11**

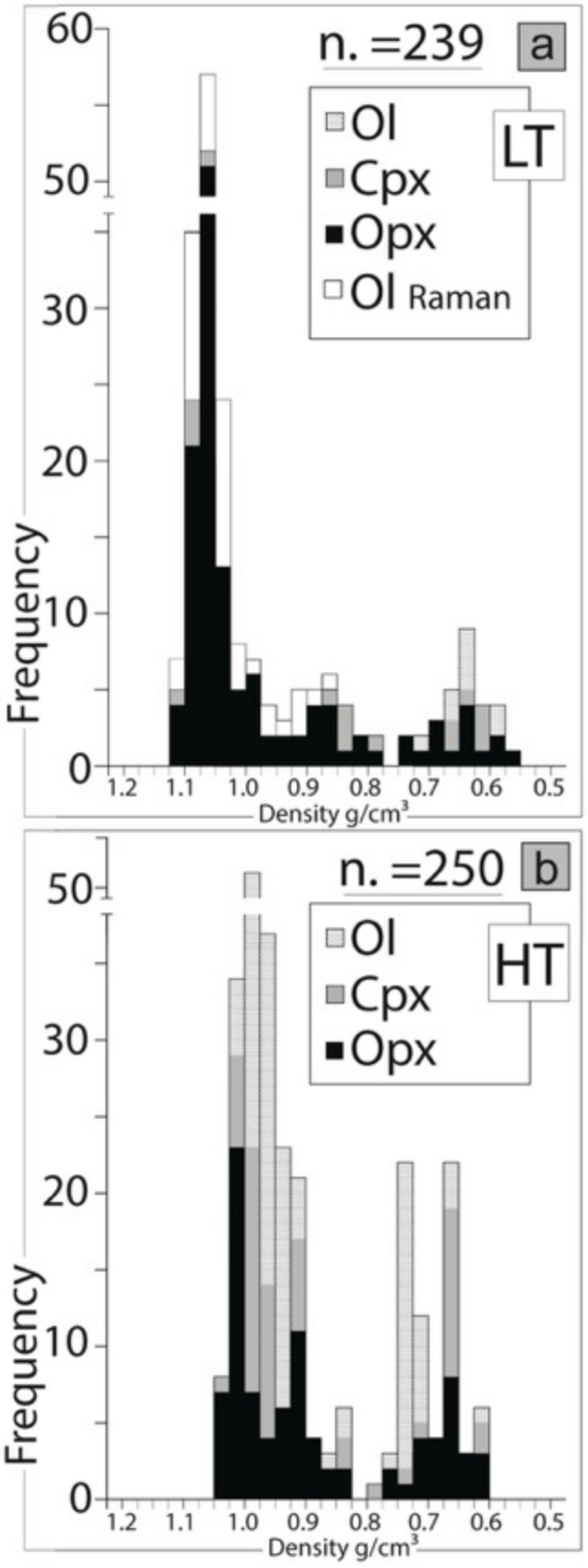

Oglialoro et. al-**Fig. 12**

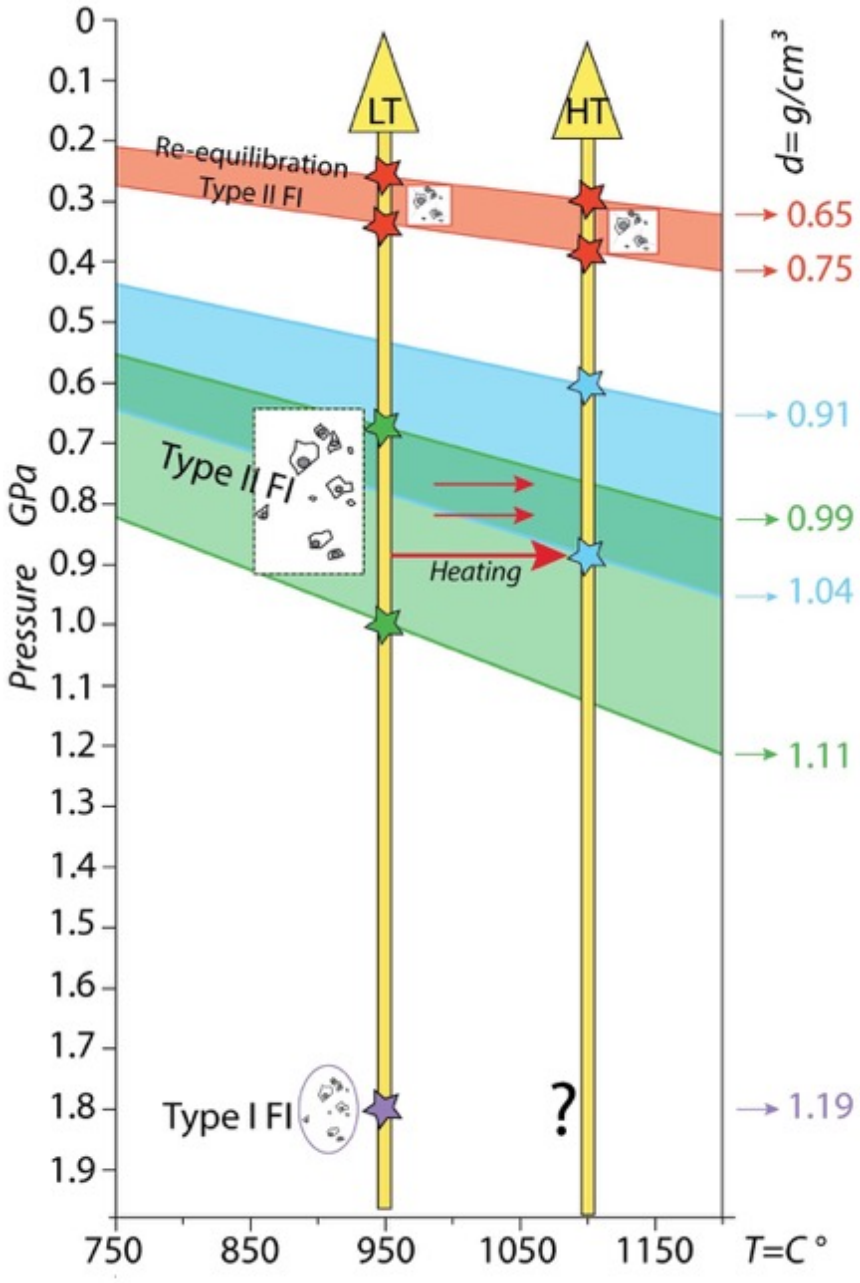

Oglialoro et. al-**Fig. 13**

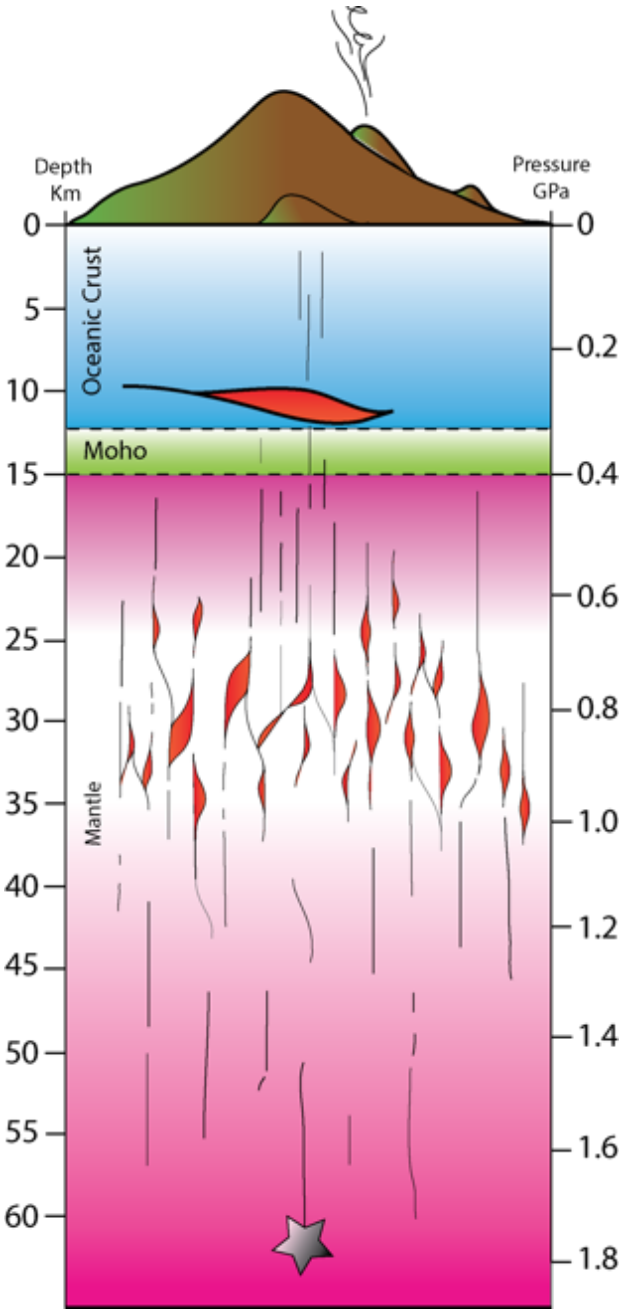

Oglialoro et. al-**Fig. 14**

7. CONCLUSIONS

The scope of this thesis is to demonstrate the importance of combined fluid inclusion and petrological studies to understand magma ascent and volcanic eruption dynamics, as well as to characterize the magma plumbing system of El Hierro volcano during the recent Rift Volcanism activity (158 ka to present). The conclusions of this thesis are based on a combination of petrological, thermodynamical, and geochemical studies in peridotites and in fluid inclusions.

The studied rocks consist of dunites, harzburgites and lherzolites (olivine-orthopyroxene-spinel series), from a lava flow date at 40 ka. Most harzburgite and lherzolite rocks show a variable recrystallization degree (from 10 to 50 %) from protogranular to porphyroclastic textures. In the most recrystallized samples, two generations of olivine and orthopyroxene are observed. Olivine shows large and elongated strained grains (porphyroclasts) and smaller polygonal strain-free ones (neoblasts). Orthopyroxene shows euhedral, exsolved strained large grains (porphyroclasts) and smaller polygonal, clear, mildly strained (neoblasts). Finally, clinopyroxene and spinel are presents as small interstitial grains.

Olivine Mg# (Mg# = Mg/Mg+Fe) range from 89.3 to 91, with the highest values in harzburgites. Orthopyroxene and clinopyroxene contain Mg# between 0.90 to 0.91 wt%, with an increase in Al_2O_3 (opx: 2.1- 3.7; cpx: 1.6-4.5 wt.%) and a decrease in Cr_2O_3 (opx: 0.2-0.7; cpx: 0.4-1.1 wt.%) from dunites to lherzolites. These chemical variations have been interpreted as the occurrence of a depletion event due to partial melting events (e.g., Neumann et al. 1991; 2004).

Geothermobarometry based on mineral chemical equilibria (e.g., Wells 1977; Brey and Koehler 1990; Witt-Eickschen and Seck 1991; Koehler and Brey 1990) defines equilibration pressure conditions of peridotites from 1.5 GPa to 2 GPa, and temperatures from 800 to 950 °C (in LT peridotites) and from 900 to 1100 °C (in HT peridotites). The different temperature conditions of peridotites are suggested to result from isobaric heating at various depths (e.g., Neumann et al. 1991; Hansteen et al. 1998).

Raman microspectroscopy and microthermometry analysis allow to identify two types of fluid inclusions in LT and HT peridotites:

Type I – early CO_2-N_2 fluid inclusions, containing dominantly carbonate/sulfate/phosphate/ spinel daughter phases (LT peridotites). In CO_2-N_2 fluids, X_{N2} varies from 0.01 to 0.18. The highest density *Type I* CO_2-N_2 (X_{N2} = 0.18; d=1.19 g/cm$^{3)}$ indicates equilibration P-T conditions in the lithosphere at 1.8 GPa and 950 °C (~ 60 km depth).

Type II – late pure CO_2 fluid inclusions (both LT and HT peridotites). This type of fluid inclusions shows a bimodal distribution of the homogenization temperatures (T_h), corresponding to density intervals from 0.99 to 1.11 g/cm^3, and from 0.65 to 0.75 g/cm^3. These values define two pressure intervals ranging from 0.67 to 1 GPa and from 0.26 to 0.34 GPa. This bimodal distribution of pressure suggests a multistage ascent behavior of magmas.

Following the noble gas method proposed by Kendrick et al. (2013), the halogens concentration has been obtained in *Type I* fluid inclusions. I/Cl and Br/Cl ratios exhibit values of $6.2*10^{-4}$ - $6.5*10^{-4}$ and of $2.02*10^{-3}$ - $1.96*10^{-3}$, respectively. These ratios result higher than typical MORB/OIB mantle (from $1.1*10^{-5}$ to $1.01*10^{-4}$), supporting a metasomatic origin for *Type I* fluids at lithospheric depths of about 60 km. I/Cl and Br/Cl ratios suggest an origin of fluids from recycled old oceanic crust (metabasalts + metasediments).

Fluid inclusions and petrological studies in peridotite xenoliths allowed to propose a model for the magma plumbing system of El Hierro volcano. According to *Type I* fluid inclusion and mineral geothermobarometry, the minimum depth of origin of peridotites has been identified at about 60 ± 10 km in the lithosphere. Two shallower trapping events of CO_2 (*Type II*) degassed from basaltic magmas allow to identify the magma rest episodes on ascent to the surface. The first one, from 36 to 22 km, in the lithospheric mantle, and the latter, from 10 to 12 km, in the lower oceanic crust. The deeper magma accumulation region is interpreted as a "vertically staked reservoir", where the magma is stored in a series of vertically interconnected pockets distributed over a wide depth interval (~14 km). This mantle magma accumulation region fed the shallower reservoir in the

lower crust, which is suggested as an ephemeral level of magma stagnation prior to eruption.

The proposed model is similar to the magma ascent dynamics reconstructed for the last 2011-2012 El Hierro eruption (Martí et al. 2013a, b.), proving that the magma plumbing system at El Hierro did not significantly change in the last 40 ka, in its mature stage. The changing of ascent magma dynamics can be related to a longer interval of time (~ 1 Ma): during the immature stage of the ocean volcanic island (El Tinor edifice, 1.2 Ma) when a single magma reservoir was possibly located in the deep lithosphere, and that subsequently evolved in an interconnected system of magma pockets (Rift Volcanism, 158 ka), without the presence of a shallow level of magma in the crust.

For future eruptions the data obtained suggests that magma ascent mainly rising from the deep reservoir can be expected. Moreover, the reconstruction of magma plumbing systems through geochemical studies in peridotites and in fluid inclusions can be successfully applied in other similar volcanic ocean island.

Future research may give further insights into magma ascent dynamics of this volcano and on the geochemical nature of the lithosphere. An underdetermined variable is the evolution of the magma plumbing system during the whole sub aerial activity of El Hierro volcano, from 1.12 Ma. Further work on fluid inclusion geothermobarometry in peridotite xenoliths from older lavas is therefore necessary to reveal ascent pathways and residence depths of magmas leading to the formation of the three consecutive volcanic edifices.

Another key question is the ultimate nature of mantle metasomatic fluids which have affected the lithosphere beneath the Canary Islands. Further petrological geochemical studies of peridotites are necessary. Trace element analyses in minerals and fluids contained in the inclusions would be useful to identify the source of metasomatic fluids. This would improve present models of the petrogenesis of basaltic magmas in the Canary Islands.

8. ACNOWLEDGEMENTS

Il più grande ringraziamento va alla mia Tutor Prof.ssa Maria Luce Frezzotti, per avermi seguito motivato, e insegnato "a fare scienza". Le devo molto, ed è stata fondamentale nel raggiungere questo traguardo, spingendomi sempre a fare il meglio. Un grande Grazie sincero e pieno di stima.

Grazie al Prof. Igor Villa per esserci stato, avermi dato consigli e la possibilità di lavorare con lui; alla Dott.ssa Simona Ferrando per avermi fatto capire come ci si può innamorare di uno strumento; al Dott. Groppelli e alla Dott.ssa Principe per avermi seguito sul campo. Alla Dott.ssa Nadia Malaspina e al Dott. Marcello Campione per gli spunti che mi hanno dato.

Alla Dott.ssa Carla Tiraboschi, la collega che chiunque vorrebbe avere. Grazie per avermi sostenuto e aiutato in questo ultimo anno, e per essere diventata una favola-H di amica.

A Veronica e Andrea: piccoli, grandi studenti: senza di voi il laboratorio non sarebbe stato lo stesso. A Mara, Marta e Alberto, per i pranzi e le sigarette in Bicocca.

Ai miei amici: Andrea Bufo per non esserti mai arrabbiato per l'affitto in ritardo; Andrea Cortese per il sostegno e le cene preparate, per esserci sempre stato come un vero amico sa fare; a Mario Zaccardi per le nostre serate e per la fiducia nel futuro. Vi voglio bene ragazzi, siete una grande certezza in questa città.

Gli amici del liceo ogni tanto si perdono, ma ci sono anche quelli che non ti lasciano mai: Andrea Santelli le nottate rimarranno indimenticabili.

Alla prima amica trovata in Bicocca. Grazie Valeria, sei la mia vulcanologa preferita.

A tutta la mia famiglia e a Liliana, a Eva e a Luciano, tutti lontani ma sempre pronti a darmi forza.

Al mio piccolo Theo, che mi ha riscaldato seduto sulle gambe aspettando pazientemente che avessi finito il lavoro per poi uscire a giocare.

A tutti voi Grazie di cuore.

Senza di te tutto questo non sarebbe stato possibile, e la mia vita non sarebbe la stessa: grazie per aver capito e condiviso i momenti belli e brutti. A te, Francesco dedico questa tesi, a te che sei l'amore certo della mia vita.

Per pesare il cuore con entrambe le mani ci vuole coraggio
E occhi bendati, su un cielo girato di spalle
La pazienza, casa nostra, il contatto, il tuo conforto
Ha a che fare con me
È qualcosa che ha a che fare con me

9. APPENDIX

Microthermometry measurements of fluid inclusions in mineral host of mantle xenoliths collected in El Julan, El Hierro Island.

Late *Type II* fluid inclusions

SAMPLE	AREA	Min.Host	Type	Petrography FI	PHASE	T_m °C	T_h °C
XML3	B1	Opx	Late	INTRAGRANULAR	L		29.2
"	"	"	"	"	"		29.2
"	"	"	"	"	"		13
"	"	"	"	"	"		9
"	"	"	"	"	"		3
"	"	"	"	"	"	-56.6	1
"	"	"	"	"	"		11.8
"	"	"	"	"	"		4.5
"	"	"	"	"	"		2
"	"	"	"	"	"		2
"	"	"	"	"	"		-13
"	"	"	"	"	"		-17.1
"	"	"	"	"	"		-2.5
"	"	"	"	"	"		-2
"	"	"	"	"	"		-5
"	"	"	"	"	"		1.2
"	"	"	"	"	"		4.5
"	"	"	"	"	"		4.5
"	"	"	"	"	"		2.5
"	"	"	"	"	"		-2.3
"	"	"	"	"	"		-1
"	"	"	"	"	"		2.8
"	"	"	"	"	"		1.8
"	"	"	"	"	"		1.5
"	"	"	"	"	"		1.1
XML3	A2	Opx	Late	INTRAGRANULAR	L		-8.5
"	"	"	"	"	"		-8.5
"	"	"	"	"	"		-13.9
"	"	"	"	"	"	-56.6	-14.3
"	"	"	"	"	"		-11.5
"	"	"	"	"	"		-12.3
"	"	"	"	"	"		-10.5
"	"	"	"	"	"		-10.5
XML3	A1	Opx	Late	INTRAGRANULAR	L		-17
"	"	"	"	"	"		-17.1
"	"	"	"	"	"		-17
"	"	"	"	"	"		-13.5
"	"	"	"	"	"		-15
"	"	"	"	"	"	-56.9	-18.1
"	"	"	"	"	"		-18.1
"	"	"	"	"	"		-15.2
"	"	"	"	"	"		-15.2
"	"	"	"	"	"		-13.5
"	"	"	"	"	"		-15
"	"	"	"	"	"		-13.8
"	"	"	"	"	"		-13.8
"	"	"	"	"	"		-13.8
"	"	"	"	"	"		-15.5
"	"	"	"	"	"		-5.5
"	"	"	"	"	"		7
"	"	"	"	"	"		1.5
XML4	A	Opx	Late	INTRAGRANULAR	L		-4.4
"	"	"	"	"	"		-13.5
"	"	"	"	"	"		-14
"	"	"	"	"	"		-14
"	"	"	"	"	"		-6.2
"	"	"	"	"	"		+2.5
"	"	"	"	"	"		-20.5

Late *Type II* fluid inclusions

SAMPLE	AREA	Min.Host	GENERATION	Type FI	PHASE	T_m ist.°C	T_h °C
XML4	A	Opx	Late	INTRAGRANULAR	L		-22
"	"	"	"	"	"		-22
"	"	"	"	"	"		-22
"	"	"	"	"	"		-1
"	"	"	"	"	"		5.8
XML4	B	Ol	Late	INTRAGRANULAR	L	-56.6	-7
"	"	"	"	"	"		-7
"	"	"	"	"	"		-3.3
"	"	"	"	"	"		-7.5
"	"	"	"	"	"		-7.5
"	"	"	"	"	"		-7.5
"	"	"	"	"	"		-7.5
"	"	"	"	"	"		12
"	"	"	"	"	"		10.5
"	"	"	"	"	"		-10.5
"	"	"	"	"	"		-11.5
XML4	B1	Ol	Late	INTERGRANULAR	L		-12.5
"	"	"	"	"	"		-11.8
"	"	"	"	"	"		-10.5
"	"	"	"	"	"		-14.5
"	"	"	"	"	"		-14
"	"	"	"	"	"		-8
"	"	"	"	"	"		-8.4
"	"	"	"	"	"		-4.5
"	"	"	"	"	"		-4
"	"	"	"	"	"		-2
"	"	"	"	"	"		-8.7
"	"	"	"	"	"		-5.4
"	"	"	"	"	"		-2.6
"	"	"	"	"	"	-56.6	0.5
"	"	"	"	"	"		-5.4
"	"	"	"	"	"		-5.4
"	"	"	"	"	"		-6.9
"	"	"	"	"	"		-6
"	"	"	"	"	"		-6
"	"	"	"	"	"		-10.2
"	"	"	"	"	"		-10.2
"	"	"	"	"	"		-10.4
"	"	"	"	"	"		-9
"	"	"	"	"	"		-9
"	"	"	"	"	"		-9.5
"	"	"	"	"	"		-5.6
"	"	"	"	"	"		-5.6
"	"	"	"	"	"		-3.5
"	"	"	"	"	"		-5
"	"	"	"	"	"		-3.3
"	"	"	"	"	"		-2.5
"	"	"	"	"	"		-2.5
"	"	"	"	"	"		0.5
XML4	B2	Ol	Late	INTERGRANULAR	L		22.7
"	"	"	"	"	"		23
"	"	"	"	"	"		23.5
"	"	"	"	"	"		22.7
"	"	"	"	"	"		23.4
"	"	"	"	"	"		23.4
"	"	"	"	"	"		23
"	"	"	"	"	"		23.5
"	"	"	"	"	"		23.5
"	"	"	"	"	"		25.2

Late *Type II* fluid inclusions

SAMPLE	AREA	Min.Host	GENERATION	Type FI	PHASE	T_m ist.°C	T_h °C
XML4	B2	Ol	Late	INTERGRANULAR	L	-56.6	25.2
"	"	"	"	"	"		25.8
"	"	"	"	"	"		26
"	"	"	"	"	"		25
"	"	"	"	"	"		25.6
"	"	"	"	"	"		26.5
"	"	"	"	"	"		25.6
"	"	"	"	"	"		25
"	"	"	"	"	"		27
"	"	"	"	"	"		27
"	"	"	"	"	"		25.8
"	"	"	"	"	"		25.5
"	"	"	"	"	"		25.5
"	"	"	"	"	"		25.5
"	"	"	"	"	"		26
"	"	"	"	"	"		25.5
"	"	"	"	"	"		-13
"	"	"	"	"	"		-13.5
XML4	B3	Ol	Late	INTRAGRANULAR	L		-10
"	"	"	"	"	"		-9.5
"	"	"	"	"	"		-9.5
"	"	"	"	"	"		-9.8
"	"	"	"	"	"		-12
"	"	"	"	"	"		-9
"	"	"	"	"	"		-9
"	"	"	"	"	"	-56.6	-7.3
"	"	"	"	"	"		-7.3
"	"	"	"	"	"		-8.3
"	"	"	"	"	"		-7.5
"	"	"	"	"	"		-6.2
"	"	"	"	"	"		-11.5
"	"	"	"	"	"		-11.7
"	"	"	"	"	"		-6.8
"	"	"	"	"	"		-5.5
"	"	"	"	"	"		-7.8
XML4	C4	Ol	Late	INTRAGRANULAR	L		-5.5
"	"	"	"	"	"		-3
"	"	"	"	"	"		9
"	"	"	"	"	"	-56.6	-11.5
"	"	"	"	"	"		3
"	"	"	"	"	"		-12
"	"	"	"	"	"		-1.5
"	"	"	"	"	"		-1.4
"	"	"	"	"	"		-1.3
"	"	"	"	"	"		-0.5
"	"	"	"	"	"		-4
"	"	"	"	"	"		-3.8
"	"	"	"	"	"		-2
"	"	"	"	"	"		1.5
"	"	"	"	"	"		2.5
XML4	C5	Ol	Late	INTRAGRANULAR	L		28.5
"	"	"	"	"	"		28
"	"	"	"	"	"		26
"	"	"	"	"	"	-56.6	26
"	"	"	"	"	"		26.5
"	"	"	"	"	"		27
"	"	"	"	"	"		26.5
"	"	"	"	"	"		21.4
"	"	"	"	"	"		-9.5

Late *Type II* fluid inclusions

SAMPLE	AREA	Min.Host	GENERATION	Type FI	PHASE	T_m ist.°C	T_h °C
XML4	C6	Ol	Late	INTRAGRANULAR	L		-9.5
"	"	"	"	"	"	-56.6	-9
"	"	"	"	"	"		-7
"	"	"	"	"	"		-9
"	"	"	"	"	"		-5
"	"	"	"	"	"		-5.5
"	"	"	"	"	"		-6.5
"	"	"	"	"	"		4
XML5	A	Cpx	Late	INTRAGRANULAR	L		27.7
"	"	"	"	"	"		27.5
"	"	"	"	"	"		27.8
"	"	"	"	"	"		28
"	"	"	"	"	"		27.5
"	"	"	"	"	"		27.9
"	"	"	"	"	"		3.5
"	"	"	"	"	"		-1.9
"	"	"	"	"	"		28
"	"	"	"	"	"		28.9
"	"	"	"	"	"		28.3
"	"	"	"	"	"		28.5
"	"	"	"	"	"		28.4
"	"	"	"	"	"	-56.6	-2
"	"	"	"	"	"		-3.5
"	"	"	"	"	"		-3
"	"	"	"	"	"		-2.8
"	"	"	"	"	"		-2.5
"	"	"	"	"	"		-6
"	"	"	"	"	"		-6
"	"	"	"	"	"		-6.1
"	"	"	"	"	"		-1.2
"	"	"	"	"	"		-1.2
"	"	"	"	"	"		-2
"	"	"	"	"	"		-5.2
"	"	"	"	"	"		-5
XML5	A	Cpx	Late	INTRAGRANULAR	L		-2
"	"	"	"	"	"		-0.5
"	"	"	"	"	"		-1.8
"	"	"	"	"	"		-2.7
"	"	"	"	"	"		-2
"	"	"	"	"	"		-2.4
"	"	"	"	"	"		-2.4
"	"	"	"	"	"		-2.7
"	"	"	"	"	"		-1.7
"	"	"	"	"	"		0.5
"	"	"	"	"	"		-1.5
"	"	"	"	"	"		1.3
"	"	"	"	"	"		1
"	"	"	"	"	"	-56.6	-1.5
"	"	"	"	"	"		-1.6
"	"	"	"	"	"		-2.5
"	"	"	"	"	"		-2
"	"	"	"	"	"		-2
"	"	"	"	"	"		3.2
"	"	"	"	"	"		1.5
"	"	"	"	"	"		1.5
"	"	"	"	"	"		1
"	"	"	"	"	"		1
"	"	"	"	"	"		1.5
"	"	"	"	"	"		0.3

Late *Type II* fluid inclusions

SAMPLE	AREA	Min.Host	GENERATION	Type FI	PHASE	T_m ist.°C	T_h °C
XML5	A	Cpx	Late	INTRAGRANULAR	L		0.3
"	"	"	"	"	"		1
"	"	"	"	"	"		2.8
"	"	"	"	"	"		2.8
"	"	"	"	"	"	-56.6	-2
"	"	"	"	"	"		1
"	"	"	"	"	"		15
"	"	"	"	"	"		5.2
"	"	"	"	"	"		5.5
"	"	"	"	"	"		7.8
"	"	"	"	"	"		7.8
"	"	"	"	"	"		1
"	"	"	"	"	"		3
"	"	"	"	"	"		2.3
"	"	"	"	"	"		6.5
XML8	F	Opx	Late	INTRAGRANULAR	L		-28.2
"	"	"	"	"	"		-28
"	"	"	"	"	"		-29.5
"	"	"	"	"	"		-30
"	"	"	"	"	"		-23
"	"	"	"	"	"		-26
"	"	"	"	"	"		-28
"	"	"	"	"	"		-1
"	"	"	"	"	"		-1.2
XML8	E	Opx	Late	INTRAGRANULAR	L		-26.1
"	"	"	"	"	"		-27.4
"	"	"	"	"	"		-27.1
"	"	"	"	"	"		-26.3
"	"	"	"	"	"		-29.3
"	"	"	"	"	"		-31.3
"	"	"	"	"	"		-26
"	"	"	"	"	"	-56.6	-37.5
"	"	"	"	"	"		-28
"	"	"	"	"	"		-26
"	"	"	"	"	"		-28.1
"	"	"	"	"	"		-20.5
"	"	"	"	"	"		-18
"	"	"	"	"	"		-21.5
"	"	"	"	"	"		-21.5
XML8	E	Opx	Late	INTRAGRANULAR	L		18
"	"	"	"	"	"		-18
"	"	"	"	"	"		-30
"	"	"	"	"	"		-27.8
"	"	"	"	"	"	-56.6	-30
"	"	"	"	"	"		-27.5
"	"	"	"	"	"		-23.5
"	"	"	"	"	"		-27.9
"	"	"	"	"	"		-28
"	"	"	"	"	"		30.5
XML8	G	Opx	Late	INTRAGRANULAR	L	-56.6	-30.5
"	"	"	"	"	"		-31.5
"	"	"	"	"	"		-30.5
"	"	"	"	"	"		25
XML 8	A	Opx	Late	INTRAGRANULAR	L	-56.6	-25.8
"	"	"	"	"	"	-56.6	-26.4
"	"	"	"	"	"		-30.5
"	"	"	"	"	"		-30.5
"	"	"	"	"	"		-25
"	"	"	"	"	"	-56.7	-27.6

Late *Type II* fluid inclusions

SAMPLE	AREA	Min.Host	GENERATION	Type FI	PHASE	T_m ist.°C	T_h °C
XML 8	A	Opx	Late	INTRAGRANULAR	L		-29.6
"	"	"	"	"	"		-29.4
"	"	"	"	"	"		-21.5
"	"	"	"	"	"		-22.7
"	"	"	"	"	"		25.6
"	"	"	"	"	L		-30.2
"	"	"	"	"	"		-30.2
"	"	"	"	"	V		25.6
"	"	"	"	"	L		-30.2
"	"	"	"	"	"		-30.9
XML 8	C4	Opx	Late	INTRAGRANULAR	L	-57.3	-5.9
"	"	"	"	"	"		-2.2
"	"	"	"	"	"		-5.6
"	"	"	"	"	"		-8.8
"	"	"	"	"	V		3.1
"	"	"	"	"	"		22.7
"	"	"	"	"	"		24.1
XML 8	C5	Opx	Late	INTRAGRANULAR	V		4.5
"	"	"	"	"	L		0.8
"	"	"	"	"	"		3.2
"	"	"	"	"	"		0.8
"	"	"	"	"	"		5.5
"	"	"	"	"	"	-56.5	-23.8
"	"	"	"	"	"		-18.3
"	"	"	"	"	V		30
XML 8	C6	Opx	Late	INTRAGRANULAR	L		-1.5
"	"	"	"	"	"		-7.1
"	"	"	"	"	"	-56.6	-6.5
"	"	"	"	"	"		0.6
"	"	"	"	"	"		5.6
"	"	"	"	"	"		5.6
"	"	"	"	"	"		8.8
"	"	"	"	"	"		7.3
"	"	"	"	"	V		7.4
"	"	"	"	"	L		7.4
"	"	"	"	"	"		8.3
XML9	A	Opx	Late	INTERGRANULAR	V		26.4
"	"	"	"	"	V		27.5
"	"	"	"	"	L		-13.8
"	"	"	"	"	"	-57.2	-22
"	"	"	"	"	"		-14.5
"	"	"	"	"	"		-14
"	"	"	"	"	"		-19
"	"	"	"	"	"		-11.3
"	"	"	"	"	"		-13.8
"	"	"	"	"	"		27.5
"	"	"	"	"	"		-9
"	"	"	"	"	"		-3.2
XML9	B1	Opx	Late	INTERGRANULAR	L		19.5
"	"	"	"	"	"		-0.3
"	"	"	"	"	"		-24
"	"	"	"	"	"		-14
"	"	"	"	"	"		-14
"	"	"	"	"	"	-56.9	-15.2
"	"	"	"	"	"		-5.3
"	"	"	"	"	"		-5.3
"	"	"	"	"	"		-11.8
"	"	"	"	"	"		-11.5
"	"	"	"	"	"		-6

Late *Type II* fluid inclusions

SAMPLE	AREA	Min.Host	GENERATION	Type FI	PHASE	T_m ist.°C	T_h °C
XML9	B1	Opx	Late	INTERGRANULAR	L		-8
"	"	"	"	"	"		-6
"	"	"	"	"	"		-5.3
"	"	"	"	"	"		-5.2
XML9	B2	Cpx	Late	INTRAGRANULAR	L		-8.2
"	"	"	"	"	"		-10.4
"	"	"	"	"	"		-12.7
"	"	"	"	"	"		-14.4
"	"	"	"	"	"		-10.4
"	"	"	"	"	"		-11.4
"	"	"	"	"	"	-56.8	-11.4
"	"	"	"	"	"		-11
"	"	"	"	"	"		-11
"	"	"	"	"	"		-11
"	"	"	"	"	V		22.5
"	"	"	"	"	L		-14.4
"	"	"	"	"	"		15.7
"	"	"	"	"	"		12.6
XML9	B3	Cpx	Late	INTRAGRANULAR	L		-6
"	"	"	"	"	"		-10.5
"	"	"	"	"	"		-9.5
"	"	"	"	"	"		-8.2
"	"	"	"	"	"		-6
"	"	"	"	"	"	-57.2	-9.5
"	"	"	"	"	"		-6.5
"	"	"	"	"	"		-6
"	"	"	"	"	"		-12
"	"	"	"	"	"		-10.6
"	"	"	"	"	"		2.7
"	"	"	"	"	"		2.7
"	"	"	"	"	"		2.5
"	"	"	"	"	"		-0.6
"	"	"	"	"	"		0.3
XML10	C	Opx	Late	INTRAGRANULAR	L		-26
"	"	"	"	"	"		-26.5
"	"	"	"	"	"	-56.6	-27
"	"	"	"	"	"		-24
"	"	"	"	"	"		-22
"	"	"	"	"	"		-24
"	"	"	"	"	"		-24
"	"	"	"	"	"		-25
"	"	"	"	"	"		-18.5
"	"	"	"	"	"		-18.5
"	"	"	"	"	"		-14
"	"	"	"	"	"		-20.3
"	"	"	"	"	"		-19.2
"	"	"	"	"	"		-16.5
"	"	"	"	"	"		-13.5
"	"	"	"	"	"		-33
"	"	"	"	"	"		-23.5
"	"	"	"	"	"		-26
"	"	"	"	"	"		-24.5
"	"	"	"	"	"		-24
"	"	"	"	"	"		-22.7
"	"	"	"	"	"		-22.6
"	"	"	"	"	"		-24.2
"	"	"	"	"	"		-23
"	"	"	"	"	"		-23.1
"	"	"	"	"	"		-23

Late *Type II* fluid inclusions

SAMPLE	AREA	Min.Host	GENERATION	Type FI	PHASE	T_m ist.°C	T_h °C
XML10	A	Cpx	Late	INTRAGRANULAR	L	-57.2	2.9
"	"	"	"	"	V		29.8
"	"	"	"	"	L		-17
"	"	"	"	"	"		-19.8
"	"	"	"	"	"	-56.6	-17.1
XML10	A	Cpx	Late	INTRAGRANULAR	V		27.8
"	"	"	"	"	L		-17
"	"	"	"	"	"		-23
"	"	"	"	"	"		-21
"	"	"	"	"	"		-21.5
XML10	B	Cpx	Late	INTRAGRANULAR	L		-37.5
"	"	"	"	"	"		-30.7
"	"	"	"	"	"		-32.1
"	"	"	"	"	"		-27.1
"	"	"	"	"	"		-16.5
"	"	"	"	"	"		-17.2
"	"	"	"	"	"		-16.5
"	"	"	"	"	"		-24.2
"	"	"	"	"	"		-18.2
"	"	"	"	"	"	-56.7	-11.8
"	"	"	"	"	"	-56.7	-24.5
"	"	"	"	"	"		-21.2
"	"	"	"	"	"		-16.1
"	"	"	"	"	"		-21.7
"	"	"	"	"	"		-24.5
"	"	"	"	"	"		-24.9
"	"	"	"	"	"		-16.2
"	"	"	"	"	"		-12.9
XML11	A	Cpx	Late	INTERGRANULAR	L		-30.5
"	"	"	"	"	"		-30.5
"	"	"	"	"	"		-31.9
"	"	"	"	"	"		-29.2
"	"	"	"	"	"	-56.7	11.4
"	"	"	"	"	"		17.1
"	"	"	"	"	"		7.1
"	"	"	"	"	"		11.2
"	"	"	"	"	"		11
XML11	B	Opx	Late	INTERGRANULAR	L	-56.7	-32.1
"	"	"	"	"	"		-32.2
"	"	"	"	"	"		-33
"	"	"	"	"	"		12.1
"	"	"	"	"	"		-32.1
"	"	"	"	"	"		-27.5
"	"	"	"	"	"		-24.6
"	"	"	"	"	"		9.4
"	"	"	"	"	"		8.7
"	"	"	"	"	"		-29.6
"	"	"	"	"	"		-26.1
"	"	"	"	"	"		-25
"	"	"	"	"	"		-27
"	"	"	"	"	"	-56.7	-27.3
"	"	"	"	"	"		-25.9
"	"	"	"	"	"		-26.2
"	"	"	"	"	"		7.5
"	"	"	"	"	"		6.2
XML11	B	Opx	Late	INTRAGRANULAR	L		-20.2
"	"	"	"	"	"		-29.3
"	"	"	"	"	"		-28
"	"	"	"	"	"		-29.5

Late *Type II* fluid inclusions

SAMPLE	AREA	Min.Host	GENERATION	Type FI	PHASE	T_m ist.°C	T_h °C
XML11	B	Opx	Late	INTRAGRANULAR	L	-56.6	-30.2
"	"	"	"	"	"		-30.1
"	"	"	"	"	"		-25.8
"	"	"	"	"	"		-20.2
"	"	"	"	"	"		-26
"	"	"	"	"	"		-12.5
XML11	C1	Opx	Late	INTRAGRANULAR	L	-56.6	-35.2
"	"	"	"	"	"		-35.1
"	"	"	"	"	"		-28.5
"	"	"	"	"	"		-28.5
"	"	"	"	"	"		-34.6
"	"	"	"	"	"		-28
"	"	"	"	"	"		-31.2
"	"	"	"	"	"		4.6
"	"	"	"	"	"		-25.6
"	"	"	"	"	"		-25.6
"	"	"	"	"	"		-25.4
"	"	"	"	"	"		11.6
"	"	"	"	"	"		14.1
"	"	"	"	"	"		-3.4
"	"	"	"	"	"		27.3
"	"	"	"	"	"		27
"	"	"	"	"	"		27.3
"	"	"	"	"	"		21.5
"	"	"	"	"	"		25
"	"	"	"	"	V		27.5
XML11	C2	Opx	Late	INTRAGRANULAR	L		27.1
"	"	"	"	"	"		21.8
"	"	"	"	"	"		-9.8
"	"	"	"	"	"		-16.2
"	"	"	"	"	"		11.8
"	"	"	"	"	"	-57.1	6
"	"	"	"	"	"		29.8
"	"	"	"	"	"		-30.8
"	"	"	"	"	"		-31.3
"	"	"	"	"	"		-30.7
"	"	"	"	"	"		-16.8
"	"	"	"	"	"		30.9
"	"	"	"	"	"		-29
"	"	"	"	"	"		-30.1
"	"	"	"	"	"		-24.4

The molar fractions of CO_2-N_2 in fluid inclusions calculated through Raman microspectroscopy analysis following Burke (2001).

Early *Type I* fluid inclusions

Data			Measurament conditions				Component	Band area			Composition
Sample	Site	Analyses	Laser	Power	Accumul (s)	N° accumul	Gas	Area lower band CO2	Area upper band CO2	Area N2	Mole fraction
XML8	F	A	532 nm	80 mw	60	3	CO_2	3821	7699		0.82
							N_2			2106	0.18
XML8	F	B	532 nm	80 mw	60	3	CO_2	1214	1966		0.91
							N_2			267	0.09
XML8	F	C	532 nm	80 mw	60	3	CO_2	2545	4819		0.93
							N_2			485	0.07
XML8	F	D	532 nm	80 mw	60	3	CO_2	102	176		0.95
							N_2			13	0.05
XML8	F	E	532 nm	80 mw	60	3	CO_2	268	493		0.93
							N_2			48	0.07
XML8	F	F	532 nm	80 mw	30	3	CO_2	257	461		0.95
							N_2			32	0.05
XML8	F	G	532 nm	80 mw	30	3	CO_2	82	151		0.94
							N_2			12	0.06